



Physical Characteristics of Chemically Propelled Colloids

A dissertation presented

by

Mei-Hsien Tu

to

The Department of Physics and Astronomy

in partial fulfillment of the requirements

for the degree of

Doctor of Philosophy

in the subject of

Physics

The University of Sheffield

March 2013

©2013 - Mei-Hsien Tu

All rights reserved.

A poet once said, The whole universe is in a glass of wine. We will probably never know in what sense he meant that, for poets do not write to be understood. But it is true that if we look at a glass of wine closely enough we see the entire universe.

There are the things of physics: the twisting liquid which evaporates depending on the wind and weather, the reflections in the glass, and our imagination adds the atoms. The glass is a distillation of the Earth's rocks, and in its composition we see the secrets of the universe's age, and the evolution of stars. What strange arrays of chemicals are in the wine? How did they come to be? There are the ferments, the enzymes, the substrates, and the products. There in wine is found the great generalization: all life is fermentation. Nobody can discover the chemistry of wine without discovering, as did Louis Pasteur, the cause of much disease. How vivid is the claret, pressing its existence into the consciousness that watches it!

If our small minds, for some convenience, divide this glass of wine, this universe, into parts - physics, biology, geology, astronomy, psychology, and so on - remember that Nature does not know it! So let us put it all back together, not forgetting ultimately what it is for. Let it give us one more final pleasure: drink it and forget it all!

Richard P. Feynman

Acknowledgments

First and foremost, I would like to express my sincere gratitude to my supervisor, Prof. Ramin Golestanian, who has continuously supported me throughout my PhD with his patience, motivation, encouragement, and knowledge, whilst allowing me to work in my own way. The enthusiasm he has for his research has been motivational for me, even during the tough time of the PhD pursuit. I appreciate all his contributions of time, ideas, and funding to make my PhD experience productive and stimulating. Without his guidance, my thesis would not have been completed.

In addition to my supervisor, I would like to thank Prof. Tanniemola B. Liverpool and Dr. Rhoda Hawkins, who are my viva examiners. I highly appreciate all their insightful comments, hard questions, and recommendations.

Furthermore, I gratefully acknowledge the financial support, including the fee scholarship and funding that I received from University of Sheffield. Many thanks to my friends and colleague, Dr. Arash Azari, Dr. Chia-Ying Chiang, Dr. Argyrios Karatrantos, Jack Morrice, Shu, and Emma, for their assistance and encouragement.

Last but not the least, I would like to thank my family for all their love and best wishes. Their faithful support during the final stages of this PhD has meant so much. Thank you.

MeiHsien Tu
University of Sheffield
March 2013

*Dedicatd to my **Family** and **Friends**;
to the people who never lost hope and honesty.*

Thesis supervisor

Author

Professor Ramin Golestanian

Mei-Hsien Tu

Physical Characteristics of Chemically Propelled Colloids

Abstract

Understanding the transport properties of microorganisms in fluid is a fundamental problem in soft matter physics, and the dynamics of an active colloid in non-equilibrium statistical mechanics has recently attracted pioneering investigations into the design of artificial swimming robots at the microscale. A topical review of the remarkable discoveries in the field, both theoretically and experimentally, is first addressed.

The mechanism of interfacial phoretic transport is used for an active colloid achieving autonomous propulsion by diffusiophoresis. A theoretical framework has been established to ascertain the generic properties of the active motion of such a self-propelled colloid, driven by the use of surface catalytic reactions. The kinetic route for the chemical reaction is considered as a two-step process, followed by quantitative procedures that examine the influence of fuel concentration and colloid size on the propulsion velocity. Specifically, both Janus and inhomogeneous colloids are studied, and their propulsion velocities rise linearly with the fuel concentration in a dilute solution and decay with the size scale in the small size limits. The theoretical results for a Janus sphere are consistent with the experimental observation.

Furthermore, to what extent can the incorporation of advection into the diffusion be interpreted as a means of self-propulsion. An advection-diffusion model is constructed to compute the concentration distribution of the solute and propulsion velocity, aiming to

explore the role played by the advection effects on the movement of Janus particles. The numerical results show that while Janus particle can achieve an autonomous propulsion at a small Péclet number, the accumulation of solute particles in the upstream of the colloid disappears at the large Pe limit.

In conclusion, the major outcome of this work is the demonstration of the qualitative agreement with the present analysis of mobility to explain the observed size dependence. Lastly, the results suggest that a catalytic colloid powered by diffusiophoresis is a useful model for self-propulsion and indicate what still needs to be done to obtain a full understanding of the swimming characteristics of colloidal dispersions.

Contents

Title Page	i
Acknowledgments	iv
Dedication	v
Abstract	vi
Table of Contents	viii
List of Figures	xi
List of Tables	xix
Citations to Previously Published Work	xx
1 Introduction and Overview	1
1.1 Introduction	1
1.2 Background	1
1.3 Artificial microswimmers	3
1.4 The hydrodynamics of microorganisms at low Reynolds numbers	4
1.5 Summary	9
2 Self-Propulsion at the Microscale	10
2.1 Introduction	10
2.2 Literature Review	10
2.2.1 Strategy for microscale propulsion	10

2.2.2	Diffusiophoresis	16
2.3	Summary	21
3	Reaction - Diffusion Model of Catalytic Colloids	27
3.1	Introduction	27
3.2	Model of Diffusion-Reaction at Low Reynolds Number	28
3.2.1	Slip Velocity for Diffusion-Reaction	28
3.2.2	Reaction-Diffusion Process of the Fuel Molecules	33
3.2.3	Scaling Region for Propulsion Velocity	41
3.3	Results	43
3.3.1	Janus Sphere	43
3.3.2	Inhomogeneous Sphere	54
3.4	Summary	61
4	Advection - Diffusion Model for Catalytic Janus Colloid	63
4.1	Introduction	63
4.2	Model of Advection-Diffusion for Phoretic Swimmers at Finite Péclet number	64
4.2.1	Advection-Diffusion Equation	64
4.2.2	Velocity Distribution	66
4.2.3	Flow Field	78
4.3	Results	82
4.3.1	Advection-Diffusion in Two Limits	84
4.3.2	Advection-Diffusion in General Condition	90
4.3.3	Flow Field for Janus and Inhomogeneous Spheres	100
4.4	Summary	104
5	Conclusion	107

Contents

5.1	Conclusion and discussion	107
5.2	Future landscape	110
	Bibliography	112
	A Stress Tensor	119

List of Figures

2.1	Schematics of the swimmer consisting of three linked spheres and its complete cycle of motion. Here D is the distance of the right and left spheres numbered 2 and 3 from the middle sphere, and ε is the relative displacement changed by the right or left arm [26] [27].	12
2.2	Schematic of a doublet of two differently sized paramagnetic polystyrene beads, attached by DNA linkers, rotating by an external oscillating magnetic field [32]. (a) Doublet rotating around an axis parallel to the plane is controlled by the external magnetic field H with frequency Ω . (b) and (c): The microscopic images illustrate that the doublet travels further along the x direction than the individual particle, and their trajectories are indicated by red and blue lines respectively.	22
2.3	Comparison of the experimental data (dots) and theoretical fittings (lines). Scaled doublet velocity V/V_0 is shown as a function of the strength H_0/H_1 and frequency Ω/Ω_B of the external oscillating magnetic field [32].	23

2.4 Schematic diagram illustrating a responsive gel body (red) with two propulsive flaps (green) attached to its opposite sides. The steering flap (green) at the front of the swimmer is sensitive to light (yellow), and velocity vectors through the middle of the gel body are shown by green cones. Combined with the steering flap bending, the periodic beating of the propulsion flaps could move the device forward [35]. 24

2.5 Sketch of a gold-platinum nanorod showing the mechanism for electrokinetic process of decomposition of hydrogen peroxide [51]. Due to the decomposition of H_2O_2 at metal surfaces, an electrical current is created from Pt to Au end. Therefore, the bimetallic rod can achieve propulsion and is seen to move in the direction of the platinum end. 24

2.6 An illustration of autonomous diffusiophoretic motion of a colloid with an enzymatic site (red). The Solute molecules of diameter a are dissolved in the fluid surrounding the colloid with radius R . Due to a reaction on a catalytic patch of the surface of the colloid, an asymmetric concentration gradient of solutes is created, leading to self-propulsion for the spherical swimmer [71]. 25

2.7 Measured displacement of both the control (blank) and platinum-coated particles suspended in different hydrogen peroxide concentrations [72]. Locomotion of $\times 5$ polystyrene beads in varying solution was recorded over 25 seconds, and the trajectory for each measurement in the same concentration is shown by different colours. 25

2.8 The mean squared displacements of platinum-coated particles [72]. Each colour represents different concentrations of hydrogen peroxide. The parabolic curve for high concentration of H_2O_2 indicates an enhanced diffusion. . . . 26

3.1	Decay of hypothetical potential $W(y)$ in the diffused layer (slipping plane) with thickness λ	29
3.2	The slip velocity \mathbf{v}_s is a function of normal distance from the colloidal surface y	31
3.3	Schematic of active colloid with radius R suspended in fluid molecules. The slipping velocity \mathbf{v}_s is induced by the flux of solute molecules at position \mathbf{r}_s within the interface, and the slipping plane is shown as the dashed circle with length scale λ . An inhomogeneous distribution of solutes drives the motion of colloid with the translation velocity V	33
3.4	The coverage function $K(\theta)$ for a Janus sphere.	36
3.5	The coverage function $K(\theta)$ for inhomogeneous case 1.	36
3.6	The coverage function $K(\theta)$ for inhomogeneous case 2	37
3.7	The coverage function $K(\theta)$ for inhomogeneous case 3	37
3.8	Three scaling regions for the propulsion velocity of a Janus sphere as a function of the size and fuel concentration. The crossover boundaries between these three regimes are presented by red dashed lines, and blue dotted lines indicate the locations which correspond to the previous experiments of Ref. [72] [73]. The red diagonal dot-dashed line means the crossover between regime II and III remains implicit.	42
3.9	Three scaling regions for the propulsion velocity of an inhomogeneous sphere as a function of the size and fuel concentration. Blue dashed and diagonal dot-dashed lines show the crossover boundaries between regimes I, II and III.	43
3.10	For a Janus sphere, the B_1 coefficient that determines the swimming velocity is a function of size parameter $\frac{k_1 R}{D_{hp}}$ at constant values of $\frac{k_1 C_\infty}{k_2}$. The colourful lines indicate different fuel concentrations $\frac{k_1 C_\infty}{k_2}$ ranging from 0.1 to 10.	44

3.11 The surface concentration of hydrogen peroxide $C_{\text{hp}}(R, \theta)$ is a function of the latitude angle θ . Coloured lines in the legend present different parameters for size and fuel concentration. 45

3.12 The surface probability for the unoccupied state p_{fr} is a function of the latitude angle θ , and this basically reflects the catalyst geometry of a Janus sphere. Various parameters of size and fuel concentration are shown by different coloured lines. 46

3.13 The concentration profile of hydrogen peroxide C_{hp} for a Janus sphere in 3D. 47

3.14 The concentration profile of the products (water and oxygen) for a Janus sphere in 3D. 47

3.15 The contour plot for the concentration of hydrogen peroxide. One hemisphere of the Janus colloid coated with the catalyst is shown by purple, and color bar indicates high (yellow) versus low (dark blue) concentration. Due to the decomposition of substrate in the chemical reaction, there is a depletion of particles in the vicinity of the coated area. 48

3.16 The contour plot for the product concentration, and discrete contour levels with high/low concentration are presented by colour bar. An accumulation of product molecules is created around the catalytic patch (purple) since more and more water and oxygen are generated from the reaction. 49

3.17 The velocity of the Janus sphere v.s. $\frac{k_1 C_\infty}{k_2}$ at constant values of $\frac{k_1 R}{D_{\text{hp}}}$ plotted on a logarithmic scale. Coloured lines indicate different size parameters $\frac{k_1 R}{D_{\text{hp}}}$ ranging from 0.01 to 10. As the propulsion velocity is proportional to the fuel concentration, the slope in this log-log plot is 1. 50

3.18 The velocity of the sphere v.s. $\frac{k_1 R}{D_{\text{hp}}}$ at constant values of $\frac{k_1 C_\infty}{k_2}$ are plotted on a logarithmic scale. Coloured lines show different fuel concentration $\frac{k_1 C_\infty}{k_2}$ ranging from 0.1 to 10. As the propulsion velocity decays with the swimmer size, the slope in the log-log plot is -1 51

3.19 A comparison of the theoretical and experimental results for the swimming velocity of a Janus sphere as a function of its radius [73]. The numerical results for the theory are shown by a solid line, while dots indicate the experimental data. Inset: the same results in log-log form. 53

3.20 B_1 v.s. $\frac{k_1 R}{D_{\text{hp}}}$ at constant values of $\frac{k_1 C_\infty}{k_2}$ for inhomogeneous case 1. 55

3.21 B_1 v.s. $\frac{k_1 R}{D_{\text{hp}}}$ at constant values of $\frac{k_1 C_\infty}{k_2}$ for inhomogeneous case 2 55

3.22 B_1 v.s. $\frac{k_1 R}{D_{\text{hp}}}$ at constant values of $\frac{k_1 C_\infty}{k_2}$ for inhomogeneous case 3 56

3.23 The propulsion velocity v.s. $\frac{k_1 C_\infty}{k_2}$ at constant values of $\frac{k_1 R}{D_{\text{hp}}}$ plotted in the logarithmic scale for inhomogeneous case 1; the slope for this log-log plot is 1. 57

3.24 The propulsion velocity v.s. $\frac{k_1 C_\infty}{k_2}$ at constant values of $\frac{k_1 R}{D_{\text{hp}}}$ plotted in the logarithmic scale for inhomogeneous case 2; the slope for this log-log plot is 1. 57

3.25 The propulsion velocity v.s. $\frac{k_1 C_\infty}{k_2}$ at constant values of $\frac{k_1 R}{D_{\text{hp}}}$ plotted in the logarithmic scale for inhomogeneous case 3; the slope for this log-log plot is 1. 58

3.26 The propulsion velocity v.s. $\frac{k_1 R}{D_{\text{hp}}}$ at constant values of $\frac{k_1 C_\infty}{k_2}$ plotted in the logarithmic scale for inhomogeneous case 1; the slope for this log-log plot is -2 58

3.27 The propulsion velocity v.s. $\frac{k_1 R}{D_{\text{hp}}}$ at constant values of $\frac{k_1 C_\infty}{k_2}$ plotted in the logarithmic scale for inhomogeneous case 2; the slope for this log-log plot is -2 59

3.28 The propulsion velocity v.s. $\frac{k_1 R}{D_{\text{hp}}}$ at constant values of $\frac{k_1 C_\infty}{k_2}$ plotted in the logarithmic scale for inhomogeneous case 3; the slope for this log-log plot is -2 59

4.1	For $N = 2$ and $t \rightarrow 1$, the C_0 of surface concentration as a function of Pe	84
4.2	For $N = 2$ and $t \rightarrow 1$, the C_1 of surface concentration as a function of Pe	84
4.3	For $N = 2$ and $t \rightarrow 1$, the C_2 of surface concentration as a function of Pe	85
4.4	For $N = 2$ and $t \rightarrow 1$, the surface concentration v.s. Pe for $\theta = 0$	86
4.5	For $N = 2$ and $t \rightarrow 1$, the surface concentration v.s. Pe for $\theta = \frac{\pi}{4}$	86
4.6	For $N = 2$ and $t \rightarrow 1$, the surface concentration v.s. Pe for $\theta = \frac{\pi}{2}$	86
4.7	For $N = 2$ and $t \rightarrow 1$, the surface concentration v.s. θ for Pe = 1	87
4.8	For $N = 2$ and $t \rightarrow 1$, the surface concentration v.s. θ for Pe = 10	87
4.9	For $N = 2$ and $t \rightarrow 1$, the surface concentration v.s. θ for Pe = 100	87
4.10	For $N = 2$ and $t \rightarrow 0$, the concentration at infinity v.s. Pe for $\theta = 0$	88
4.11	For $N = 2$ and $t \rightarrow 0$, the concentration at infinity v.s. Pe for $\theta = \frac{\pi}{4}$	88
4.12	For $N = 2$ and $t \rightarrow 0$, the concentration at infinity v.s. Pe for $\theta = \frac{\pi}{2}$	88
4.13	For $N = 2$ and $t \rightarrow 0$, the concentration at infinity v.s. θ for Pe = 1	88
4.14	For $N = 2$ and $t \rightarrow 0$, the concentration at infinity v.s. θ for Pe = 10	89
4.15	For $N = 2$ and $t \rightarrow 0$, the concentration at infinity v.s. θ for Pe = 100	89
4.16	For $N = 3$ and $t \rightarrow 1$, the C_0 of surface concentration as a function of Pe	90
4.17	For $N = 3$ and $t \rightarrow 1$, the C_1 of surface concentration as a function of Pe	90
4.18	For $N = 3$ and $t \rightarrow 1$, the C_2 of surface concentration as a function of Pe	90
4.19	For $N = 3$ and $t \rightarrow 1$, the C_3 of surface concentration as a function of Pe	90
4.20	For $N = 1$, C_0 as a function of t	91
4.21	For $N = 1$, C_1 as a function of t	91
4.22	For $N = 2$, C_0 as a function of t	92
4.23	For $N = 2$, C_1 as a function of t	92
4.24	For $N = 2$, C_2 as a function of t	92
4.25	For $N = 3$, C_0 as a function of t	92
4.26	For $N = 3$, C_1 as a function of t	92

4.27	For $N = 3$, C_2 as a function of t	93
4.28	For $N = 3$, C_3 as a function of t	93
4.29	For $N = 4$, C_0 as a function of t	93
4.30	For $N = 4$, C_1 as a function of t	93
4.31	For $N = 4$, C_2 as a function of t	93
4.32	For $N = 4$, C_3 as a function of t	93
4.33	For $N = 4$, C_4 as a function of t	94
4.34	For $N = 1$ and $Pe = 1$, the surface concentration v.s. θ	94
4.35	For $N = 2$ and $Pe = 1$, the surface concentration v.s. θ	94
4.36	For $N = 3$ and $Pe = 1$, the surface concentration v.s. θ	94
4.37	For $N = 4$ and $Pe = 1$, the surface concentration v.s. θ	94
4.38	For $N = 1$, C_1 v.s. Pe	95
4.39	For $N = 2$, C_1 v.s. Pe	95
4.40	For $N = 3$, C_1 v.s. Pe	95
4.41	For $N = 4$, C_1 v.s. Pe	95
4.42	For $N = 4$, $Pe = 1$, the concentration distribution of the solute for a Janus sphere in 3D.	96
4.43	For $N = 4$, $Pe = 1$, the contour plot for the concentration profile of the so- lute and an accumulation in the vicinity of the Janus sphere in its upstream region. The Janus colloid is placed in the centre, and color bar indicates high (yellow) versus low (dark blue) concentration.	97
4.44	For $N = 4$, $Pe = 100$, the concentration distribution of the solute for a Janus sphere in 3D.	98
4.45	For $N = 4$, $Pe = 100$, the contour plot for the concentration profile of the solute. There is no an accumulation of particles because of no symmetry breaking.	99

4.46 The flow field around the Janus sphere for $\frac{k_1 C_\infty}{k_2} = 0.5$ and $\frac{k_1 R}{D_{hp}} = 0.5$ in region I of the diagram in Figure 3.8. 101

4.47 The flow field around the Janus sphere for $\frac{k_1 C_\infty}{k_2} = 5$ and $\frac{k_1 R}{D_{hp}} = 0.5$ in region II of the diagram in Figure 3.8. 101

4.48 The flow field around the Janus sphere for $\frac{k_1 C_\infty}{k_2} = 0.5$ and $\frac{k_1 R}{D_{hp}} = 1$ in region III of the diagram in Figure 3.8. 102

4.49 The flow field around the Janus sphere for $\frac{k_1 C_\infty}{k_2} = 0.5$ and $\frac{k_1 R}{D_{hp}} = 5$ in region III of the diagram in Figure 3.8. 102

4.50 The flow field around the Janus sphere for $\frac{k_1 C_\infty}{k_2} = 0.5$ and $\frac{k_1 R}{D_{hp}} = 10$ in region III of the diagram in Figure 3.8. 103

4.51 The flow field around the Janus sphere for $\frac{k_1 C_\infty}{k_2} = 0.5$ and $\frac{k_1 R}{D_{hp}} = 20$ in region III of the diagram in Figure 3.8. 103

4.52 The flow field around the Janus sphere for $\frac{k_1 C_\infty}{k_2} = 0.5$ and $\frac{k_1 R}{D_{hp}} = 50$ in region III of the diagram in Figure 3.8. 104

4.53 The flow field around the inhomogeneous sphere for $\frac{k_1 C_\infty}{k_2} = 0.5$ and $\frac{k_1 R}{D_{hp}} = 0.5$ in region I of the diagram in Figure 3.9. 105

4.54 The flow field around the inhomogeneous sphere for $\frac{k_1 C_\infty}{k_2} = 5$ and $\frac{k_1 R}{D_{hp}} = 0.5$ in region II of the diagram in Figure 3.9. 105

4.55 The flow field around the inhomogeneous sphere for $\frac{k_1 C_\infty}{k_2} = 0.5$ and $\frac{k_1 R}{D_{hp}} = 50$ in region III of the diagram in Figure 3.9. 106

List of Tables

1.1 Reynolds numbers for different species	5
------------------------------------------------------	---

Citations to Previously Published Work

Major portions of Chapter 3 have appeared in the following papers:

“Size dependence of the propulsion velocity for catalytic Janus-sphere swimmers“, S. Ebbens, M.-H. Tu, J.R. Howse, and R. Golestanian, *Phys. Rev. E* **85**, 020401(R) (2012).

Electronic preprints (shown in `typewriter font`) are available on the Internet at the following URL:

`http://arXiv.org`

Chapter 1

Introduction and Overview

1.1 Introduction

In this chapter, general information about swimming at the microscale and subdivisions of the topic are provided. A statement of the problem will then be discussed in order to specifically address the research question.

1.2 Background

The world is filled and inhabited with abundant microorganisms, many of which first appeared on Earth nearly four billion years ago [1] [2] [3]. Despite their tiny size, these microorganisms are essential for the survival of all organisms and have a significant effect on many biological processes, including reproduction, infection, and the marine life ecosystem. Bacteria, fungi, and algae convert energy and release nutrients into the environment when breaking down the waste from humans, animals and plants, which enables other organisms to gain energy from the process of decomposition. Microorganisms are also involved in the cycle of many important elements and compounds, including oxygen, carbon and nitrogen, and the endless cycle of materials is also linked to the transformation

of energy in nature. For example, massive plankton blooms form one part of the oceanic ecosystem and bacterial metabolites in the ocean decompose not only carbon, but also nitrogen, phosphorus and sulphur. Furthermore, microbes take part in the production of food, such as the conversion of sugar into other compounds when using yeast or bacteria in the absence of oxygen, namely fermentation. The process of fermentation is often used, with the help of microbes, to produce tasty food, such as beer, yogurt, cheese, wine, bread, and chocolate, to name but a few. Thus, microbes are essential to agriculture and the global circulation of materials.

Generally, at least one thousand different species of microbiomes inhabit the human body and the total number of microbiomes is estimated to be 10 – 100 trillion [4] [5]. In other words, there are ten times the number of microbial cells as there are human cells [4] [5] [6] [7], and this makes an individual human a giant superorganism. The metabolic activity performed by these microbes has various tasks at different locations in the human body and plays a vital role in the digestion and absorption of food as well as in protecting against infections at the cellular level. However, many bacteria, fungi and viruses are harmful to humans and result in many diseases and severe illnesses, such as smallpox, food poisoning, and the plague during the Middle Ages. While some microbes cause disease, others are beneficial to human health, working with our bodies in many complex and subtle ways. For instance, motile cilia are present in the lining of the human lungs and the windpipe (trachea), sweeping mucus and dirt out of the airways in order to provide protection against infections [8]. Other types of cilia in the cochlear and some brain tissues are responsible for the detection of vibrations caused by sound and the circulation of cerebrospinal fluid [9]. The millions of microbes that reside on our skin and inside us, form a protective barrier to prevent pathogens from colonising the skin's surface, boosting the skin's immune system [10]. Without the skin microbiomes, our bodies would be open

to microbial attacks. As microbes are essential to the Earth and to humans, considerable research has been carried out into how the microbes that call the human body home affect our health, their locomotion and collective motion; there are still many areas to be investigated.

Transport is a fundamental requirement for all living matter, not only when searching for food or finding a mate, but also for escaping from danger. Physiological processes must continually take place in order to transport the required materials to and from all areas of the human body, right down to the individual cells. At the cellular level, nutrients are transported to cells, and waste materials are then moved out of these cells through the process of osmosis and diffusion. Osmosis across the cell membrane, which is semipermeable, separates and expels bio-waste and keeps the bloodstream free from impurities in our bodies. The system that transports food, water, and nutrients between the cell, the organism, and the external environment helps us to maintain health and sustain life. To survive in such a wide variety of habitats, microbes have evolved a great number of mechanisms to obtain energy, digest food and reproduce, and the locomotion of active organisms, such as bacteria and cell motility, share certain characteristics in common. It is important that the mechanisms of the microorganisms determine their movement, and an understanding of their locomotion is crucial when designing synthetic nanomotors.

1.3 Artificial microswimmers

The issue of artificial micro- or nanoswimmers in fluid has been widely investigated in order to explore the physical and biophysical principles underlying the locomotion. The field of micro- or nanoswimmers, which can convert physical or chemical energy sources

into mechanical work, emerged at the end of the 1990s due to the demand for tiny devices to aid chemical, biochemical and medical applications, such as monitoring, drug delivery and cell repair. This opens an avenue to produce autonomous devices: micro- and nanorobots, controlled by different mechanisms. The research into designing artificial swimming robots that include several feasible features or functions has been useful as it has yielded new information that is applicable to humans. Swimming robots could be delivered to specific cellular targets when they are injected into the body via the vascular and digestive systems with the aim of performing medical tasks. A nanoswimmer could incorporate a possible number of attachments in order to sense, transport, and be tailored to swim through the bloodstream with speed and efficiency [11]. Such a micro- or nanoscale delivery vehicle could attach probes, which could then monitor the location of the device. Consequently, it is hoped that these robots can help the avoidance of major invasive surgery and enhance the diagnosis of disease.

1.4 The hydrodynamics of microorganisms at low Reynolds numbers

Despite the fact that artificial nanoswimmers have plenty of potential applications, it is difficult to keep a small robot going in a steady direction and also navigate it to its desired destination. This is due to the combination of a low Reynolds number and Brownian motion in the nanoworld. Physically, as the size of an object decreases, the mass and weight decrease as the third power of its size. As an object gets smaller and smaller, forces, such as molecular attraction and cohesion, become more significant, and the gravitation exerted on the object decreases due to the reduction in mass. Thus, the key difference between the nanoworld and our everyday life is that viscous dissipation completely dominates inertial effects, and this refers to the low Reynolds number environment. The Reynolds number

Re is a dimensionless number that gives a measure of the ratio of inertial forces to viscous force [12]:

$$\text{Re} = \frac{\rho V a}{\eta}, \quad (1.1)$$

where a is the dimension of the body, V represents its speed, ρ is the density of the fluid, and η denotes the fluid viscosity, a measure of a fluid's tendency to stick together. Table 1.1 shows examples of the Reynolds number range from very large values to extremely small ones [13]. For instance, the Reynolds number of a swimming whale is approximately of the order $\mathcal{O}(10^8)$, whereas for a swimming bacteria it is roughly $\mathcal{O}(10^{-5})$ to $\mathcal{O}(10^{-4})$ [14].

Table 1.1: Reynolds numbers for different species [13]

	Reynolds number
A large whale swimming at 10 m/s	300,000,000
A tuna swimming at the same speed	30,000,000
A duck flying at 20 m/s	300,000
A large dragon fly going 7 m/s	30,000
A copepod in a speed burst of 0.2 m/s	300
Flapping wings of the smallest flying insects	30
An invertebrate larva, 0.3 mm long, at 1 mm/s	0.3
A sea urchin sperm advancing the species at 0.2 mm/s	0.03
A bacterium, swimming at 0.01 mm/s	0.00001

In the nanoworld, water itself acts as a very viscous liquid because the inertia of a swimmer is completely irrelevant to its motion at a low Reynolds number. As the inertial forces are assumed to be negligible, the Navier-Stokes equation, the governing equation of

fluid motion, can be reduced to the Stokes equation:

$$-\nabla p + \eta \nabla^2 \mathbf{v} + \mathbf{f} = 0, \quad (1.2)$$

where p is pressure, η presents the fluid viscosity, \mathbf{v} is the flow velocity, and \mathbf{f} denotes external force. Since the Stokes equation is linear and exhibits time reversal symmetry, a periodic and reciprocal motion cannot lead to any locomotion in an inertia-less realm. Therefore, swimming in a viscous fluid is a big challenge for small objects. Due to the property of time reversibility, it is difficult to mix together two or more viscous fluids, and this amazing phenomenon is called laminar flow [8] [15] [16]. For example, drops of dye are injected into a cylinder filled with syrup, following which the inner cylinder is rotated slowly so that the drops appear uniformly around the entire container. Surprisingly, these dyed drops can return to their initial state or starting point by simply reversing the direction of the mixing.

In addition, rules of physics are governed by different length scales, and thermal fluctuations become important at the microscale [17]. When a micro-sized object is suspended in gas or liquid, its movement is considerably influenced by the continuous collision of randomly moving particles in the environment, and this effect is a type of thermal perturbation. The direction of the micro-sized particle is constantly changing whilst other gas or liquid molecules are striking it. This deflection is due to the transfer of kinetic energy from the rapidly moving molecule to the tiny particle, a phenomenon known as Brownian diffusion. The stochastic process involves a random force field due to the significant effect of thermal noise or other fluctuations of the solvent on the particle. Therefore, one needs propulsion strategies that can maintain the orientation of a microrobot efficiently in viscous environments and which can overcome the thermal fluctuations from the surroundings. In the following section, the aim is to introduce various methods that microorganisms have

adopted to achieve propulsion in fluid.

Movement is one of the existential requirements of creatures and a microorganism is no exception. In nature, microorganisms have evolved various sophisticated mechanisms in order to search for food, mates, or avoid danger, and the solutions are diverse. The following are some examples of how propulsion can be achieved by a sequence of shape deformations under time-reversal invariants. Many microswimmers use one or more appendages to generate mobility in a viscous environment [18]. The appendant part could be a relatively stiff helix that is rotated by a motor embedded in the cell wall [18], or it could be a flexible filament undergoing whip-like motions due to the action of molecular motors [11]. Bacteria, such as *Escherichia coli*, can swim and tumble by applying chemical energy to operate a flagellum, which is powered by a rotary motor and acts as a rigid propeller. This ability is important for *E. coli*, enabling it to obtain food by detecting fluid flow, gradients in nutrients and to move to regions of higher concentration [19].

Furthermore, both cilia and flagella have unique propulsion mechanisms that perform different functions at various locations within the human body. Flagella propel themselves with hair-like structures which can exhibit a variety of structures and movement patterns [20] [21]. Moreover, cilia are also used for nutrient uptake and quorum sensing by detecting other physical and chemical signals. The movement of an individual cilium is asymmetric with an effective stroke and a recovery stroke [22]. Many cilia are arranged in rows on the cell surface and can beat synchronously while being slightly out of phase with the adjacent row. *Paramecium*, covered with thousands of cilia, can move forwards and backwards based on the locomotion of coordinated waves of beating performed by the cilia [23].

When designing artificial microrobots, there are two main approaches to accumulate

this development. One is to be inspired by motile cells and bacterium and to mimic their propulsion mechanisms. The other is to establish theoretical models or clever experiments that shed a new light on the hidden world of motility at the micro- or nanoscale. The task in the next chapter is to make current developments more precise.

The rest of the thesis is organised as follows. In Chapter 2, this study embarks on an ambitious journey to illustrate how the evolution of designing artificial microbes, and a review of the current state of research in the field, is intimately related to swimming at a low Reynolds number. In despite of the diverse mechanisms of propulsion, all have some basic underlying principles, which will be highlighted in the following section.

Chapter 3 explores a facet of the locomotion of active colloids that asymmetrically catalyses a chemical reaction and can achieve autonomous propulsion due to diffusiophoresis. Firstly, a diffusion-reaction model for the concentration of solutes is applied, and the catalytic activity occurring on the surface of the colloid is considered as a two-step process. The computed concentration profile is employed to calculate the velocity distribution of the asymmetrically catalysed colloid, and the results show that the propulsion velocity decays with the size of this particle. The effects of various sized colloid scales and solute concentrations have been examined, and the qualitative picture of the size dependence of the velocity distribution is in good agreement with the theoretical predictions and experimental data. The computational investigations of the active colloids give an insight into the nature of the non-equilibrium phenomenon.

While self-diffusiophoresis is addressed under the diffusion-reaction model in Chapter 3, the effects of advection-diffusion on the solute dispersion is discussed in Chapter 4. This chapter begins by introducing some general information about advective effects, and

a natural question then arises: what role does advection-diffusion play? To address this question, the study examines a simple case, Janus sphere, and investigates the role played by advection-diffusion in a phoretic colloid. In addition, fluid field for diffusion-reaction model can be depicted by applying the theoretical framework of advection-diffusion.

Finally, Chapter 5 offers some general conclusions and directions for future research.

1.5 Summary

The issue of artificial micro- or nanoswimmers in fluid has been widely investigated, and these tiny devices could sense and transport attachments in order to perform various functions in nature and the human body. Despite these potential applications, it is difficult to keep a tiny robot going in a steady direction and to steer it to its destination because of the combination of Brownian motion and the viscous environment. Many bacteria have achieved autonomous propulsion powered by various mechanisms at low Reynolds numbers, and their movement provides rich information for designing artificial microswimmers.

Chapter 2

Self-Propulsion at the Microscale

2.1 Introduction

The goal of this review is to describe the theoretical framework and experimental techniques for locomotion at a low Reynolds number environment, such as water or the bloodstream. After a brief, general review of recent developments, the fundamental properties of locomotion without inertia are outlined, followed by a discussion of some of the remarkable contributions from artificial swimming robots, both theoretically and experimentally. This chapter aims to capture the excitement of this research area, which lies in a multidisciplinary area, including physics, chemistry, bioengineering, and applied mathematics.

2.2 Literature Review

2.2.1 Strategy for microscale propulsion

Self-propelled motion is one of the most fascinating aspects of biological systems and has an essential use in the human body at the cellular level. A typical example of intracellular self-propelled motion is a motor protein, which can convert chemical reactions

into mechanical work along filaments. Kinesin and myosin can utilise the chemical energy released by the hydrolysis of ATP, and the conformational changes from this hydrolysis leads to directed transport on microtubules or actins [24]. This motility process is vital as it affects many biological processes, including the cell division, muscle contraction, and axonal transport.

Recent developments in micro- and nanoscale engineering have led to the realisation of various miniature mobile robots. The synthetic nano- or microswimmers have attracted considerable theoretical and experimental interests, and a number of mechanisms have been proposed in order to produce a net displacement of the synthetic microrobot in an aqueous media. After a brief overview of previous studies, the focus is on self-propelled nano- and microsystems powered by diffusiophoresis.

In order to produce a net displacement in any direction in a viscous fluid, a non-reciprocal motion is required in order to break the time-reversal symmetry of the motion, an idea first stated by Purcell [25]. A typical reciprocal movement is the scallop theorem, in which a scallop opens slowly and shuts its shell quickly, but achieves no net progress by symmetrically flapping its arms. The pioneering work done by Purcell also concluded that a microswimmer requires at least two degrees of freedom when undergoing a non-reciprocal motion, and this imposes a constraint on the design of an artificial microbe.

A simple, one-dimensional swimmer consisting of three spheres linked in a row connected by two rigid rods was proposed by Najafi and Golestanian [26] [27]. The complete cycle of the non-reciprocal motion is divided into four stages, and the distinct mechanochemical states of the three linked spheres is illustrated in Figure 2.1. As the rods sequentially contract and expand in length, the four-stage cycle can lead to a net

translation of the whole system to the right side by an amount Δ . Therefore, the cycle of motion effectively causes the spheres to propel the device forward. In addition, the conformational cycle of such swimmers has two degrees of freedom, and it is assumed that the swimming velocity depends on the transition rates between elongated and shortened states [28]. Based on this simple kinetic model, the effect of an external force or load on the swimming velocity is discussed, and the results show that the position of the external force exerted can affect the performances of this swimmer when carrying a load or in resisting an opposing force [28].

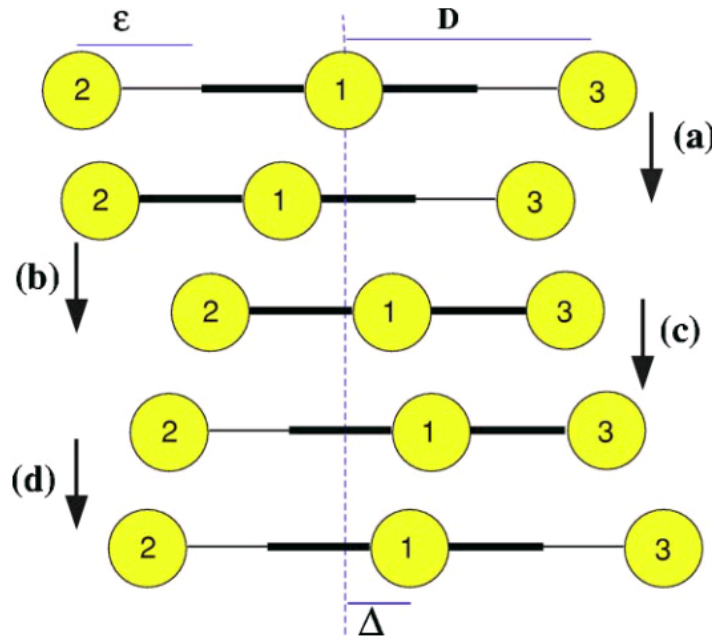


Figure 2.1: Schematics of the swimmer consisting of three linked spheres and its complete cycle of motion. Here D is the distance of the right and left spheres numbered 2 and 3 from the middle sphere, and ϵ is the relative displacement changed by the right or left arm [26] [27].

It is demonstrated that a chain of colloidal magnetic particles linked by DNA can be driven by an external oscillatory magnetic field [29], and this breakthrough in artificial

nanomotors is inspired by the motion of spermatozoa. As the alignment of the filament with an assembled blood cell was actuated by an oscillating magnetic field, the flexible linkage of magnetic particles attached to a red blood cell can behave like a propelled flagellum. Due to the combination of a static magnetic field and a sinusoidal field, a beating pattern was induced by the continuous deformation of the filament. The attached red-blood cell with a tail exhibits self-propulsion, and its swimming velocity and orientation depend on the external fields.

A new approach, developed by Mei and his colleagues in 2008, describes the recent progress on rolling up functional nanomembranes on polymers [30]. This rolled-up nanotech produces a catalytic tubular microjet by controlling the fabrication of metal and oxide tubes as well as many other material combinations including titanium/iron/gold/silver multilayer nanomembranes. Due to the decomposition of hydrogen peroxide following a catalytic reaction of the hydrogen peroxide with the silver inner tube wall, the propulsion of the microjets is generated by oxygen bubbles thrust out of an opening in the tube. This catalytic tubular microrobot has advanced performances, such as cargo delivery, dynamic assembly, and remotely controlled microjets.

It is reported that the motion of multi-oscillating dumb-bells with mutual phase differences can break the otherwise time reversible motion and cause directed motion [31]. Another swimming mechanism based on dumb-bells is experimentally demonstrated and theoretically analysed by Tierno et al. [32] [33] [34]. By switching an external magnetic field, a non-reciprocal rotation of DNA-linked doublets is produced in a viscous-dominated confined fluid, and the conformation of the system is illustrated in Figure 2.2. The path and orientation of the paramagnetic doublets can be controlled by an external oscillating magnetic field, and the velocity depends on the strength and frequency of the magnetic

field as shown in Figure 2.3.

Recently, a team of researchers at the Georgia Institute of Technology has developed a new model for microswimmer "flexible gel robots" powered by periodic expansions and contractions [35]. This system consists of a hydrogel which is ten microns long with two propulsive flaps attached to each side of the gel body, and its swimming direction is controlled by a flexible steering flap at its front, as shown in Figure 2.4. The responsive gel body undergoes periodic expansion and contraction in response to an external stimuli, such as light, temperature change or magnetic field, leading to volume changes in a cyclical way as well as a time-irreversible beating motion of the propulsion flaps. As a result, a net motion can be generated by the combination of movements of the gel body and the beating motion. The stimuli-sensitive body acts as an engine so that it can propel and navigate itself at low Reynolds numbers. Furthermore, the researchers have tested various parameters of gel and flap properties, such as size, oscillation rates, and intensity of external stimulus in order to optimize the efficiency of the propulsion.

According to a recent article [36], it is reported that a self-propelled microsystems without any external fuels can achieve an autonomous motion in a very acidic environment, such as the stomach and human blood serum. The interior material of the tubular polyaniline (PANI)/Zn microrocket is made of zinc, which is not only related to the generation of the hydrogen bubbles but is also more biocompatible. The mechanism is based on the bubbles of hydrogen gas spontaneously produced from the microrocket's nozzle. By testing different acidic conditions, the new microrockets display a speed-pH dependence, and this speed can reach 0.001 m/s .

Another method is discussed to achieve orientation by spinning under gravity [37].

This system which consists of three spheres connected by two arms can spin along their axes without external torque. The rotation can influence sedimentation gradually and this model can be extended to study the effect of gravity on a viscous fluid.

Cell motility in viscous fluids is ubiquitous and affects many biological processes, including reproduction, infection and the marine life ecosystem, and the polymerisation of actin proteins into dynamic filament structures plays a crucial role in cell motility. Actin is a protein involved in many cellular processes ranging from the regulation of gene transcription to acting as a motor in cell motility [38] [39]. Actin polymerisation is responsible for the motile properties of cells, such as Eukaryotic cell migration, as it can generate the force which deforms the cell membrane. In a typical example, the movement of *Listeria monocytogenes* can be induced by polymerising or depolymerising actin filaments and the observation reveals that the nucleation and elongation of actin filaments are stimulated by the ActA and Arp2/3 complex. The assembly of comet tails made of actin filaments is developed and is essential for coupling actin polymerisation to the force that drives bacterial propulsion [40] [41]. Furthermore, there is a condition where the effect of the non-diffusing solute is considered. In this scheme, the actin comet tail of *Listeria* could be modelled as an inert trailing particle and perform as a porous medium, inducing motility in the advection dominated regime [42].

In order to understand actin dynamics in cells, a mathematical model based on a combination of passive polymerisation and branched-network growth is reviewed [43]. To maintain a consistent supply of actin monomers, actin filaments are eventually severed and depolymerised. Filament density is regulated by capping protein binding to the filament tips, ceasing polymerisation [43].

An important point to notice is that most nanomotor mechanisms, mentioned above, involve either metals or solutions which are not biocompatible with the human body. As a result, the application of such swimming robots is restricted. Enzymes, being a group of natural bio-chemical substances that are responsible for enormous chemical reactions within the body, can overcome this drawback by operating in suitable substrates that are already present in the body. The non-reciprocal conformation changes of the enzyme, as well as diffusiophoresis and electrophoresis can conceivably be used to generate motion in the case of enzyme-driven nanomotors. The following section discusses enzyme-based microswimmers in detail and such micro- or nanomotors provide strategies for the design of synthetic ones.

2.2.2 Diffusiophoresis

The movement of colloidal particles caused by interactions between interfaces and external fields is referred to as phoretic transport [44], and this effect could be induced by a gradient in electrostatic potential (electrophoresis), solute concentration (diffusiophoresis), or temperature (thermophoresis). The various phoretic motions (electrophoresis, diffusiophoresis, thermophoresis) differ from sedimentation in that the driving forces operate within a thin interfacial layer at the surface of a particle rather than on the bulk of the particle. Many investigations on phoretic effect are focused on Janus sphere, which is composed of two different surface properties and named after the two-faced Roman god, and some of the subsequent works are outlined as follows.

Electrophoresis is the motion of a charged particle relative to a fluid under the influence of an electric field [45] [46] [47]. This occurs as the particle carries an electric surface charge which is acted upon by an electrostatic coulombic force from an external electric field [45] [46]. It is suggested that microswimmers are capable of moving autonomously

by self-electrophoresis in the presence of an externally applied electric field [44] [48] [49].

According to previous findings [50] [51] [52], nanorod devices consisting of gold-platinum rods with equal sized segments can move autonomously in a hydrogen peroxide solution. The system of rod-shaped nanoparticles with reaction-driven motion is directed to the right, as shown in Figure 2.5 [51]. The platinum acts as a catalyst for the decomposition of the hydrogen peroxide and remains unchanged throughout the chemical reaction. Due to the oxygen concentration gradient generated between the ends of the rod, the propulsion of such a conducting device exhibits enhanced translations along the rod axis at speeds of up to ten body lengths per second in the H_2O_2 solution. A further visual verification of the predicted direction of the fluid flow field in a coupled gold-platinum electrode system was obtained by monitoring tracer particles moving near to a gold-platinum catalytic micro pump [50] [51].

Several teams have studied fabricated self-propulsion powered by electrochemical reactions and the particles effectively act as short-circuited electrochemical cells. It is demonstrated that a carbon fibre is capable of moving autonomously by the redox reactions of glucose and oxygen occurring on its opposite sides [53]. Propulsion due to the electrochemical decomposition of hydrogen peroxide fuel into oxygen and water, has also been demonstrated to generate fluid flows above concentric electrodes [54] and in between interdigitated microelectrodes [51], as well as propelling rotating micro-gears made from platinum and gold [55] and bimetallic nanorod motors [56].

For thermophoresis or the Soret effect [57] – [65], it should be emphasised that the hot Brownian motion induced by low to moderate laser power is capable of self-propulsion, and movement could be as fast as self-diffusiophoretic colloids [66]. Using Janus particles

with their half hemisphere covered with gold, self-propelled motion was examined under externally imposed laser irradiation [67]. When the half-metal coated beads absorbed light from the non-uniform laser beam, it underwent substantially enhanced Brownian diffusion with a ballistic velocity enhanced mean-square displacements [67] [68].

Moreover, it is suggested that self-propulsion can be caused by an imbalance of concentration gradient on a Janus sphere, a colloidal particle made of two halves with different physical properties. The difference in the concentration of the molecules on the two sides of a Janus particle leads to an imbalance in the total kinetic energies of the molecules. Therefore, the particle tends to move towards the area of lower concentration, and this type of particle movement is known as diffusiophoresis [69]. Based on this effect, the locomotion of a colloid with an asymmetric coating of catalyst on its surface can achieve autonomous propulsion by diffusiophoresis [70] [71].

The simple model of a self-propelling device driven by diffusiophoretic effect was proposed by Golestanian et al.[71] and a sketch of the configuration is provided in Figure 2.6. In the scheme, the enzyme acts as a catalyst promoting the reaction rate of the chemical reaction in its vicinity. One benefit of propulsion by diffusiophoresis is high efficiency, as no additional power is needed. In fact, an enzyme simply increases the rate of reaction and remains unchanged throughout the chemical reaction. This means the sphere never loses its own fuel, and the process of the diffusiophoretic effect can only be slowed by changes within its surroundings.

Experiments on the diffusiophoretic effect has realised that the velocity of polystyrene Janus particles depends on the concentration of fuel molecules in a short time [72]. In this experiment, a spherical swimmer was a polystyrene ball with a diameter of $1.62 \mu m$, and

an asymmetric distribution of catalyst was coated on its surface. One half of the sphere was coated with platinum, whereas the other half remained bare. The swimmer was then placed in a solution of hydrogen peroxide (H_2O_2). During the chemical reaction, there were more product molecules generated in the vicinity of the coated hemisphere, and the gradient of solute concentration on the two sides of the Janus colloid becomes imbalanced. Consequently, the polystyrene ball was propelled by the asymmetric release of the reaction products. In order to demonstrate that the motion of the artificial micro swimmers was a function of the hydrogen peroxide concentration, a number of swimmers were produced and their trajectories were recorded over 25 seconds in various concentrations of hydrogen peroxide. Additionally, polystyrene spheres of the same size without a catalyst coat on their surfaces were also produced and used as control spheres. Both the coated and bare spheres were placed in the same solution, and their trajectories were tracked and compared in Figure 2.7 [72]. No matter how large the H_2O_2 concentration is, control particles still undergo Brownian motion. On the contrary, there is an enhanced diffusion of Pt-coated bead, and the displacement increases with the fuel concentration. Furthermore, the mean squared displacement can be estimated as a function of time by trajectory analysis. The mean squared displacements for the Pt-coated Janus spheres, immersed in hydrogen peroxide at various concentrations, are illustrated in Figure 2.8 [72]. While the curves for the 0% are linear with the elapsed time, they become parabolic by increasing the concentration of hydrogen peroxide up to 10%. The results in Figures 2.7 – 2.8 indicate that such a colloid has an effective autonomous propulsion, and how fast it can swim depends on the concentration of fuel molecules. The experimental observation can be explained by a generic model of diffusiophoresis proposed by Golestanian and his colleagues [71] [73].

There have been several investigations into diffusiophoresis and these have, so far,

yielded positive results. For certain motile biological systems, such as *Listeria monocytogenes*, a protein concentration gradient can be generated by polymerising or depolymerising protein filaments, and this provides a means of self-propulsion [74]. This mechanism is appropriate to an advective regime where the motion is dominated by the fluid advection instead of diffusion [75]. By local demixing of a critical binary liquid mixture, active motion can be easily tuned by illumination. Illumination techniques have been employed to confine, control and steer the motion of Janus colloids covered in gold on one of the hemispheres [76]. Furthermore, it has been demonstrated experimentally that the segregation and pattern formation of colloids and macromolecules can be achieved based on diffusionphoresis [77] [78].

A characteristic feature of such self-propelled motion is that self-motile colloids undergo stochastic motion depending on three distinct time scales: the vorticity diffusion time τ_h , the solute diffusion time τ_d , and the colloidal rotational diffusion time τ_r [79]. Experimental study has once again used the platinum catalysed reaction of decomposition of hydrogen peroxide and examined the effect of the observation time interval on the translation diffusion of Pt-coated Janus sphere in H_2O_2 solution [80]. In addition, making more complicated geometries, such as dumbbells with a variety of catalytic patterns has been suggested by S. Ebbens et al. [81]. A class of artificial microswimmers with combined translational and rotational self-propulsion has been studied experimentally. The chemically-fueled microswimmers are made of doublets of Janus colloidal beads with catalytic patches that are positioned at a fixed angle relative to one another. The mean-square displacement and the mean-square angular displacement of the active doublets were analysed from the context of a simple Langevin description, using the physical characteristics of the microswimmers, such as the spontaneous translational and rotational velocities extracted.

The physical characteristics of an active colloid powered by diffusiophoresis have been investigated theoretically, however, the previous model indicated the swimming velocity of a colloid with an asymmetric catalyst is independent of the size [82]. Furthermore, current research shows the effect of size on the propulsion velocity of the Janus sphere, both theoretically and experimentally, and the velocity decays as a function of size with inverse size-dependence [73]. The velocity has been studied systematically as a function of the fuel concentration and its size. The purpose of this thesis is to understand such properties from the molecular point of view.

In Chapter 3, a simple model of reaction-diffusion is considered, which is induced by using surface catalytic reactions and gradients of concentration to produce slip velocity that could lead to the net propulsion of a spherical swimmer.

2.3 Summary

So far, this topical review has reported a number of different systems, employing the various mechanism on miniature mobile robots at low Reynolds numbers. Although not all subjects are addressed, it is hoped that the collection of articles will stimulate further discussion of the highly non-intuitional world of motility at the microscale.

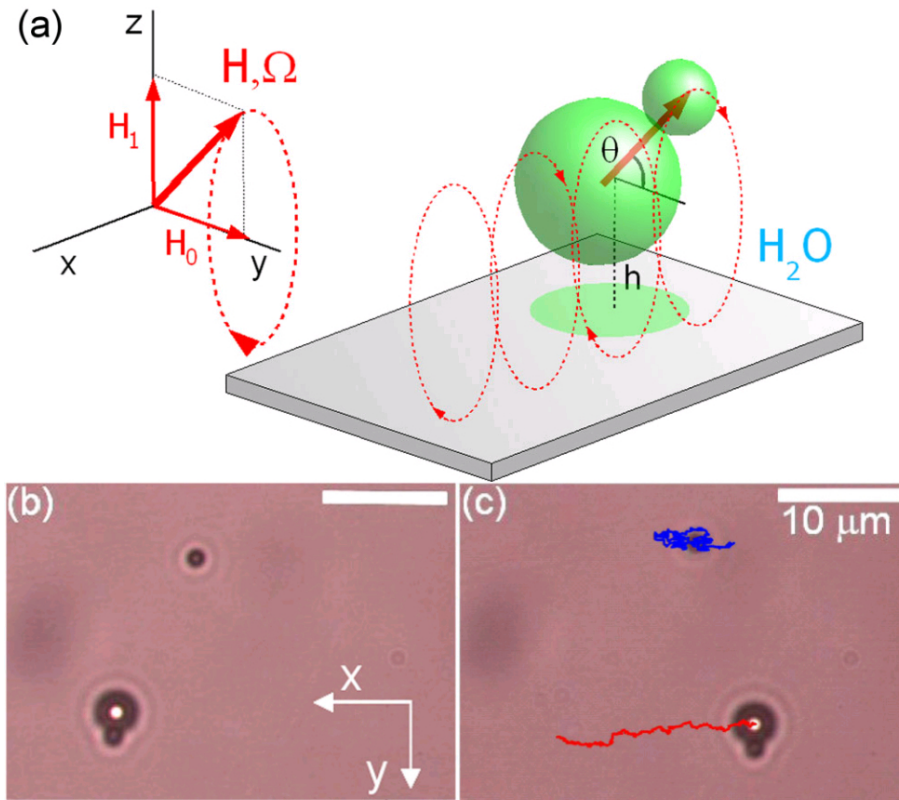


Figure 2.2: Schematic of a doublet of two differently sized paramagnetic polystyrene beads, attached by DNA linkers, rotating by an external oscillating magnetic field [32]. (a) Doublet rotating around an axis parallel to the plane is controlled by the external magnetic field H with frequency Ω . (b) and (c): The microscopic images illustrate that the doublet travels further along the x direction than the individual particle, and their trajectories are indicated by red and blue lines respectively.

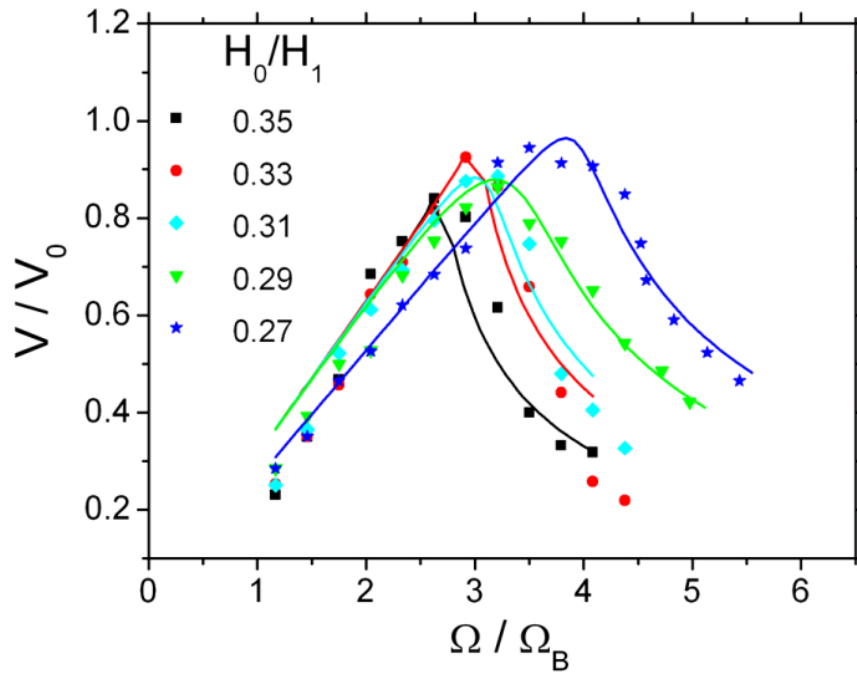


Figure 2.3: Comparison of the experimental data (dots) and theoretical fittings (lines). Scaled doublet velocity V/V_0 is shown as a function of the strength H_0/H_1 and frequency Ω/Ω_B of the external oscillating magnetic field [32].

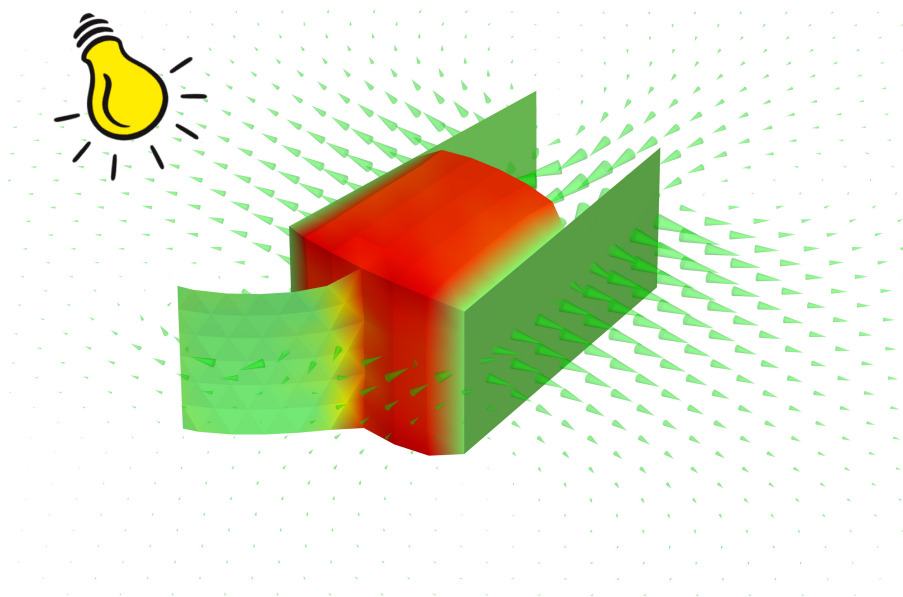


Figure 2.4: Schematic diagram illustrating a responsive gel body (red) with two propulsive flaps (green) attached to its opposite sides. The steering flap (green) at the front of the swimmer is sensitive to light (yellow), and velocity vectors through the middle of the gel body are shown by green cones. Combined with the steering flap bending, the periodic beating of the propulsion flaps could move the device forward [35].

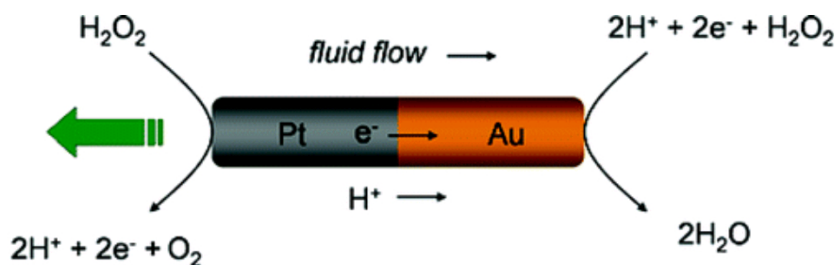


Figure 2.5: Sketch of a gold-platinum nanorod showing the mechanism for electro-kinetic process of decomposition of hydrogen peroxide [51]. Due to the decomposition of H_2O_2 at metal surfaces, an electrical current is created from Pt to Au end. Therefore, the bimetallic rod can achieve propulsion and is seen to move in the direction of the platinum end.

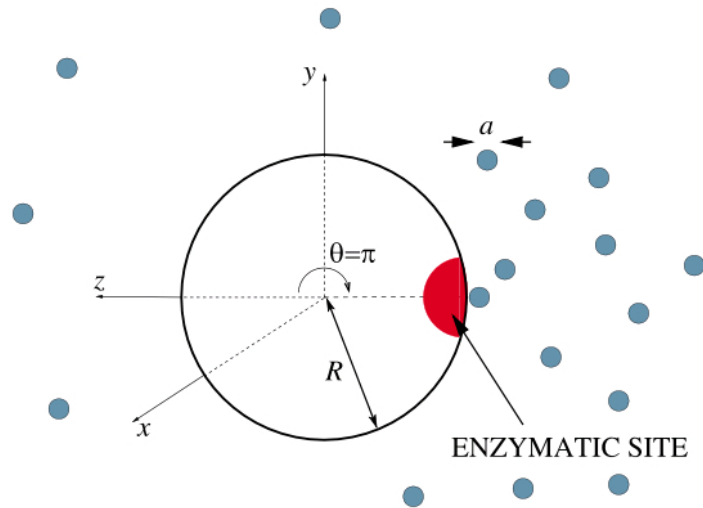


Figure 2.6: An illustration of autonomous diffusiophoretic motion of a colloid with an enzymatic site (red). The Solute molecules of diameter a are dissolved in the fluid surrounding the colloid with radius R . Due to a reaction on a catalytic patch of the surface of the colloid, an asymmetric concentration gradient of solutes is created, leading to self-propulsion for the spherical swimmer [71].

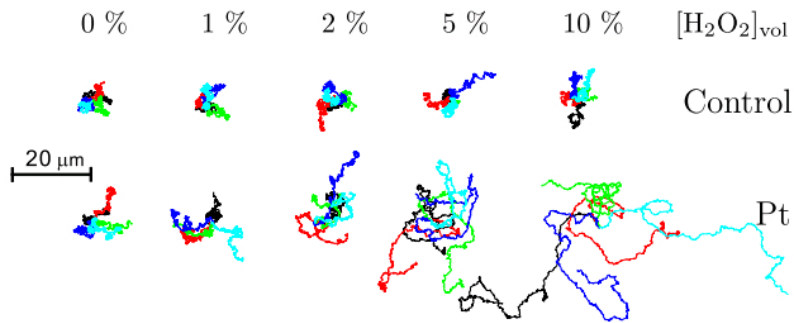


Figure 2.7: Measured displacement of both the control (blank) and platinum-coated particles suspended in different hydrogen peroxide concentrations [72]. Locomotion of $\times 5$ polystyrene beads in varying solution was recorded over 25 seconds, and the trajectory for each measurement in the same concentration is shown by different colours.

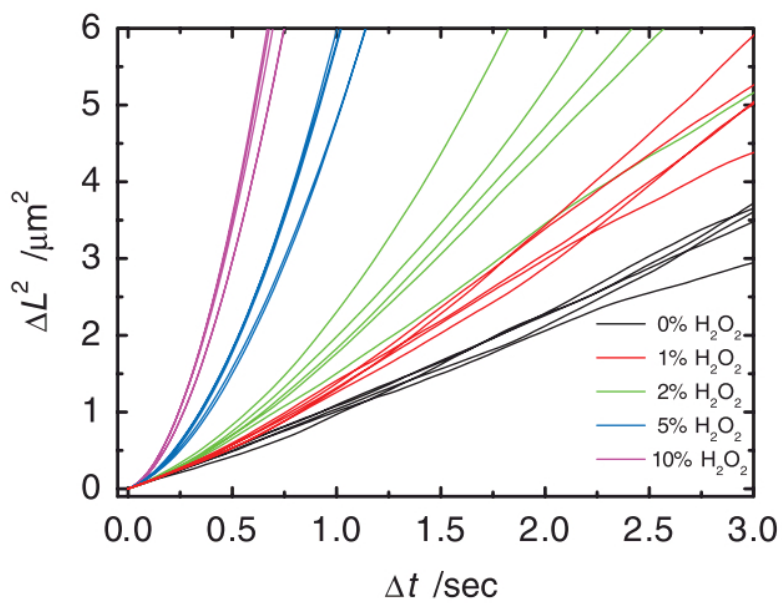


Figure 2.8: The mean squared displacements of platinum-coated particles [72]. Each colour represents different concentrations of hydrogen peroxide. The parabolic curve for high concentration of H_2O_2 indicates an enhanced diffusion.

Chapter 3

Reaction - Diffusion Model of Catalytic Colloids

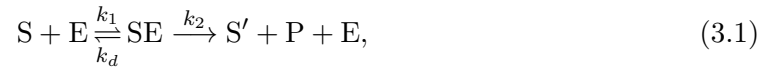
3.1 Introduction

A colloid that asymmetrically catalyses a chemical reaction powered by diffusiophoresis provides a means of self-propulsion, and this mechanism can achieve an autonomous propulsion at low Re as the time-reversal symmetry is broken. A theoretical framework has been established to investigate the behaviour of the swimming velocity of such a colloid which maintains an asymmetric configuration of solute concentration adjacent to it. The study begins with a diffusion-reaction model, followed by quantitative procedures that will estimate the influence of fuel concentration and colloid size on the propulsion velocity. Both the analytic and numerical results emphasise physical intuition and are eventually compared with experimental data.

3.2 Model of Diffusion-Reaction at Low Reynolds Number

3.2.1 Slip Velocity for Diffusion-Reaction

This chapter aims to develop a theory that models the self-propulsion achieved by an active colloid with an asymmetric catalyst on its surface. Specifically, the desire is to compute the concentration distribution, thus determining the propulsion velocity at low Reynolds numbers. Firstly, a theoretical model for diffusion-reaction, based on diffusiophoresis, is introduced. In order to obtain a full insight into the movement of an asymmetrically catalysed colloid, the factors that affect its path need to be determined. Next, the general kinetic route of the two-step reaction is considered: the reaction path that breaks substrate S into products S' and P via an intermediate process where the substrate forms the complex SE with enzyme E [73]:



where k_1 and k_2 are the corresponding rates for the two reactions. The backward reaction path in Eq. (3.1) is eliminated for simplicity, as it does not change the qualitative behaviour of the system [73]. Due to the presence of the enzyme, the chemical reaction takes place considerably quickly in the vicinity of the catalyst, and this leads to the increased production of S' and P with corresponding concentrations $C_{S'}$ and C_P , respectively.

Solute molecules interact with the surface of the colloid through intermolecular interactions, including van der Waals attractive forces, hard sphere repulsive interactions, and the hydration forces. The colloidal motion is caused by these forces, which are typically short ranged. In order to simplify the situation, a common potential W mediates these interactions between the solutes and the colloid is assumed, and the potential is considered to decay over an effective distance λ [69]. The potential between a colloid and a solute

particle is a function of their normal separation distance y [83], and its general behaviour is shown in Figure 3.1. If the potential function $W(y)$ is repulsive, then the colloid is driven to the side with lower solute concentration. The characteristic length scale λ is expected to be of the order $\mathcal{O}(\text{\AA})$, and its precise value can be computed by knowledge of solute/colloid interaction $W(y)$ [44] [84].

$$\lambda_{eff}^2 = \int_0^\infty dz z \left\{ \frac{D_S}{D_P} \left[1 - e^{-\frac{W_P(z)}{k_B T}} \right] + \frac{D_S}{D_{S'}} \left[1 - e^{-\frac{W_{S'}(z)}{k_B T}} \right] - \left[1 - e^{-\frac{W_S(z)}{k_B T}} \right] \right\} \quad (3.2)$$

Here, k_B is Boltzmann constant, T denotes the absolute temperature, and D indicates diffusion coefficient.

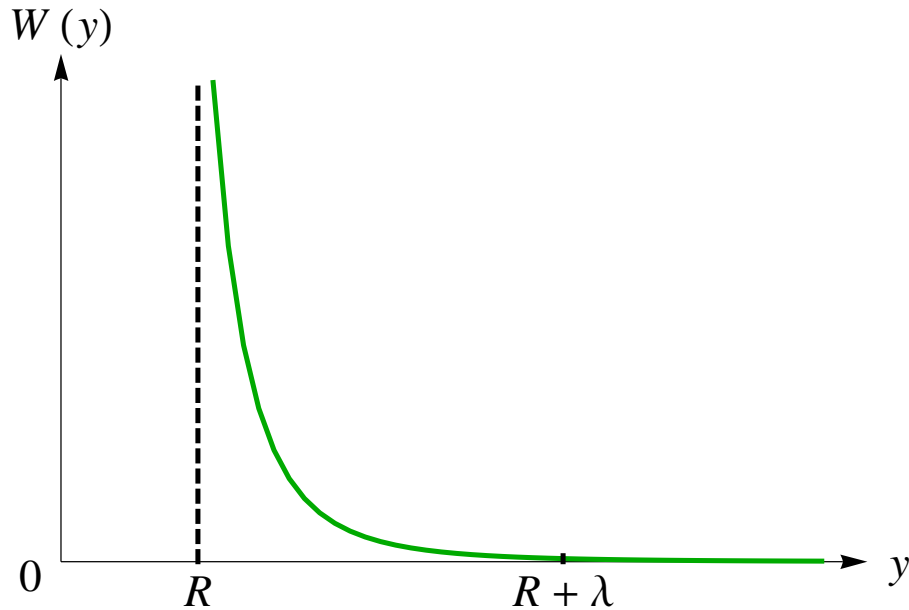


Figure 3.1: Decay of hypothetical potential $W(y)$ in the diffused layer (slipping plane) with thickness λ .

The flow field is divided into inner and outer regions with different length scales, λ and R respectively. As a result, the inner region can be considered as a plate and boundary layer concept is applied. In this scheme, the thickness λ of the interface between colloid and fluid molecules is much smaller than the size of the colloid R . A solute molecule is

experienced a force $-C\nabla W(y)$, that is proportional to the local solute concentration C and the radial gradient of the potential $\nabla W(y)$, and this leads to a pressure p in the thin layer. As the interaction of the solute to the particle is increasing along the side of higher solute concentration, a diffusive flux of solute is produced from the higher concentration side to the lower one. Then this streaming flow across the interface causes a relative motion with a slip velocity \mathbf{v}_s , which is tangential to the plate, at the edge of the inner region [44]. The slip velocity has different behaviours on different length scales. While the slip velocity is continuous within an interfacial layer, it becomes discontinuous on the scale of the colloid size.

A model for the slip velocity due the interaction between the solutes and the colloid is developed by Derjaguin et al. and Anderson [44] [69], and this movement is related to the solute concentration in a local coordinate where y is the normal variation to the surface of the colloid. At the equilibrium, the local solute concentration in the inner region can be represented by Boltzmann distribution:

$$C(y, \theta) = C^S(\theta) \exp \frac{-W(y)}{k_B T}, \quad (3.3)$$

where θ is the lateral angle in the spherical coordinate, and $C^S(\theta)$ is the concentration along the surface at the outer edge of the slipping plane. It is important that the momentum transferred between solute molecules and the colloid is conserved within the inner region (both x- and y-directions). In the limit $\lambda/R \ll 1$, the boundary-layer approximation applies to the Stokes equations.

$$\frac{\partial p}{\partial y} + C \frac{\partial W(y)}{\partial y} = 0, \quad (3.4)$$

$$\eta \frac{\partial^2 v_x}{\partial z^2} - \frac{\partial p}{\partial x} = 0 \quad (3.5)$$

Here, p is the pressure field, η denotes the viscosity of the solvent, and \mathbf{v}_x means the x-component of the slip velocity. Combining the preceding equations gives the formula

for the slip velocity in a solution of nonelectrolyte solutes with concentration gradient ∇C [69], and the resulting slip velocity along the surface is described in Eq. (3.6) and Figure 3.2.

$$\mathbf{v}_s = \frac{k_B T}{\eta} \int_0^\infty dy y \left[1 - \exp\left(\frac{-W_j(y)}{k_B T}\right) \right] \frac{\partial C}{\partial x} \quad (3.6)$$

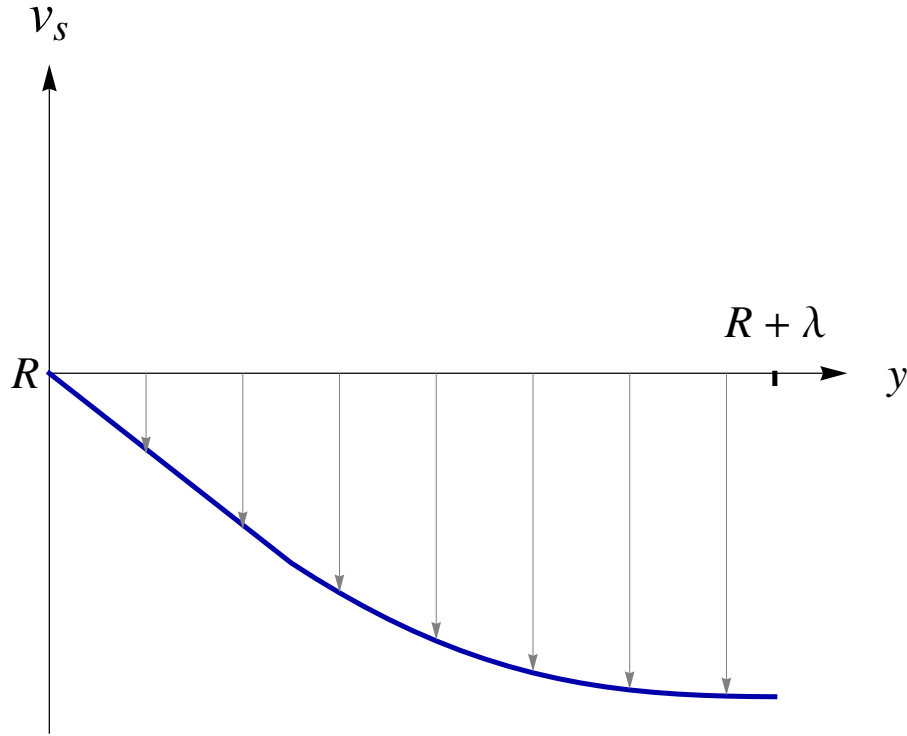


Figure 3.2: The slip velocity \mathbf{v}_s is a function of normal distance from the colloidal surface y .

Alternatively, a slip velocity of the solute particle passing by the colloid at position \mathbf{r}_s somewhere within the interface can be expressed in terms of a coefficient μ :

$$\mathbf{v}_s = \mu_j(r_s)(\mathbf{I} - \mathbf{nn}) \cdot \nabla C_j(r_s), \quad (3.7)$$

$$\mu_j(r_s) = \frac{k_B T}{\eta} \int_0^\infty dy y \left[1 - \exp\left(\frac{-W_j(y)}{k_B T}\right) \right]. \quad (3.8)$$

Here, the unit vector \mathbf{n} is normal to the surface, \mathbf{I} denotes the identity tensor, and $\mathbf{I} - \mathbf{nn}$

gives the tangent direction. $W_j(y)$ indicates the intermolecular potential between the j th diffused molecules and the surface of the colloid [44]. The coefficient between the slip velocity and a concentration gradient $\mu_j(r_s)$ is defined as a local mobility for the solute species j , and is controlled by the interaction of the solute molecules with the surface of the colloid [44]. In the reaction-diffusion framework, a slip velocity is influenced by all the solute species, including substrate and product particles at position \mathbf{r}_s on the surface [44] [69].

$$\begin{aligned} \mathbf{v}_s(r_s) &= \mu_S(r_s)(\mathbf{I} - \mathbf{nn}) \cdot \nabla C_S(r_s) + \mu_P(r_s)(\mathbf{I} - \mathbf{nn}) \cdot \nabla C_P(r_s) \\ &+ \mu_{S'}(r_s)(\mathbf{I} - \mathbf{nn}) \cdot \nabla C_{S'}(r_s) \end{aligned} \quad (3.9)$$

After introducing the idea of slip velocity, the configuration of a colloid suspended in solute molecules is depicted in Figure 3.3.

Furthermore, a lateral slip velocity \mathbf{v}_s due to the depletion of the product particles within the interface produces a net drift motion of the colloid, and the net drift velocity \mathbf{V} can be formulated from the overall slip velocity [82] [85] [86]:

$$\mathbf{V} \cdot \hat{\mathbf{f}}_i = - \int \int dr_s \mathbf{n} \cdot \sigma_i \cdot \mathbf{v}_s(r_s), \quad (3.10)$$

where σ_i is the hydrodynamic stress tensor at the surface and $\hat{\mathbf{f}}_i$ represents an applied unit force. The Eqs. (3.9) – (3.10) are applied to any shape of swimmer. In the following section, the focus is placed on an asymmetrically catalysed sphere with radius R . For a sphere, the net drift velocity described in Eq. (3.10) can be deduced [82] [87]:

$$\mathbf{n} \cdot \sigma_i = \frac{1}{4\pi R^2} \hat{\mathbf{f}}_i, \quad (3.11)$$

$$\mathbf{V} = - \frac{1}{4\pi R^2} \int \int dr_s \mathbf{v}_s(r_s). \quad (3.12)$$

Once the concentration profile is known, the velocity distribution of the spherical swimmer

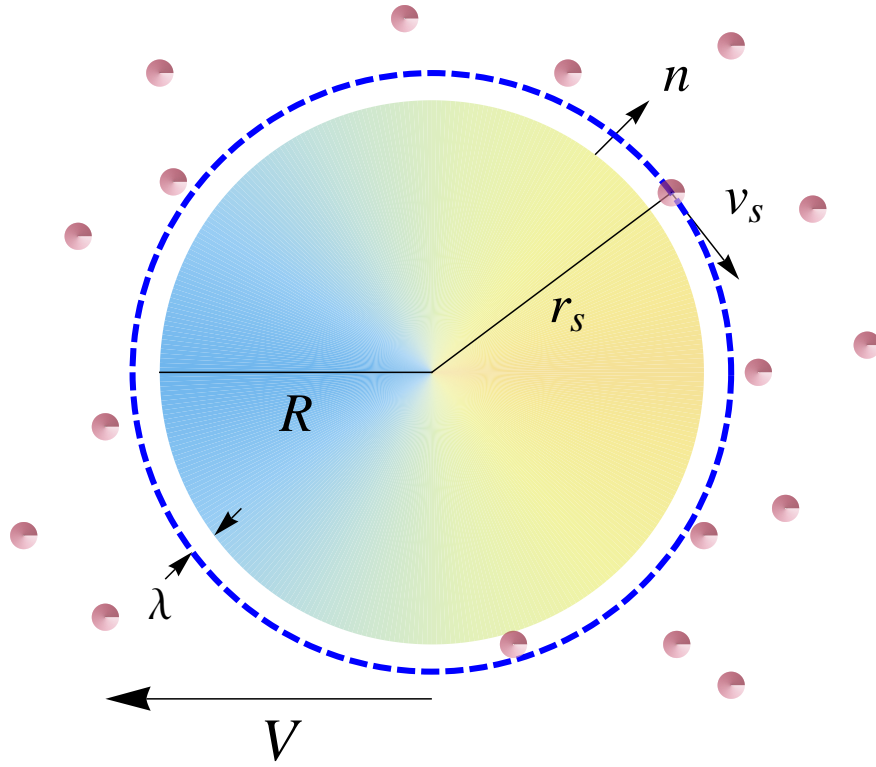
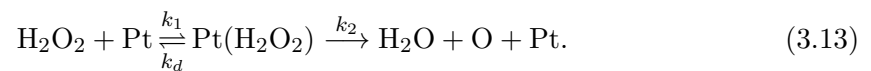


Figure 3.3: Schematic of active colloid with radius R suspended in fluid molecules. The slipping velocity \mathbf{v}_s is induced by the flux of solute molecules at position \mathbf{r}_s within the interface, and the slipping plane is shown as the dashed circle with length scale λ . An inhomogeneous distribution of solutes drives the motion of colloid with the translation velocity V .

can be determined.

3.2.2 Reaction-Diffusion Process of the Fuel Molecules

The diffusion-reaction model proposed in [73] assumes that the kinetic route for the chemical reaction taking place in the vicinity of the enzyme is a two-step reaction:



The migration of colloid dispersed in a fluid under the action of a concentration gradient is far from equilibrium, and the solute diffusion time can be computed by scale analysis. Because the particles of interest are micron size and the diffusion coefficients for solute species D are of the order $10^{-9} m^2/s$, diffusion time is estimated as $[T] = [L]^2/[D] \sim 10^{-3} s$. In addition, the the motion of the colloid powered by diffusiophesis is less than $10 \mu m/s$ [72], which is much slower than the the solute diffusion. In this situation, a separation of time scale between the diffusion of solute species and the propulsion of the colloid is considered [79], and this indicates that the system of reaction-diffusion process achieves a steady state. Therefore, the transition involving the binding of the substrate from the solution is assumed to proceed at a rate k_1 . The diffusion-reaction equations for the three species read

$$-D_{\text{hp}}\nabla^2 C_{\text{hp}} = -k_1 C_{\text{hp}} C_{\text{E}}, \quad (3.14)$$

$$-D_{\text{w}}\nabla^2 C_{\text{w}} = k_2 C_{\text{SE}}, \quad (3.15)$$

$$-D_{\text{o}}\nabla^2 C_{\text{o}} = k_2 C_{\text{SE}}, \quad (3.16)$$

at the steady state. In the above equations, hp indicates hydrogen peroxide, w denotes water, and o means oxygen. C_{α} and D_{α} are the concentration and diffusion constant for each species, respectively. C_{E} is the (volume) density of the unoccupied enzymatic regions, and C_{SE} represents the density of the occupied regions where the substrate forms a complex with the enzyme. At a steady state, the effective rates of the two processes should balance each other, and this imposes a constraint to the equations:

$$k_1 C_{\text{hp}} C_{\text{E}} = k_2 C_{\text{SE}}. \quad (3.17)$$

From integrating the three diffusion equations above, we have:

$$D_{\text{hp}}C_{\text{hp}} + D_{\text{w}}C_{\text{w}} = D_{\text{hp}}C_{\infty}, \quad (3.18)$$

$$D_{\text{hp}}C_{\text{hp}} + D_{\text{o}}C_{\text{o}} = D_{\text{hp}}C_{\infty}, \quad (3.19)$$

$$D_{\text{w}}C_{\text{w}} = D_{\text{o}}C_{\text{o}}, \quad (3.20)$$

where, C_{∞} is the concentration at infinity. Therefore, the concentrations of the products C_{w} and C_{o} are the function of C_{hp} :

$$C_{\text{w}} = \frac{D_{\text{hp}}}{D_{\text{w}}}(C_{\infty} - C_{\text{hp}}), \quad (3.21)$$

$$C_{\text{o}} = \frac{D_{\text{hp}}}{D_{\text{o}}}(C_{\infty} - C_{\text{hp}}). \quad (3.22)$$

The concentrations of the products can be calculated as long as the concentration profile of hydrogen peroxide is obtained.

Using the notation $C_{\text{hp}} \equiv [\text{H}_2\text{O}_2]$ and $C_{\text{o}} \equiv [\text{O}_2]$, the steady state diffusion–reaction equations for the reaction can be rewritten as

$$\nabla^2 C_{\text{hp}}(r, \theta) = 0, \quad \nabla^2 C_{\text{o}}(r, \theta) = 0, \quad (3.23)$$

subject to the boundary conditions

$$D_{\text{hp}}\partial_r C_{\text{hp}}|_{r=R} = k_1 C_{\text{hp}}(R, \theta) p_{\text{fr}} K(\theta), \quad (3.24)$$

$$D_{\text{o}}\partial_r C_{\text{o}}|_{r=R} = -k_2 p_{\text{cx}}(\theta) K(\theta), \quad (3.25)$$

where $K(\theta)$ is the “coverage” function that described how the angular pattern of the platinum patch(es) cover the surface of the colloid. For instance, the coverage function of a Janus sphere has a simple form:

$$K(\theta) = \begin{cases} 1, & \text{if } 0 < \theta < \frac{\pi}{2} \\ 0, & \text{if } \frac{\pi}{2} < \theta < \pi. \end{cases}$$

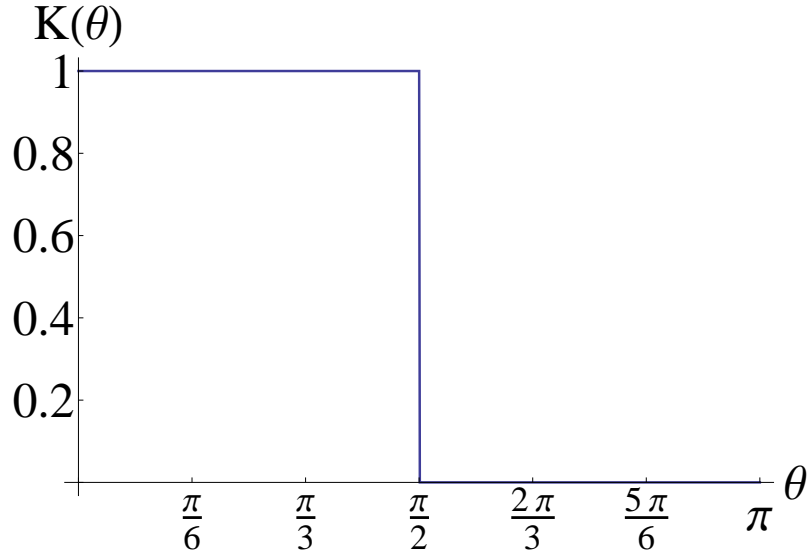


Figure 3.4: The coverage function $K(\theta)$ for a Janus sphere.

The angular pattern of the catalyst coating on the Janus sphere is shown in Figure 3.4. If a distribution of catalyst is coated unevenly on surface of a sphere, such colloid is regarded as an inhomogeneous sphere. Figures 3.5 – 3.6 are illustrated as three examples of coverage function for inhomogeneous spheres. These inhomogeneous coverage functions are chosen because they are simple in terms of Legendre polynomials.

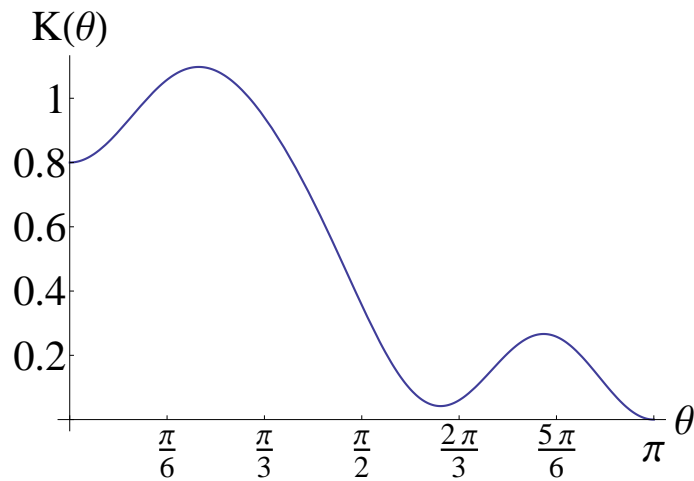


Figure 3.5: The coverage function $K(\theta)$ for inhomogeneous case 1.

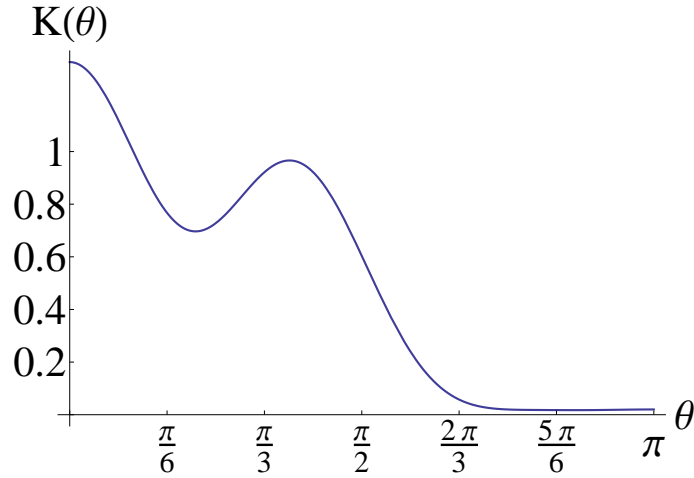


Figure 3.6: The coverage function $K(\theta)$ for inhomogeneous case 2

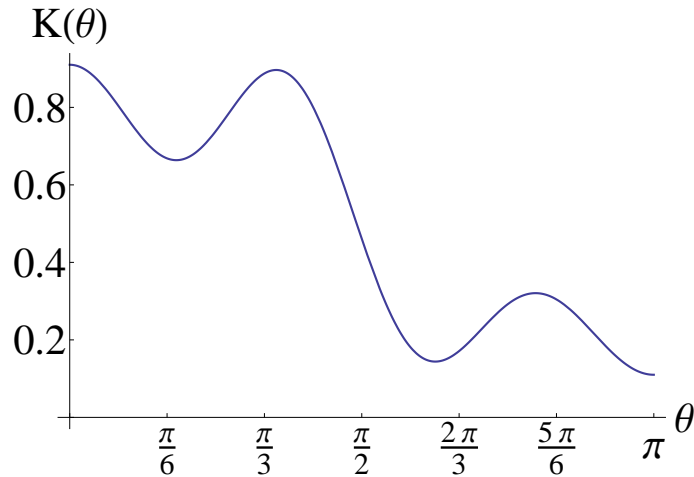


Figure 3.7: The coverage function $K(\theta)$ for inhomogeneous case 3

In addition, the enzyme spends a certain fraction p_{fr} of its time unoccupied or free, and the rest $p_{\text{cx}} = 1 - p_{\text{fr}}$ is bound to the substrate. Both p_{fr} and p_{cx} are nearly constant in time and this means the enzyme converts the substrate at a constant rate, which needs to be found. In fact, the enzyme remains unchanged throughout the chemical reaction, and the concentrations of the platinum in a free or occupied state can be represented by the probability in either state multiplying the total concentration of the enzyme in all states

C_E^0 .

$$p_{\text{fr}} + p_{\text{cx}} = 1, \quad (3.26)$$

$$C_E + C_{\text{SE}} = C_E^0 = \frac{N_E^0}{4\pi R^2} \delta(r - R), \quad (3.27)$$

$$C_{\text{SE}} = p_{\text{fr}}(\theta) C_E^0, \quad (3.28)$$

$$C_E = p_{\text{cx}}(\theta) C_E^0, \quad (3.29)$$

where, N_E^0 is the total number of enzyme molecules. Based on the Eqs. (3.26) – (3.29), the balanced relation Eq. (3.17) can be rewritten in the following way:

$$1 - p_{\text{fr}} = \frac{k_1}{k_2} p_{\text{fr}} C_{\text{hp}}(r, \theta). \quad (3.30)$$

Solving this equation gives the probability of being in a free state as

$$p_{\text{fr}} = \frac{k_2}{k_2 + k_1 C_{\text{hp}}}. \quad (3.31)$$

Then the boundary condition in Eq. (3.24) can be expressed as

$$D_{\text{hp}} \partial_r C_{\text{hp}}|_{r=R} = \frac{k_2 k_1 C_{\text{hp}}(R, \theta)}{k_2 + k_1 C_{\text{hp}}(R, \theta)} K(\theta). \quad (3.32)$$

For a sphere of radius R with azimuthally symmetric patterns, the surface quantities only depend on the latitude angle θ . If the diffusion coefficient is a constant, the steady state diffusion-reaction reduces to the Laplace equation. These allow us to expand the concentration of hydrogen peroxide in terms of Legendre polynomials as:

$$C_{\text{hp}}(r, \theta) = C_\infty \left[1 - \sum_{l=0}^{\infty} B_l \left(\frac{R}{r} \right)^{l+1} P_l(\cos \theta) \right], \quad (3.33)$$

where C_∞ is the concentration at infinity and B_l is an unknown coefficient. When the concentration profile described above is applied, the boundary condition in Eq. (3.32) can

be represented in this way:

$$\begin{aligned} \sum_{l=0}^{\infty} B_l(l+1)P_l(\cos\theta) &= -\frac{k_2 k_1 C_{hp}}{k_2 + k_1 C_{hp}} K(\theta) \\ &= \frac{\left(\frac{k_1 R}{D_{hp}}\right) [1 - \sum_l B_l P_l]}{1 + \left(\frac{k_1 C_{\infty}}{k_2}\right) [1 - \sum_l B_l P_l]} K(\theta). \end{aligned} \quad (3.34)$$

Here, the coverage function $K(\theta)$ could also be expanded by Legendre polynomials [88]

$$K(\theta) = \sum_{l=0}^{\infty} F_l P_l(\cos\theta), \quad (3.35)$$

and where

$$F_l = -\left(\frac{1}{2}\right)^{\frac{l-1}{2}} \frac{(2l+1)(l-2)!!}{4\left(\frac{l+1}{2}\right)!}. \quad (3.36)$$

Expressing the preceding arguments for the boundary condition is a new formula in B_l involved with Legendre polynomials:

$$\begin{aligned} \frac{k_1 C_{\infty}}{k_2} \sum_{l,m=0}^{N_{max}} B_l B_m (l+1) \left(\frac{2n+1}{2}\right) G_{lmn} - \frac{k_1 R}{D_{hp}} \sum_{l,m=0}^{N_{max}} B_l F_m (l+1) \left(\frac{2n+1}{2}\right) G_{lmn} \\ + \frac{k_1 R}{D_{hp}} F_n - \left(1 + \frac{k_1 C_{\infty}}{k_2}\right) B_n (n+1) = 0. \end{aligned} \quad (3.37)$$

Here, G_{lmn} is a Legendre polynomial triple product integral

$$G_{lmn} = \int_{-1}^1 P_l(x) P_m(x) P_n(x) dx. \quad (3.38)$$

Eq. (3.37) is a nonlinear and quadratic equation in B_l which needs solving for B_l in order to have a full picture of the concentration profile $C_{hp}(r, \theta)$. The unknown coefficient B_l is a function of $\frac{k_1 C_{\infty}}{k_2}$ and $\frac{k_1 R}{D_{hp}}$. Basically, the summations in Eq. (3.37) should be calculated from 0 to ∞ , but there will be infinite solutions for B_l . To simplify the problem, N_{max} was chosen as the upper limit of these summations ($0 \leq l, m, n \leq N_{max}$). When the values of $\frac{k_1 C_{\infty}}{k_2}$ and $\frac{k_1 R}{D_{hp}}$ are chosen, there will be a new set of equations in $B_0, B_1, \dots, B_{N_{max}}$.

In general, there will be more than one set of solutions for $B_0, B_1, \dots, B_{N_{max}}$ depending on the value of N_{max} . If this situation happens, a method of constraints is needed to select which set of $B_0, B_1, \dots, B_{N_{max}}$ is of interest. Therefore, two facts of the concentration of $[\text{H}_2\text{O}_2]$ are taken into account. One fact is that the surface concentration of hydrogen peroxide $C_{\text{hp}}(R, \theta)$ is less than the concentration at infinity C_∞ . The other is that $C_{\text{hp}}(R, \theta)$ is always positive. These provide a new constraint for the surface concentration $C_{\text{hp}}(R, \theta)$:

$$1 > \sum_{l=0}^{N_{max}} B_l P_l(\cos \theta) > 0. \quad (3.39)$$

For the two special cases where $\theta = 0$ and π , then the constraint in Eq. (3.39) has the following forms:

$$1 > \sum_{l=0}^{N_{max}} B_l P_l(1) > 0, \quad (3.40)$$

$$1 > \sum_{l=0}^{N_{max}} B_l P_l(-1) > 0. \quad (3.41)$$

Using the formula described above, the unknown variable B_l in Eq. (3.37) can be numerically solved as long as the set of solutions is satisfied with the two constraints in Eqs. (3.40) and (3.41). Now, a complete distribution has been achieved for the concentration profile and its gradient that were created by the two-step reaction between the solute and the enzyme. As a result, the velocity of the spherical swimmer can be evaluated in terms of $\frac{k_1 C_\infty}{k_2}$ and $\frac{k_1 R}{D_{\text{hp}}}$. By analysing the mobilities of the substrate and the two products, it is found that the velocity of the swimmer is only dependent on $B_1(\frac{k_1 C_\infty}{k_2}, \frac{k_1 R}{D_{\text{hp}}})$:

$$\begin{aligned} \mathbf{V}(\frac{k_1 C_\infty}{k_2}, \frac{k_1 R}{D_{\text{hp}}}) &= -\frac{2}{3} \frac{D_{\text{hp}} C_\infty}{R} \left[\frac{\mu_w}{D_w} + \frac{\mu_o}{D_o} - \frac{\mu_{\text{hp}}}{D_{\text{hp}}} \right] B_1(\frac{k_1 C_\infty}{k_2}, \frac{k_1 R}{D_{\text{hp}}}) \\ &= -V_0 \frac{2}{3} \frac{D_{\text{hp}} C_\infty}{k_2 R} B_1(\frac{k_1 C_\infty}{k_2}, \frac{k_1 R}{D_{\text{hp}}}), \end{aligned} \quad (3.42)$$

$$V_0 = \left[\frac{\mu_w}{D_w} + \frac{\mu_o}{D_o} - \frac{\mu_{\text{hp}}}{D_{\text{hp}}} \right] k_2, \quad (3.43)$$

where, V_0 is the velocity scale.

3.2.3 Scaling Region for Propulsion Velocity

By solving Eq. (3.34) numerically, both the B_1 and velocity are the function of the size of the colloid as well as the fuel concentration in the fluid. The theoretical prediction of the propulsion velocity is of a Janus sphere, which has a hemispherical coating of catalyst and is a special case. For a Janus sphere, the coefficient B_1 becomes a constant in the large size limit when $R \gg D_{\text{hp}}/k_1$ and $R \gg D_{\text{hp}}C_\infty/k_2$. In the limit $R \ll D_{\text{hp}}/k_1$ and $R \gg D_{\text{hp}}C_\infty/k_2$, B_1 the swimming velocity is size-independent due to $B_1 \simeq \frac{3k_1R}{8D_{\text{hp}}}$. When $R \ll D_{\text{hp}}/k_1$ and $R \ll D_{\text{hp}}C_\infty/k_2$, $B_1 \simeq \frac{3k_2R}{8D_{\text{hp}}C_\infty}$, the velocity does not depend on the radius R . The magnitude of velocity for the Janus sphere has two asymptotic forms at small R or in the large R limit.

$$V\left(\frac{k_1C_\infty}{k_2}, \frac{k_1R}{D_{\text{hp}}}\right) \sim \begin{cases} R - \text{independent,} & \text{if } \frac{k_1R}{D_{\text{hp}}} \ll 1 \\ \frac{1}{R}, & \text{if } \frac{k_1R}{D_{\text{hp}}} \gg 1 \end{cases}$$

After appropriate scaling, the propulsion velocity in Eq. (3.42) can be represented as a function of the thermal energy $k_B T$, viscosity η and an effective Derjaguin length λ_{eff} [69]. The swimming velocity exhibits different behaviour in different limits and the corresponding regions are summarised in Figure 3.8.

To obtain the behaviour of the swimming velocity of an inhomogeneous sphere, a similar procedure is adopted as for the problem. According to Eq. (3.34) and Eq. (3.42), the behaviour of both the B_1 and velocity at different limits of R can be predicted. In the large size limit when $R \gg D_{\text{hp}}/k_1$ and $R \gg D_{\text{hp}}C_\infty/k_2$, Eq. (3.34) becomes

$$\sum_{l=0}^{\infty} B_l(l+1)P_l(\cos\theta) = \frac{k_1R}{D_{\text{hp}}} \left[1 - \sum_l B_l P_l \right] K(\theta). \quad (3.44)$$

Note that the summation of the right hand side of Eq. (3.34) is always finite, and this

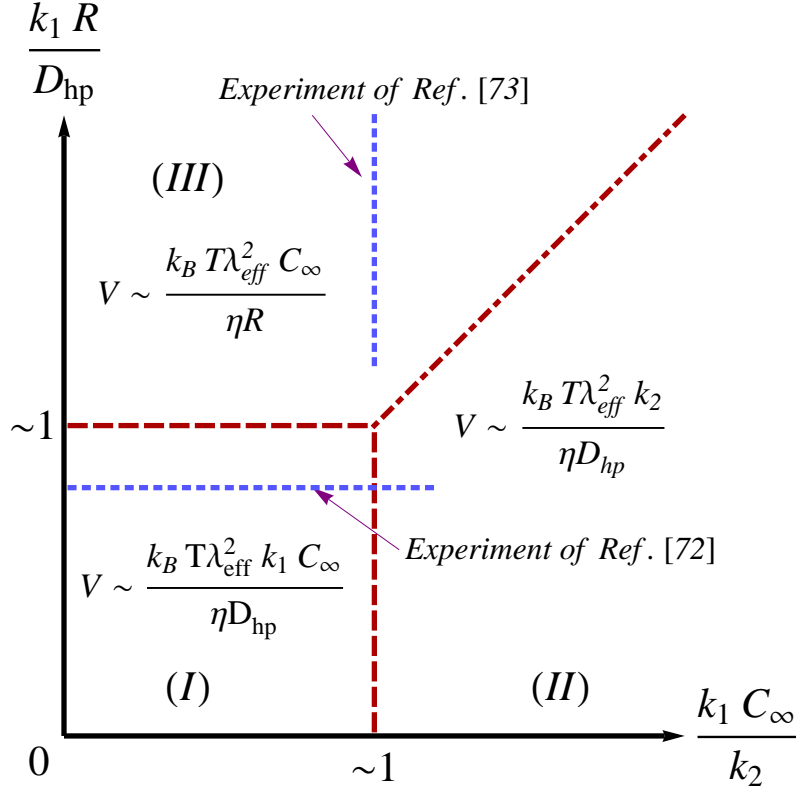


Figure 3.8: Three scaling regions for the propulsion velocity of a Janus sphere as a function of the size and fuel concentration. The crossover boundaries between these three regimes are presented by red dashed lines, and blue dotted lines indicate the locations which correspond to the previous experiments of Ref. [72] [73]. The red diagonal dot-dashed line means the crossover between regime II and III remains implicit.

can be achieved via small $[1 - \sum_l B_l P_l]$ with $B_1 \sim 1/R$ for any positive coverage function $K(\theta)$. In the limit $R \ll D_{\text{hp}}/k_1$ and $R \gg D_{\text{hp}}C_\infty/k_2$, B_1 is proportional to the size scale R and this relation indicates that the swimming velocity is independent of R . Similarly, when $R \ll D_{\text{hp}}/k_1$ and $R \ll D_{\text{hp}}C_\infty/k_2$, Eq. (3.34) can be expressed as

$$\sum_{l=0}^{\infty} B_l (l+1) P_l(\cos \theta) = \frac{k_2 R}{D_{\text{hp}} C_\infty} K(\theta). \quad (3.45)$$

Therefore, the relationship between B_1 and R is also linear.

The prediction of the speed for an inhomogeneous sphere is summarised as follows and shown in Figure 3.9.

$$V\left(\frac{k_1 C_\infty}{k_2}, \frac{k_1 R}{D_{\text{hp}}}\right) \sim \begin{cases} R - \text{independent,} & \text{if } \frac{k_1 R}{D_{\text{hp}}} \ll 1 \\ \frac{1}{R^2}, & \text{if } \frac{k_1 R}{D_{\text{hp}}} \gg 1 \end{cases}$$

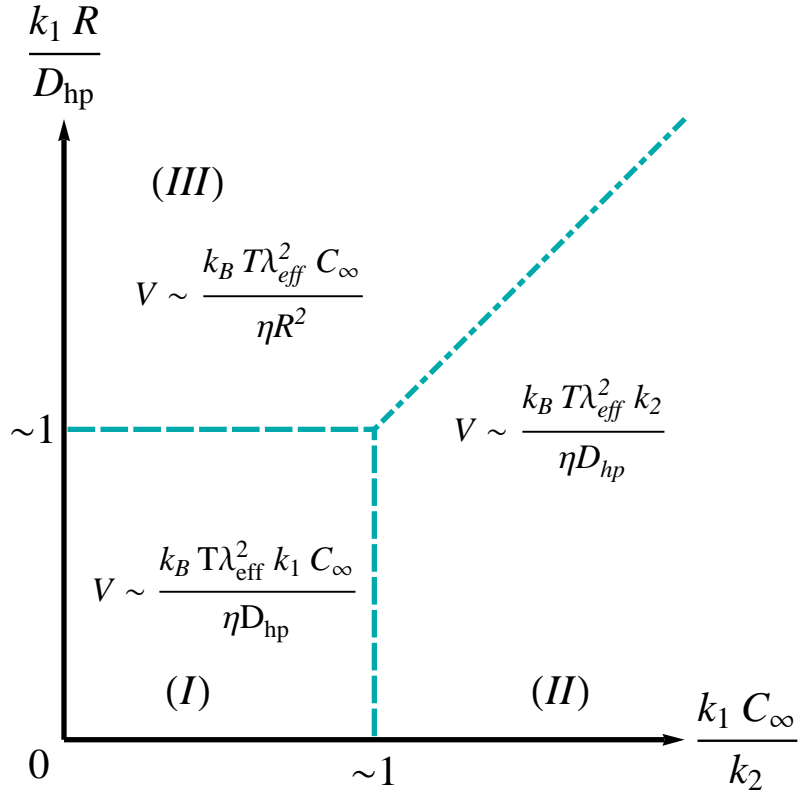


Figure 3.9: Three scaling regions for the propulsion velocity of an inhomogeneous sphere as a function of the size and fuel concentration. Blue dashed and diagonal dot-dashed lines show the crossover boundaries between regimes I, II and III.

3.3 Results

3.3.1 Janus Sphere

First of all, a Janus sphere was considered as its coverage function $K(\theta)$ has a simple form. When the two parameters $\frac{k_1 C_\infty}{k_2}$ and $\frac{k_1 R}{D_{\text{hp}}}$ were given, the propulsion velocity of the

swimmer was estimated by solving Eq. (3.37) for B_l numerically. Note that the propulsion velocity is only controlled by the term containing the B_1 coefficient, hence the numerical solution of B_1 plays a vital role in the analysis.

For larger N_{max} , the Eq. (3.37) starts to be more complex. The small value of N_{max} is insufficient to offer a stable solution of B_l and increasing N_{max} is the only way to achieve an adequate solution for these nonlinear equations. In effect, the value of N_{max} used in the code is between 8 and 20. Figure 3.10 indicates that the B_1 is proportional to the size scale R , but becomes a constant at the large size limit.

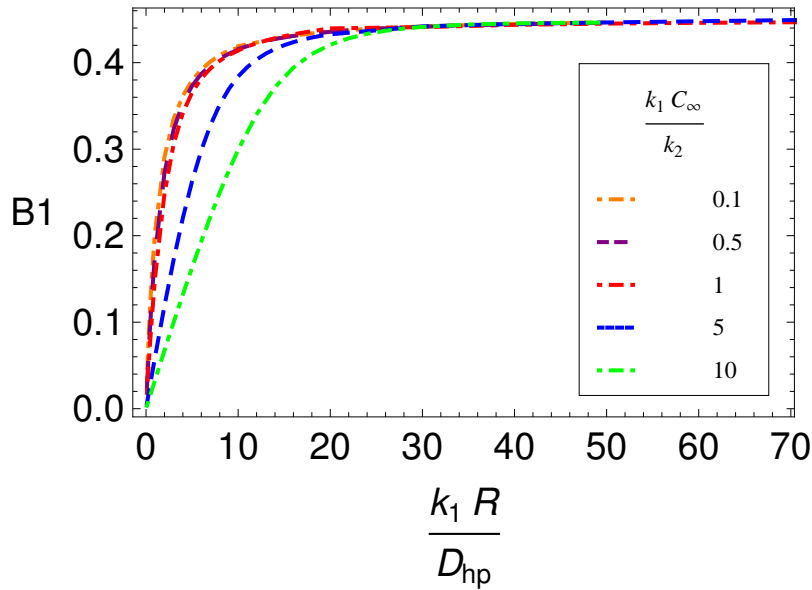


Figure 3.10: For a Janus sphere, the B_1 coefficient that determines the swimming velocity is a function of size parameter $\frac{k_1 R}{D_{hp}}$ at constant values of $\frac{k_1 C_\infty}{k_2}$. The colourful lines indicate different fuel concentrations $\frac{k_1 C_\infty}{k_2}$ ranging from 0.1 to 10.

Having tested the effect of various fuel concentrations and sizes on B_l , the full distribution of the concentration of hydrogen peroxide C_{hp} can be found from Eq. (3.33), and

the surface concentration $C_{\text{hp}}(R, \theta)$ for different parameters $\frac{k_1 C_\infty}{k_2}$ and $\frac{k_1 R}{D_{\text{hp}}}$ is plotted with respect to θ in Figure 3.11.

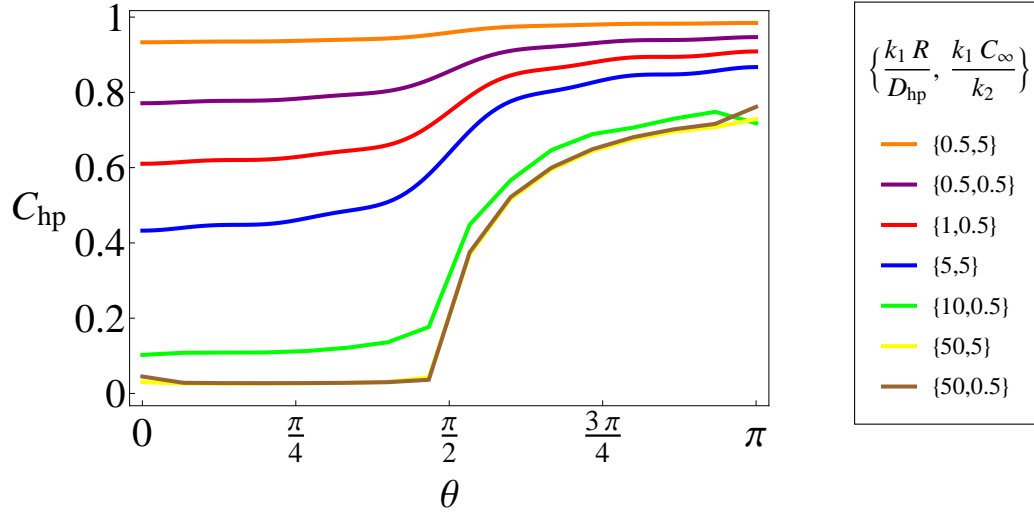


Figure 3.11: The surface concentration of hydrogen peroxide $C_{\text{hp}}(R, \theta)$ is a function of the latitude angle θ . Coloured lines in the legend present different parameters for size and fuel concentration.

The data in Figure 3.11 reflects that there is a depletion in the surface concentration of hydrogen peroxide in the region $0 < \theta < \pi/2$ due to the fixed enzymatic area on the surface of the Janus sphere. Note that the size parameter $\frac{k_1 R}{D_{\text{hp}}}$ has a direct association to the radius of the sphere. If the size of the swimmer is quite small, this corresponds to the case where the depletion zone disappears. For the two cases $\frac{k_1 R}{D_{\text{hp}}} = 50$, $\frac{k_1 C_\infty}{k_2} = 5$ and $\frac{k_1 R}{D_{\text{hp}}} = 50$, $\frac{k_1 C_\infty}{k_2} = 0.5$, the two sets of data fluctuate considerably in the region $\pi/2 < \theta < \pi$, hence the data is transformed into a frequency domain by a Fourier transform for frequency filtering, then followed by an inverse transform to return to the original space.

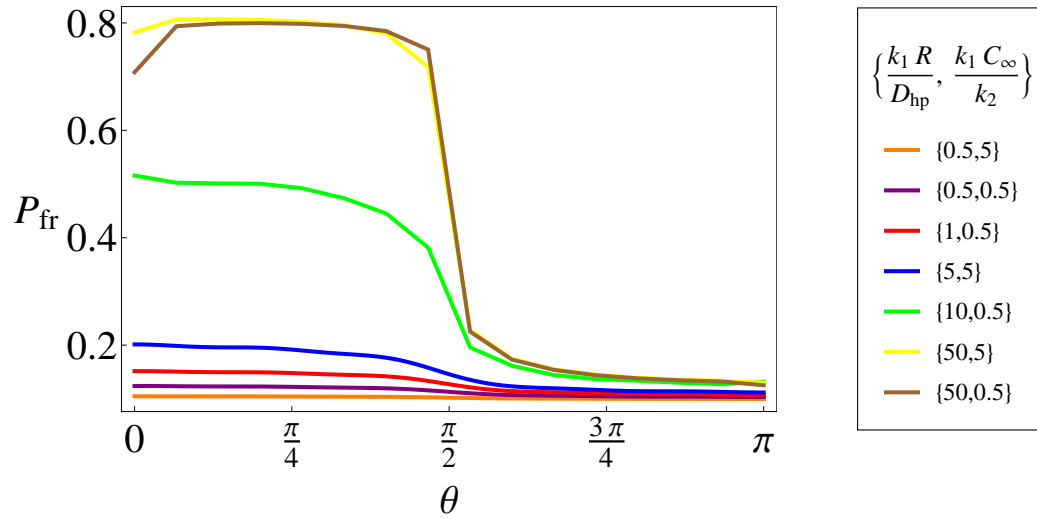


Figure 3.12: The surface probability for the unoccupied state p_{fr} is a function of the latitude angle θ , and this basically reflects the catalyst geometry of a Janus sphere. Various parameters of size and fuel concentration are shown by different coloured lines.

In the experiment demonstrated by [72], the rates for the reaction in Eq. (3.13) are calculated as $k_1 = 4.4 \times 10^{11} \mu\text{m}^{-2}\text{s}^{-1}$, and $k_2 = 4.8 \times 10^{10} \mu\text{m}^{-2}\text{s}^{-1}$. Then the surface probability for the unoccupied state p_{fr} can be calculated from Eq. (3.31) and shown in Figure 3.12. In essence, the distribution of the surface probability reflects the pattern of coverage function $K(\theta)$ for a Janus sphere.

Figures 3.13 – 3.14 are 3D colour-map presentations which display the concentrations of the substrate/product particles and clearly reveal the depletion/accumulation zones around the coated area during the reaction process. The corresponding contour plots for the substrate and product particles are also illustrated in Figures 3.15 – 3.16.

Furthermore, the velocity distributions for the Janus sphere are shown in Figures 3.17

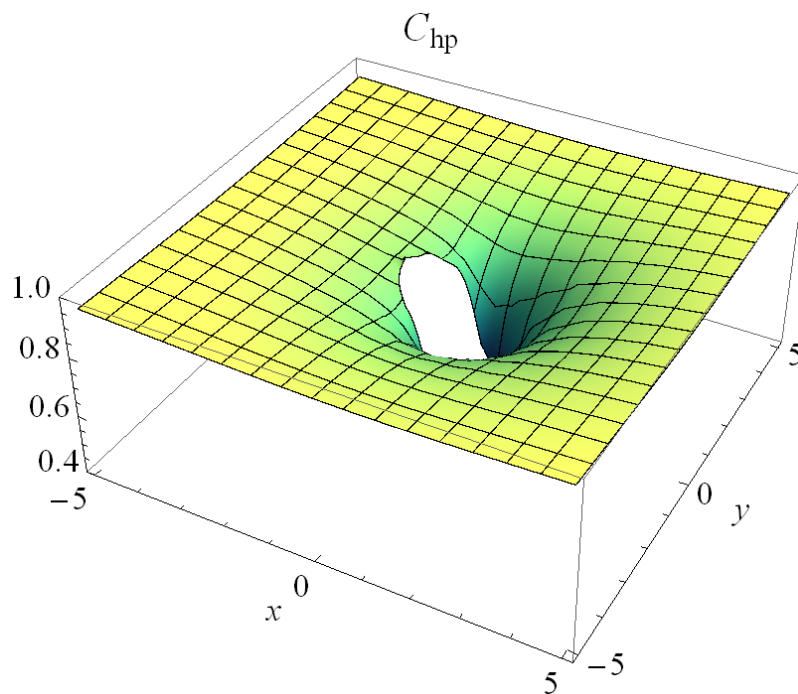


Figure 3.13: The concentration profile of hydrogen peroxide C_{hp} for a Janus sphere in 3D.

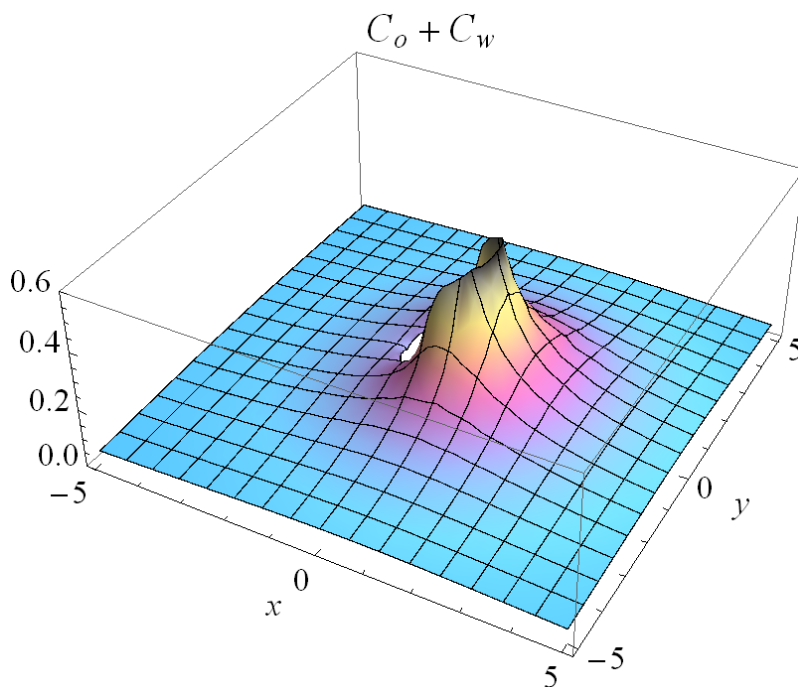


Figure 3.14: The concentration profile of the products (water and oxygen) for a Janus sphere in 3D.

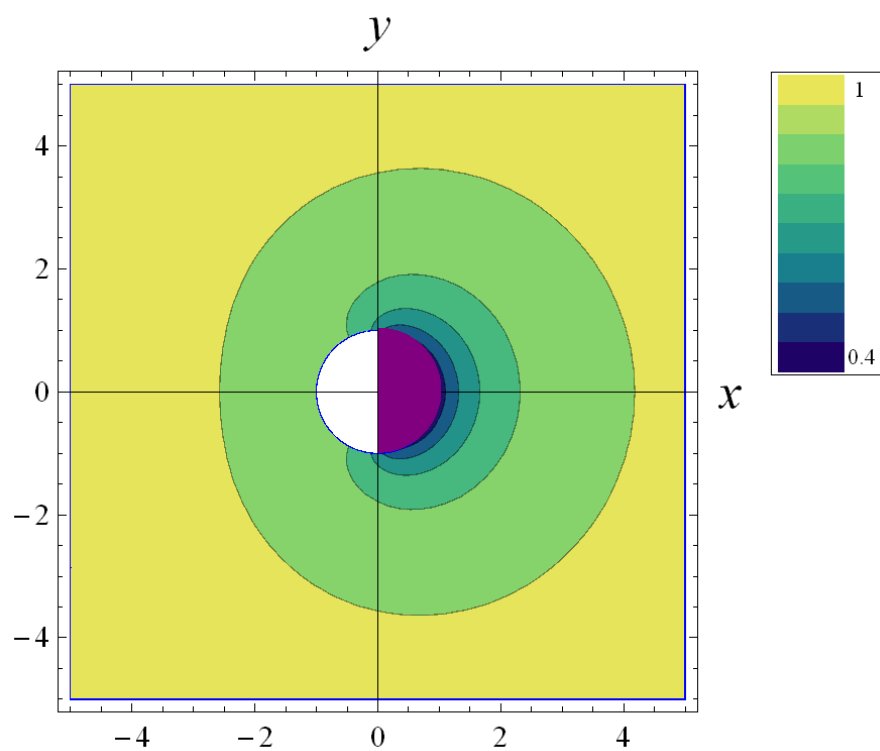


Figure 3.15: The contour plot for the concentration of hydrogen peroxide. One hemisphere of the Janus colloid coated with the catalyst is shown by purple, and color bar indicates high (yellow) versus low (dark blue) concentration. Due to the decomposition of substrate in the chemical reaction, there is a depletion of particles in the vicinity of the coated area.

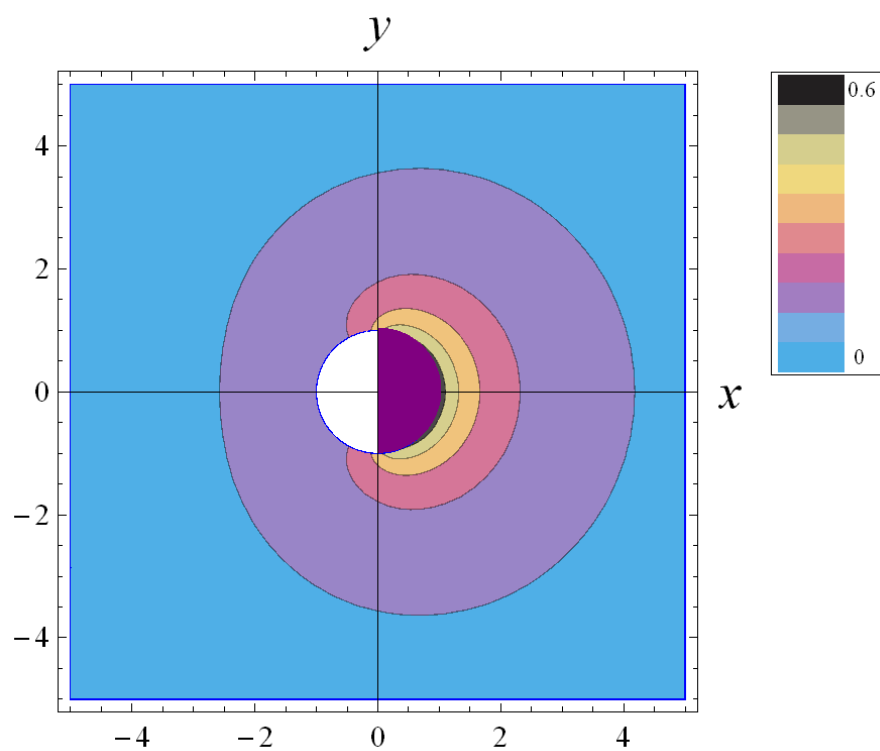


Figure 3.16: The contour plot for the product concentration, and discrete contour levels with high/low concentration are presented by colour bar. An accumulation of product molecules is created around the catalytic patch (purple) since more and more water and oxygen are generated from the reaction.

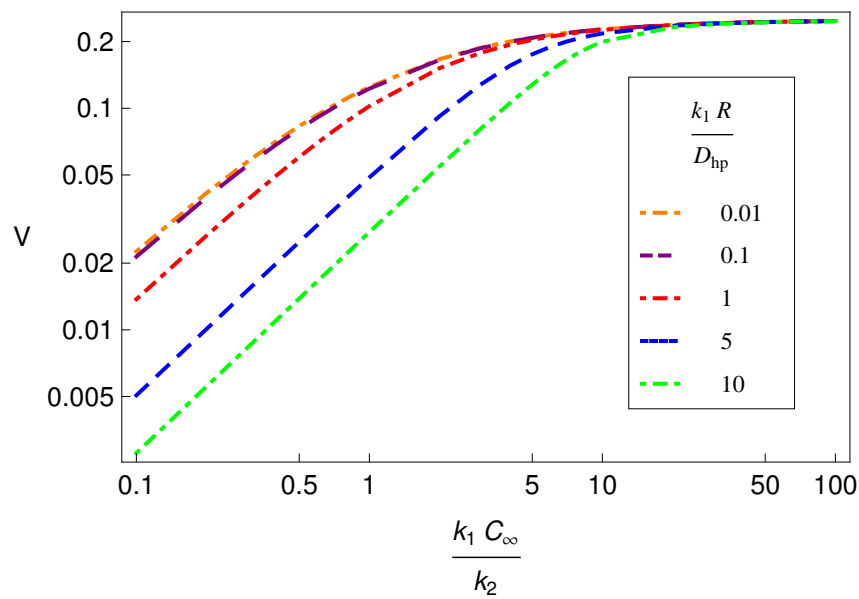


Figure 3.17: The velocity of the Janus sphere v.s. $\frac{k_1 C_\infty}{k_2}$ at constant values of $\frac{k_1 R}{D_{\text{hp}}}$ plotted on a logarithmic scale. Coloured lines indicate different size parameters $\frac{k_1 R}{D_{\text{hp}}}$ ranging from 0.01 to 10. As the propulsion velocity is proportional to the fuel concentration, the slope in this log-log plot is 1.

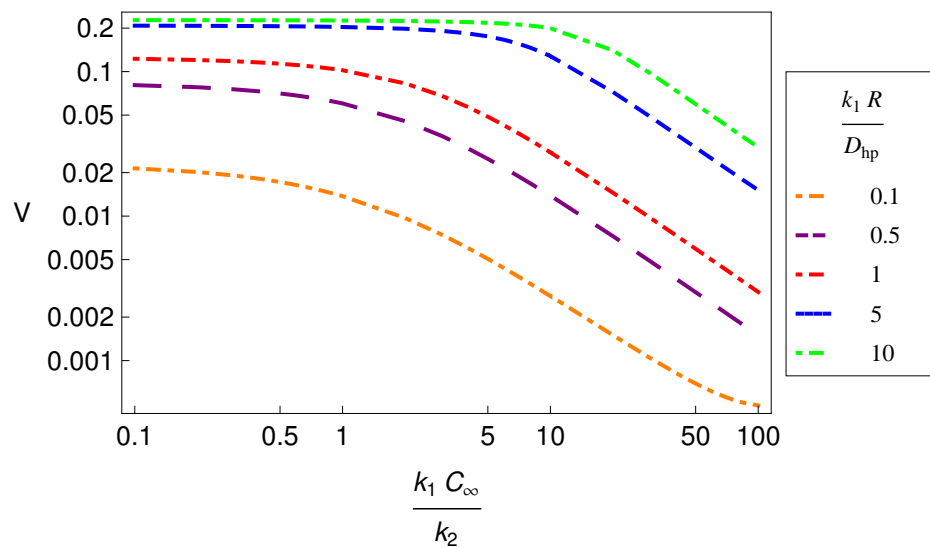


Figure 3.18: The velocity of the sphere v.s. $\frac{k_1 R}{D_{hp}}$ at constant values of $\frac{k_1 C_\infty}{k_2}$ are plotted on a logarithmic scale. Coloured lines show different fuel concentration $\frac{k_1 C_\infty}{k_2}$ ranging from 0.1 to 10. As the propulsion velocity decays with the swimmer size, the slope in the log-log plot is -1 .

– 3.18, and the results are illustrated on a logarithmic scale to highlight the turning points. According to the definition of variable $\frac{k_1 C_\infty}{k_2}$, the reaction rates k_1 and k_2 have the same dimensions, and consequently the relationship between $\frac{k_1 C_\infty}{k_2}$ and C_∞ is linear. As shown in Figure 3.17, the velocity is proportional to the concentration C_∞ while the fuel concentration is low ($\frac{k_1 C_\infty}{k_2} \ll 1$). As $\frac{k_1 C_\infty}{k_2}$ increases gradually, the velocity becomes independent of the fuel concentration.

Compared with Figure 3.17, there is a reversed pattern in Figure 3.18. In the small size limit $\frac{k_1 R}{D_{hp}} \ll 1$, the swimming velocity of the Janus sphere is independent of the size scale. By contrast, the propulsion velocity decreases and has a $1/R$ dependence in the realm $\frac{k_1 R}{D_{hp}} \gg 1$. In conclusion, the behaviour of the velocity is almost as predicted.

The propulsion velocity of Janus colloids that are half covered with a catalyst is experimentally probed [73]. In the experiment, various sizes of Janus spheres made of polystyrene beads were suspended in a hydrogen peroxide solution with 10% concentration. The size distribution ranged from 250 nm to 5 μ m and Janus colloids with different sizes were then tested, provided that other parameters, such as catalyst coating, thickness and fuel concentration were fixed. The experiment demonstrates that the velocity of the Janus particle decreases with its radius in the size range of the observation. The $1/R$ dependence is shown in Figure 3.19 [73], and the experimental data corresponds to the region III in Figure 3.8. In Figure 3.19, the parameters with a choice of $T = 293\text{ K}$, $\eta = 10^{-3}\text{ Pa}\cdot\text{s}$, $C_\infty = 3\text{ M}(10\%)$, and $\lambda_{eff} = 0.62\text{ \AA}$ fit reasonably well with the measured velocities in the size range of the observation [72] [73]. After appropriate scaling, the theoretical results are consistent with the experimental data, suggesting that a catalytic colloid propelled by diffusiophoresis can be a useful model to examine the swimming characteristics of colloidal dispersions.

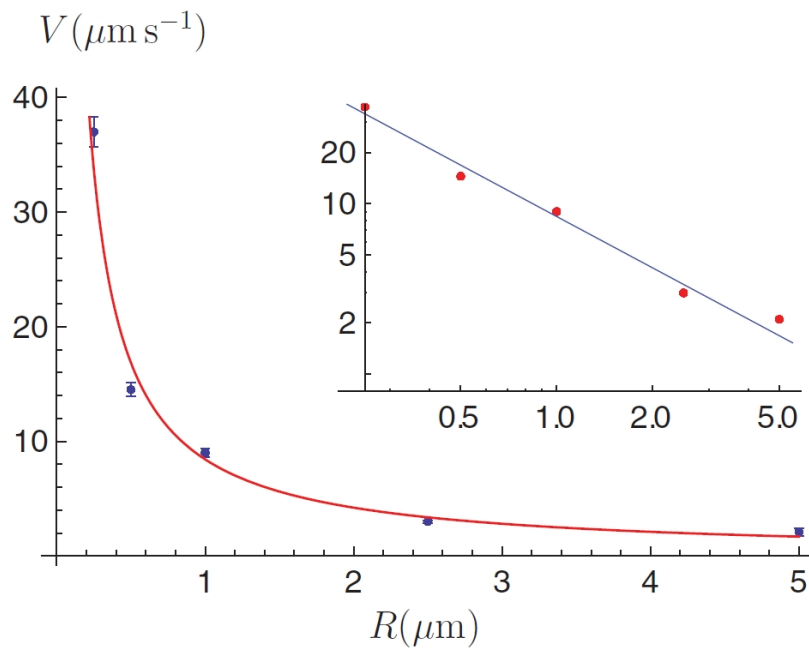


Figure 3.19: A comparison of the theoretical and experimental results for the swimming velocity of a Janus sphere as a function of its radius [73]. The numerical results for the theory are shown by a solid line, while dots indicate the experimental data. Inset: the same results in log-log form.

3.3.2 Inhomogeneous Sphere

For an inhomogeneous sphere, several different cases with various angular patterns of catalyst were studied. Although the coverage functions of these cases are different, the swimming velocities of such inhomogeneous spheres have the same behaviour. In the following, three different cases are shown as examples, and the corresponding coverage functions for these three cases are illustrated with respect to θ in Figures 3.5 – 3.7.

Similar to Janus sphere, the interaction and the asymmetric solute concentration in principle drive the motion for the inhomogeneous sphere to propel itself. By solving the set of nonlinear equations in Eq. (3.37), the full distribution of the concentration of hydrogen peroxide C_{hp} can be obtained as well. Figures 3.20 – 3.22 plot the solution of B_1 for cases 1–3, respectively, and B_1 is shown as a function of the colloid size. The results for these three different cases reveal the same trend of B_1 , which can be divided into two regions. While B_1 increases rapidly with the colloid size R in the region $\frac{k_1 R}{D_{\text{hp}}} < 50$, it suddenly decreases in the large size region $50 < \frac{k_1 R}{D_{\text{hp}}} < 1000$. The two regions of B_1 exhibit distinct dependence on the size of the sphere.

Next, the propulsion velocity can be determined from Eq. (3.42), and the results are illustrated in Figures 3.23 – 3.28. These figures have been sketched in the logarithmic scale for better visualisation. Figures 3.23 – 3.25 show a linear growth in velocity with increasing fuel concentration for small concentration $\frac{k_1 C_\infty}{k_2} < 1$, however, the propulsion velocity does not depend on fuel concentration in the region $10 < \frac{k_1 C_\infty}{k_2} < 100$. In general, velocity for both the Janus colloid and inhomogeneous covered spheres has the same dependence on fuel concentration. Additionally, the size dependence on velocity of the inhomogeneous sphere becomes increasing important as larger sized colloid, and

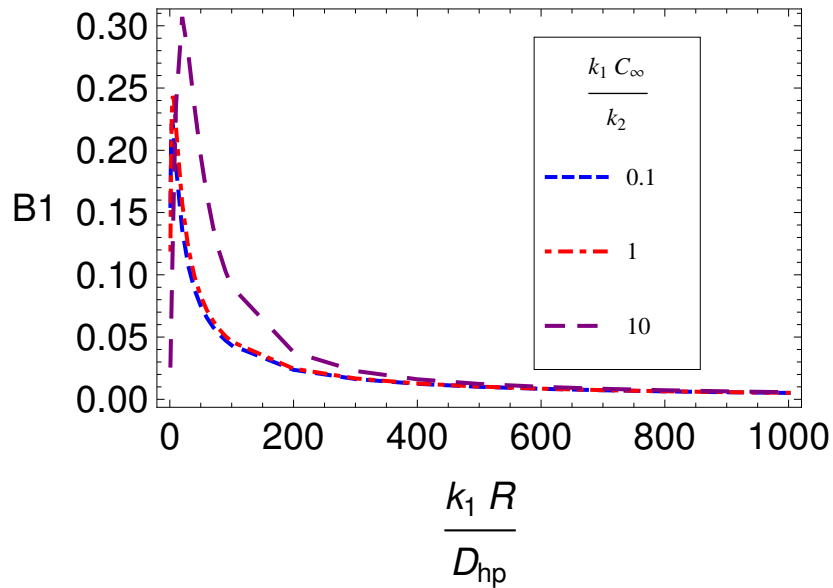


Figure 3.20: B_1 v.s. $\frac{k_1 R}{D_{hp}}$ at constant values of $\frac{k_1 C_\infty}{k_2}$ for inhomogeneous case 1.

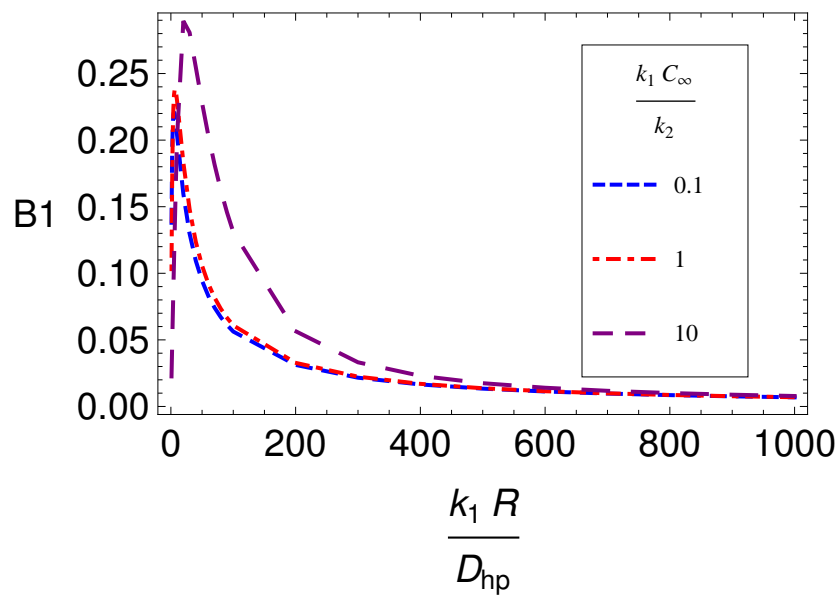


Figure 3.21: B_1 v.s. $\frac{k_1 R}{D_{hp}}$ at constant values of $\frac{k_1 C_\infty}{k_2}$ for inhomogeneous case 2

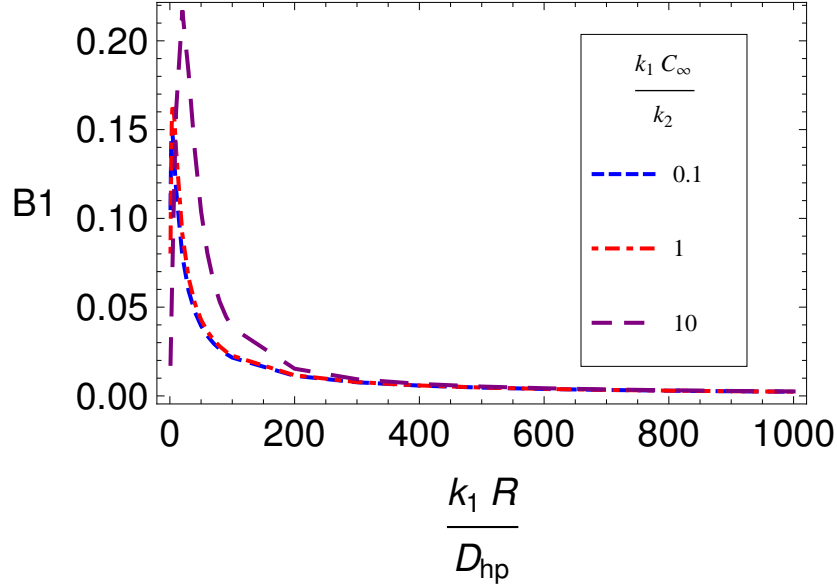


Figure 3.22: B_1 v.s. $\frac{k_1 R}{D_{hp}}$ at constant values of $\frac{k_1 C_\infty}{k_2}$ for inhomogeneous case 3

Figures 3.26 – 3.28 display this trend. When the spherical swimmer is sufficiently small ($\frac{k_1 R}{D_{hp}} < 100$), B_1 is proportional to its radius as shown in Figures 3.20 – 3.22. As a result, propulsion velocity is independent of the size scale at small size limit. On the contrary, the $1/R$ dependence occurs if the size of the spherical swimmer is in the realm $\frac{k_1 R}{D_{hp}} > 100$, where B_1 decreases with the size scale. The swimming velocity, consequently, decays with the size of the spherical swimmer and has a $1/R^2$ dependence. To sum up, the numerical results show that the behaviours of the velocity for inhomogeneous cases are almost as the theory has predicted in section 3.23.

When diffusiophoresis is expected to be the dominant propulsion mechanism, both Janus and inhomogeneous colloids can propel themselves in an aqueous solution, and such self-propulsion can be observed in all regions in Figures 3.8 – 3.9. The results display that the velocity of the asymmetrically catalysed particle is proportional to the fuel concentration in region I, whereas it decays with the radius of the sphere in region III. Although

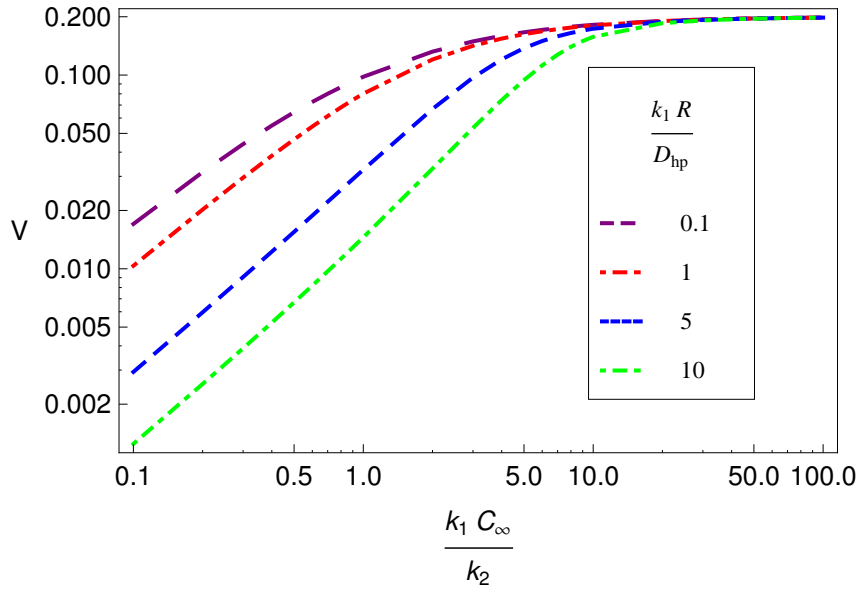


Figure 3.23: The propulsion velocity v.s. $\frac{k_1 C_\infty}{k_2}$ at constant values of $\frac{k_1 R}{D_{hp}}$ plotted in the logarithmic scale for inhomogeneous case 1; the slope for this log-log plot is 1.

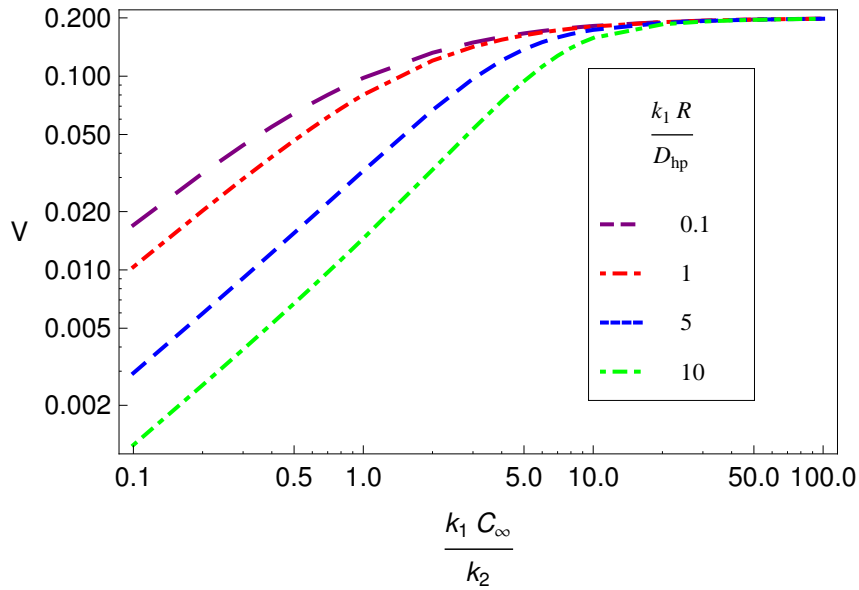


Figure 3.24: The propulsion velocity v.s. $\frac{k_1 C_\infty}{k_2}$ at constant values of $\frac{k_1 R}{D_{hp}}$ plotted in the logarithmic scale for inhomogeneous case 2; the slope for this log-log plot is 1.

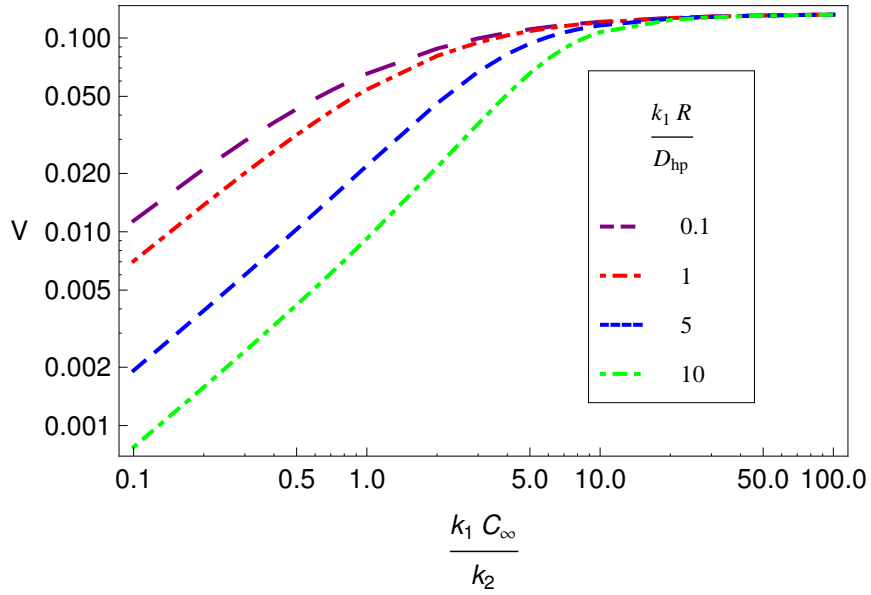


Figure 3.25: The propulsion velocity v.s. $\frac{k_1 C_\infty}{k_2}$ at constant values of $\frac{k_1 R}{D_{hp}}$ plotted in the logarithmic scale for inhomogeneous case 3; the slope for this log-log plot is 1.

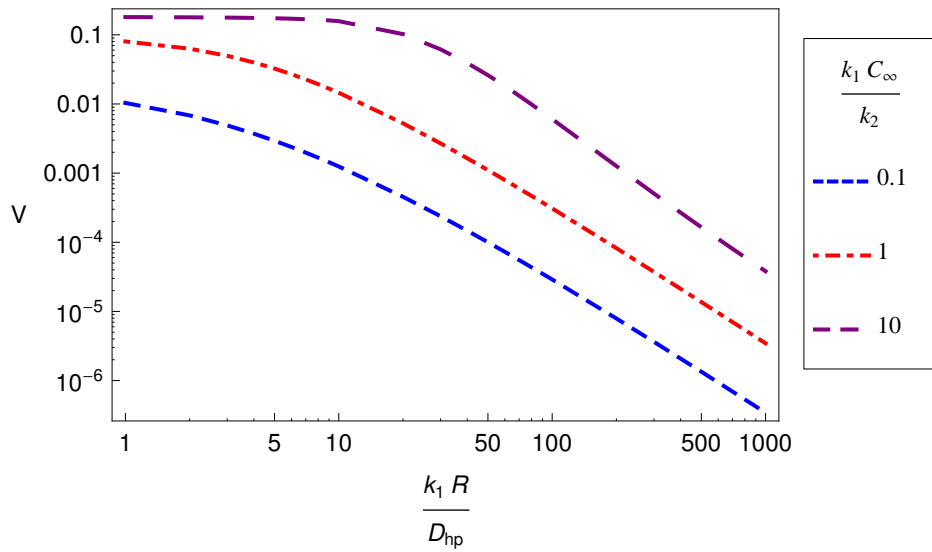


Figure 3.26: The propulsion velocity v.s. $\frac{k_1 R}{D_{hp}}$ at constant values of $\frac{k_1 C_\infty}{k_2}$ plotted in the logarithmic scale for inhomogeneous case 1; the slope for this log-log plot is -2.

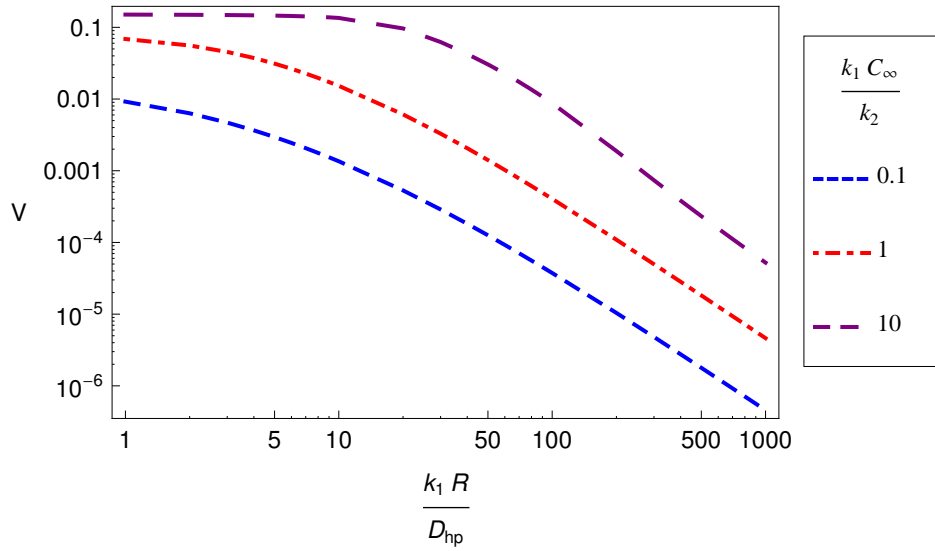


Figure 3.27: The propulsion velocity v.s. $\frac{k_1 R}{D_{hp}}$ at constant values of $\frac{k_1 C_\infty}{k_2}$ plotted in the logarithmic scale for inhomogeneous case 2; the slope for this log-log plot is -2 .

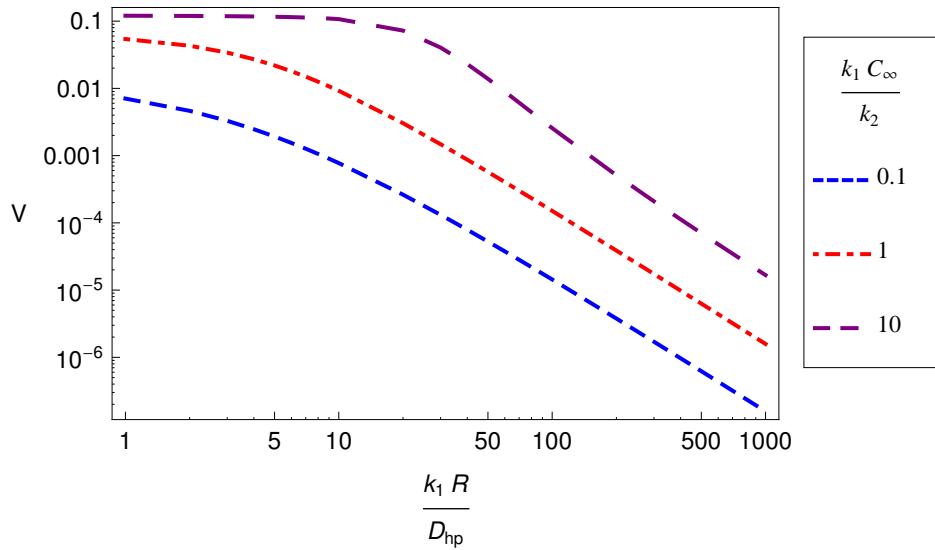


Figure 3.28: The propulsion velocity v.s. $\frac{k_1 R}{D_{hp}}$ at constant values of $\frac{k_1 C_\infty}{k_2}$ plotted in the logarithmic scale for inhomogeneous case 3; the slope for this log-log plot is -2 .

the swimming velocity for both Janus and inhomogeneous spheres is size independent in regimes I and II, it decays as a function of the colloid size at the larger size limit in regime III. The diagonal dot-dashed line in Figures 3.8 – 3.9 indicates that this crossover between regime II and III is not clear.

The fundamental difference in propulsion velocity for both Janus and inhomogeneous spheres is in the regime III in Figures 3.8 – 3.9, where velocity decrease considerably with the colloid size. The main difference between Janus and inhomogeneous spheres is in their different catalyst geometries. Why a Janus colloid swims faster than an inhomogeneous one can be understood physically. Propulsion of a Janus sphere powered by self-diffusiophoresis is due to solute gradient, which is sustained by a surface reaction occurring on only one side of the Janus colloid. However, catalyst is coated unevenly on both sides of an inhomogeneous sphere. Since there are products generated on two sides of an inhomogeneous colloid, this implies that the interactions of the solute species on the colloid become balanced, leading to small solute diffusion. In other words, it is easier for a Janus particle to maintain the asymmetric distribution of solute molecules and imbalanced concentration gradient, involving in solute diffusion. As a consequently, there is an enhanced diffusion of the Janus particle, and the velocity for Janus colloid decays slower with its size compared with an inhomogeneous one. From mathematical view, the velocity for inhomogeneous colloid has $1/R^2$ size dependence at a large size limit, and the decay length scale of the velocity reduction is computed as $\sqrt{D_{hp}/k_1}$ due to dimension analysis.

It was observed that the velocity of the Janus sphere decreases with the size scale [73]. This appears to contradict the expectation that the velocity of self-diffusiophoretic swimmers is independent of size, and is only controlled by the activity, which is a measure of the effective rate of activity for the catalytic reaction, the mobility, which is controlled

by the interaction of the solute molecules with the surface of the colloid, and the diffusion coefficient of the solute [82]. This is, however, only a statement about the contribution of size to the swimming velocity due to hydrodynamics. The key to resolving this apparent contradiction is to realise that the activity, which is taken as an effective rate of particle production per unit area, is in itself the result of a complex catalytic reaction-diffusion process and might depend on size.

It is important to note that there are experimental limitations on the practical range of size and fuel concentration. In fact, systematic probing the motion for smaller swimmers becomes more difficult because of the optical limit of the scattering techniques [73]. In addition, there will be an expulsion of oxygen bubbles as long as the local oxygen production from the chemical reaction with catalyst is considerably faster than solute diffusion from the surface of the colloid. This bubble release occurs especially for high fuel concentration or large colloids, and could also drive the propulsion of the particle [73] [89] [90]. With increasing fuel concentration or the size of swimmer, the self-diffusiophoresis is not the only explanation for the observed propulsion of the active colloid due to the presence of exceeding oxygen concentration and bubble ejection.

3.4 Summary

In conclusion, both Janus and inhomogeneous spheres can achieve autonomous propulsion powered by diffusiophoretic effect. The propulsion velocity of the Janus particle is inversely proportional to the radius of the sphere at the large size limit, however, the $1/R$ behaviour is expected to disappear for smaller sizes of swimmers. The numerical results for the velocity behaviour of the Janus colloid are in agreement with the experimental observation. This theoretical analysis for Janus sphere is then extended to an inhomoge-

neous case. Compared with Janus particles, while an inhomogeneous sphere has similar behaviour for propulsion velocity at small size limits, its propulsion velocity exhibits a decay with $1/R^2$ dependence at large size limits.

Chapter 4

Advection - Diffusion Model for Catalytic Janus Colloid

4.1 Introduction

At the heart of this chapter is the incorporation of advection into the diffusion equation, and the presentation of analytic and numerical methods to solve the resulting partial differential equation for a Janus colloid with an asymmetric chemical catalyst. Despite the Janus sphere being regarded as the simplest model, it is still a perfect starting point for the investigation of an autonomous motion powered by diffusiophoresis. However, even this simplest of model contains subtleties and complexities: what happens if advective transport and diffusive motion are considered together? How does the advection come into play? The work presented in the following sections attempts to offer a simple paradigm to explore the effects of advection on self-propulsion of colloidal particles. The quantitative procedures to examine the influence of advection-diffusion on velocity of a Janus sphere are provided as well.

4.2 Model of Advection-Diffusion for Phoretic Swimmers at Finite Péclet number

4.2.1 Advection-Diffusion Equation

Previous investigations of the phoretic motion of a self-propelled swimmer driven by concentration gradient only assumed that the scalar field evolves solely via diffusion [73] [79] [82] [91], and the effects of advection on such self-propelled colloids have been neglected. In this chapter, a theoretical framework is established for studying the effects of advection-diffusion on the diffusiophoretic motion of colloidal particles and examines the general case with finite Péclet number. The relative importance between advection and diffusion can be measured by a dimensionless Péclet number Pe .

$$Pe = \frac{va}{D} \quad (4.1)$$

Here, v is the flow speed, a denotes a characteristic length scale of the colloid, and D refers to the diffusion coefficient of the solute. A typical, open ocean is characterised by velocities of order 0.01 m/s , lengths of order $2 - 3000 \text{ km}$ (the size of large rotating ocean currents), and the turbulent diffusion coefficient of order $1000 \text{ m}^2/\text{s}$, therefore Pe is of order $20 - 30$. For the theoretical model for diffusion-reaction described in Chapter 3, the advection is neglected relative to diffusion as Pe is less than 10^{-2} with magnitude of propulsion velocity $V < 10 \text{ } \mu\text{m/s}$, colloid size $R \sim \mu\text{m}$, and diffusion coefficient $D \sim 10^{-9} \text{ m}^2/\text{s}$.

In this scheme, a Janus particle with radius R is considered. Taking the incompressible flow assumption into account, the Stokes equations will read

$$\nabla p = \eta \nabla^2 \mathbf{v}, \quad (4.2)$$

$$\nabla \cdot \mathbf{v} = 0. \quad (4.3)$$

Here p is the pressure, η denotes the (constant) dynamic viscosity, and \mathbf{v} represents the velocity of the fluid. For a solute, the concentration field c can be approximated by the solution of the Stokes equations:

$$\mathbf{v} \cdot \nabla c - D \nabla^2 c = 0. \quad (4.4)$$

Boundary condition for the concentration field is set out by

$$-D \partial_r c|_{r=R} = \alpha(\theta), \quad (4.5)$$

where α is the surface activity, and θ denotes the polar angle. The concentration profile is then expanded in terms of Legendre polynomials $P_l(\cos \theta)$ with unknown coefficient c_l .

$$c(r, \theta) = \sum_{l=0}^{\infty} c_l(r) P_l(\cos \theta) \quad (4.6)$$

The interest here is in the spherical coordinates (r, θ, φ) . Here, r is radial distance, θ indicates the polar angle, and φ denotes the azimuthal angle. Note that the theoretical model is specialised in azimuthally symmetric problems (i.e. problems with no azimuthal dependence). In other words, this approach infers $\frac{\partial c}{\partial \varphi} = 0$, and in this case Laplacian and gradient operators can be simplified in this way:

$$\nabla^2 c = \frac{\partial^2 c}{\partial r^2} + \frac{2}{r} \frac{\partial c}{\partial r} + \frac{1}{r^2} \frac{\partial^2 c}{\partial \theta^2} + \frac{\cot \theta}{r^2} \frac{\partial c}{\partial \theta}, \quad (4.7)$$

$$\nabla c = \frac{\partial c}{\partial r} \hat{r} + \frac{1}{r} \frac{\partial c}{\partial \theta} \hat{\theta}. \quad (4.8)$$

Then the advection-diffusion equation Eq. (4.4) becomes:

$$\begin{aligned} & \mathbf{v} \cdot \nabla c - D \nabla^2 c \\ &= v_r \frac{\partial c}{\partial r} + \frac{1}{r} v_\theta \frac{\partial c}{\partial \theta} - D \left(\frac{\partial^2 c}{\partial r^2} + \frac{2}{r} \frac{\partial c}{\partial r} - \frac{l(l+1)c}{r^2} \right) \\ &= \sum_{l=0}^{\infty} v_r \frac{\partial c_l}{\partial r} P_l(\cos \theta) + \sum_{l=0}^{\infty} \frac{v_\theta c_l}{r} \frac{\partial P_l}{\partial \theta} - \sum_{l=0}^{\infty} D \left(\frac{\partial^2 c_l}{\partial r^2} + \frac{2}{r} \frac{\partial c_l}{\partial r} - \frac{l(l+1)c_l}{r^2} \right) P_l(\cos \theta). \end{aligned} \quad (4.9)$$

4.2.2 Velocity Distribution

To begin with, fluid flow is set up due to an interaction between the colloid and solute within a thin boundary layer, and a slip velocity at the edge of this layer is proportional to the local concentration gradient determined by a combination of diffusion and advection.

$$\mathbf{v}_s(r_s) = \mu_s(r_s)(\mathbf{I} - \mathbf{nn}) \cdot \nabla c_s(r_s) \quad (4.10)$$

For the spherical case, the pressure is represented as the summation of Legendre polynomials.

$$\nabla^2 p = 0 \implies p(r, \theta) = \sum_{l=0}^{\infty} A_l \left(\frac{R}{r}\right)^{l+1} P_l(\cos \theta) \quad (4.11)$$

By introducing the Laplacian ∇^2 , the expression for $\nabla^2(r \cdot v)$ is

$$\nabla^2(r \cdot \mathbf{v}) = r \cdot \nabla^2 \mathbf{v} + 2\nabla \cdot \mathbf{v}. \quad (4.12)$$

As the flow is not compressible, providing that the fluid density does not vary in response to a change in pressure, hence the curl of a gradient field is zero ($\nabla \cdot \mathbf{v} = 0$), and the above equation leads to the following

$$\begin{aligned} \nabla^2(rv_r(r, \theta))r &= r \cdot \nabla^2 \mathbf{v} = \frac{r}{\eta} \nabla p \\ &= -\frac{1}{\eta} \sum_{l=0}^{\infty} A_l(l+1) \left(\frac{R}{r}\right)^{l+1} P_l(\cos \theta). \end{aligned} \quad (4.13)$$

This help us to write $r \cdot \mathbf{v}$ in the form of

$$rv_r(r, \theta) = \frac{1}{\eta} \sum_{l=0}^{\infty} f_l P_l(\cos \theta), \quad (4.14)$$

where f_l is unknown. By applying Eq. (4.14) to Eq. (4.13), the following formula can be obtained

$$\frac{1}{r} \frac{\partial^2}{\partial r^2}(rf_l(r)) - \frac{l(l+1)}{r^2} f_l(r) = -P_l(l+1) \left(\frac{R}{r}\right)^{l+1}. \quad (4.15)$$

One of the most powerful methods of solving differential equations is "Guess-and-Check".

Now, an attempt is made to guess a particular solution for the unknown function f_l .

$$f_l(r) = X_l r^l + \frac{Y_l}{r^{l+1}} + \frac{1}{2} \frac{l+1}{2l-1} Z_l R^2 \left(\frac{R}{r}\right)^{l-1} \quad (4.16)$$

Note that X_l , Y_l , and Z_l correspond to different r dependences and these three unknown functions will need to be solved later.

Firstly, X_l can be determined by considering some extreme conditions. As $r \rightarrow \infty$ and $v_r < \infty$, this results in $X_l = 0$ for $l \geq 2$. Furthermore, if the velocity is integrated over the surface of a large sphere, the zeroth order of X_l , Y_l , Z_l are all zeros.

$$0 = \oint \mathbf{v} \cdot d\mathbf{s} = r \frac{f_0(r)}{\eta} = \frac{1}{\eta} \left(X_0 r + Y_0 - \frac{1}{2} Z_0 R r^2 \right) \quad (4.17)$$

$$\implies X_0 = 0, \quad Y_0 = 0, \quad Z_0 = 0 \quad (4.18)$$

For another special case where $r \rightarrow \infty$, X_1 is found to have a simple form.

$$\begin{aligned} v_r(r, \theta)|_{r \rightarrow \infty} &= \frac{1}{r\eta} \left(X_1 r + \frac{Y_1}{r^2} + Z_1 R^2 \right) P_1(\cos\theta) \\ &= \frac{X_1}{\eta} \cos\theta = -|\mathbf{v}| \cos\theta \\ \implies X_1 &= -|\mathbf{v}| \eta \end{aligned} \quad (4.19)$$

Here, $|\mathbf{v}|$ is the magnitude of the fluid velocity. After solving X_l , the velocity profile can be rewritten as

$$\begin{aligned} v_r(r, \theta) &= \frac{1}{r\eta} \sum_{l=0}^{\infty} f_l P_l(\cos\theta) \\ &= -|\mathbf{v}| \cos\theta + \frac{1}{r\eta} \sum_{l=1}^{\infty} \left[\frac{Y_l}{r^{l+1}} + \frac{1}{2} \frac{l+1}{2l-1} Z_l R^2 \left(\frac{R}{r} \right)^{l-1} \right] P_l(\cos\theta) \\ &= -|\mathbf{v}| \cos\theta + \frac{1}{\eta} \sum_{l=1}^{\infty} \left[\frac{Y_l}{r^{l+2}} + \frac{1}{2} \frac{l+1}{2l-1} Z_l R \left(\frac{R}{r} \right)^l \right] P_l(\cos\theta). \end{aligned} \quad (4.20)$$

The next step is to consider the boundary condition in order to solve Y_l . At the surface, the velocity should be zero $v_r(R, \theta) = 0$.

For $l = 1$

$$\begin{aligned} -|\mathbf{v}| + \frac{1}{\eta} \left(\frac{Y_1}{R^3} + Z_1 R \right) &= 0 \\ \implies Y_1 &= (\eta|\mathbf{v}| - Z_1 R) R^3 \end{aligned} \quad (4.21)$$

For $l \geq 2$

$$\begin{aligned} \frac{Y_l}{R^{l+2}} + \frac{1}{2} \frac{l+1}{2l-1} Z_l R &= 0 \\ \implies Y_l &= -\frac{1}{2} \frac{l+1}{2l-1} Z_l R^{l+3} \end{aligned} \quad (4.22)$$

Substituting the solutions of X_l and Y_l , the velocity distribution is reduced to only one unknown coefficient Z_l .

$$v_r(r, \theta) = -|\mathbf{v}| \cos \left[1 - \left(\frac{R}{r} \right)^3 \right] + \frac{R}{2\eta} \sum_{l=1}^{\infty} Z_l \frac{l+1}{2l-1} \left[\left(\frac{R}{r} \right)^l - \left(\frac{R}{r} \right)^{l+2} \right] P_l(\cos \theta) \quad (4.23)$$

Next, a trick of a stream function is applied to solve the unknown function Z_l .

If the flow is incompressible and irrotational, velocity can be expressed as a function of a scalar potential $\mathbf{v} = f(\psi)$, where ψ is known as the stream function because it is constant along a streamline. The potential ψ is not only the scalar field which a vector field can be expressed in terms of. Velocity can be expressed in terms of a stream function as well.

$$\begin{aligned} \nabla \times \mathbf{v} = 0 &\implies \mathbf{v} = \nabla \psi \\ \nabla \cdot \mathbf{v} = 0 &\implies \nabla^2 \psi = 0 \end{aligned} \quad (4.24)$$

Considering a two-dimensional flow $\mathbf{v} = (v_x, v_y, 0)$, the stream function ψ is defined to satisfy the continuity equation, which is in fact a statement of the conservation of mass. In spherical coordinates, the velocity components for such a flow are related to the stream function ψ by

$$v_r = -\frac{1}{r^2 \sin \theta} \frac{\partial \psi}{\partial \theta}, \quad v_\theta = \frac{1}{r \sin \theta} \frac{\partial \psi}{\partial r}. \quad (4.25)$$

By using new function v_l , Eq. (4.23) can be rewritten as

$$v_r = \sum_{l=1}^{\infty} v_l(r) P_l(\cos \theta) = \frac{1}{r^2} \frac{\partial \psi}{\partial x}, \quad x = \cos \theta. \quad (4.26)$$

Note that concentration profile is expanded in terms of Legendre polynomials in Eq. (4.6). The Legendre polynomials are satisfied with Legendre's differential equation, and $P_l(x)$ can be expressed by using Rodrigues' formula, manipulating the l th power series in a class of special functions in terms of the l th derivatives of the Legendre polynomials.

$$\frac{d}{dx} \left[(1-x^2) \frac{dP_l(x)}{dx} \right] = -l(l+1)P_l(x), \quad (4.27)$$

$$P_l(x) = \frac{1}{2^l l!} \frac{d^l}{dx^l} \left[(x^2-1)^l \right] \quad (4.28)$$

By applying the recurrence relation known as Bonnet's recursion formula

$$P_l(x) = \frac{1}{2l+1} \frac{d}{dx} [P_{l+1}(x) - P_{l-1}(x)], \quad (4.29)$$

this compact representation of Legendre polynomial can help us to obtain the profile of the stream function ψ .

$$\begin{aligned} \frac{\partial \psi}{\partial x} &= -\sin \theta \frac{\partial \psi}{\partial \theta} = \sum_{l=1}^{\infty} r^2 v_l(r) P_l(x) \\ &= \sum_{l=1}^{\infty} \frac{r^2 v_l(r)}{2l+1} \frac{d}{dx} [P_{l+1}(x) - P_{l-1}(x)], \end{aligned} \quad (4.30)$$

$$\psi = \sum_{l=1}^{\infty} \frac{r^2 v_l(r)}{2l+1} [P_{l+1}(x) - P_{l-1}(x)] \quad (4.31)$$

The v_θ can be formulated as follows

$$\begin{aligned} v_\theta &= \frac{1}{r \sin \theta} \sum_{l=1}^{\infty} \frac{1}{2l+1} \left(2r v_l(r) + r^2 \frac{d v_l}{d r} \right) [P_{l+1}(x) - P_{l-1}(x)] \\ &= |\mathbf{v}| \sin \theta \left[1 + \frac{1}{2} \left(\frac{R}{r} \right)^3 \right] + \frac{R}{2\eta \sin \theta} \sum_{l=1}^{\infty} \frac{Z_l(l+1)}{(2l+1)(2l-1)} \left[(2-l) \left(\frac{R}{r} \right)^l + l \left(\frac{R}{r} \right)^{l+2} \right] \\ &\quad [P_{l+1}(\cos \theta) - P_{l-1}(\cos \theta)] \end{aligned} \quad (4.32)$$

The Z_l is still unknown, and the slip boundary condition and properties of Legendre polynomials are considered to solve it. Slip boundary condition is a function of mobility

μ and solute concentration c .

$$\begin{aligned}
 v_\theta(R, \theta) &= \frac{\mu}{R} \partial_\theta c(R, \theta) \\
 &= \frac{\mu}{R} \frac{\partial}{\partial \theta} \sum_{l=0}^{\infty} c_l(R) P_l(\cos \theta) \\
 &= -\frac{\mu}{R} \sin \theta \sum_{l=0}^{\infty} \frac{d}{dx} c_l(R) P_l(\cos \theta)
 \end{aligned} \tag{4.33}$$

On the surface, v_θ in Eq. (4.32) has this form:

$$v_\theta(r = R, \theta) = \frac{3}{2} |\mathbf{v}| \sin \theta + \frac{R}{\eta \sin \theta} \sum_{l=1}^{\infty} \frac{Z_l(l+1)}{(2l+1)(2l-1)} [P_{l+1}(x) - P_{l-1}(x)]. \tag{4.34}$$

Note that Eqs. (4.33) – (4.34) are two forms of v_θ and both need to be the same. Multiplying the right hand sides of Eqs. (4.33) – (4.34) by $\sin \theta$, the v_θ can be carried out.

$$\frac{\mu}{R} (x^2 - 1) \frac{d}{dx} \sum_{l=1}^{\infty} c_l(R) P_l(x) = \frac{3}{2} |\mathbf{v}| (1 - x^2) + \frac{R}{\eta} \sum_{l=1}^{\infty} \frac{Z_l(l+1)}{(2l+1)(2l-1)} [P_{l+1}(x) - P_{l-1}(x)] \tag{4.35}$$

Differentiating both sides of Eq. (4.35) leads to the following relation.

$$\begin{aligned}
 &\frac{\mu}{R} \frac{d}{dx} \left[(x^2 - 1) \frac{d}{dx} \sum_{l=1}^{\infty} c_l(R) P_l(x) \right] \\
 &= \frac{3}{2} |\mathbf{v}| \frac{d}{dx} (1 - x^2) + \frac{R}{\eta} \sum_{l=1}^{\infty} Z_l \frac{l+1}{2l-1} \frac{d}{dx} \left[\frac{P_{l+1}(x)}{2l+1} - \frac{P_{l-1}(x)}{2l+1} \right]
 \end{aligned} \tag{4.36}$$

Bonnet's recursion formula is then applied and Eq. (4.36) can be reduced to

$$\frac{\mu}{R} \sum_{l=1}^{\infty} c_l(R) l(l+1) P_l(x) = -3|\mathbf{v}|x + \frac{R}{\eta} \sum_{l=1}^{\infty} Z_l \frac{l+1}{2l-1} P_l(x). \tag{4.37}$$

Finally, the different order of the desired function Z_l can be expressed in the following way, and Z_l has a straightforward relation to the concentration.

$$l = 1, \quad Z_1 = \frac{\mu\eta}{R^2} c_1 + \frac{3\eta|\mathbf{v}|}{2R} \tag{4.38}$$

$$l \geq 2, \quad Z_l = \frac{\mu\eta}{R^2} l(2l-1) c_l \tag{4.39}$$

Next, Z_1 is solved by using a stress tensor σ which is derived from the Appendix. A detailed exposition of all the components of the stress tensor is also provided.

In the Appendix, it shows that σ_{rr} and $\sigma_{r\theta}$ are the function of pressure, velocity, and viscosity. For force free motion, it implies that Z_1 must be zero,

$$F_T = \oint ds(\sigma_{rr} \cos \theta - \sigma_{r\theta} \sin \theta) = 0, \quad (4.40)$$

$$\implies Z_1 = 0 \quad (4.41)$$

and this relates the velocity v and concentration c

$$|\mathbf{v}| = -\frac{2}{3} \frac{\mu}{R} c_1(R, \theta). \quad (4.42)$$

There is now an explicit form for the velocity distribution:

$$v_r(r, \theta) = -|\mathbf{v}| \left[1 - \left(\frac{R}{r} \right)^3 \right] \cos \theta + \frac{\mu}{2R} \sum_{l=2}^{\infty} l(l+1) c_l \left[\left(\frac{R}{r} \right)^l - \left(\frac{R}{r} \right)^{l+2} \right] P_l(\cos \theta), \quad (4.43)$$

$$v_\theta(r, \theta) = |\mathbf{v}| \left[1 + \frac{1}{2} \left(\frac{R}{r} \right)^3 \right] \sin \theta + \frac{\mu}{2R \sin \theta} \sum_{l=2}^{\infty} c_l \frac{l(l+1)}{2l+1} \left[(2-l) \left(\frac{R}{r} \right)^l + l \left(\frac{R}{r} \right)^{l+2} \right] [P_{l+1}(\cos \theta) - P_{l-1}(\cos \theta)]. \quad (4.44)$$

Combining the preceding equations, the resulting formula shows that the the advection-diffusion equation in Eq. (4.9) is very complex and nonlinear. How to deal with this nonlinearity? The first trick is to eliminate it – with scaling and a change of variables. After an appropriate scaling, it is convenient to use the new scaled variables $\zeta, C, \mathbf{V}, \text{Pe}, K$

and set

$$\varsigma = \frac{r}{R}, \quad (4.45)$$

$$c(r, \theta) = \frac{\alpha R}{D} C(\varsigma, \theta), \quad (4.46)$$

$$\mathbf{v}(r, \theta) = \frac{\alpha \mu}{D} \mathbf{V}(\varsigma, \theta), \quad (4.47)$$

$$\text{Pe} = \frac{\alpha \mu R}{D^2}, \quad (4.48)$$

$$\alpha = \alpha K(\theta). \quad (4.49)$$

The advection-diffusion equation and its boundary condition in Eqs. (4.4 – (4.5) can then be expressed as

$$\text{Pe} \mathbf{V} \cdot \nabla C - \nabla^2 C = 0, \quad (4.50)$$

$$-\partial_\varsigma C|_{\varsigma=1} = K(\theta). \quad (4.51)$$

It is useful to define a new variable t , which is the ratio between radius of the sphere and distance; t is dimensionless and ranges between 0 and 1.

$$t = \frac{R}{r} = \frac{1}{\varsigma}$$

$$R < r < \infty \implies 1 > t > 0 \quad (4.52)$$

Although the advection-diffusion equation is modified, the technique combined with the scaling and changing of variables does not make it linear. Here are the details – for both the first and second derivatives:

$$\frac{\partial}{\partial \varsigma} = -t^2 \frac{\partial}{\partial t}, \quad (4.53)$$

$$\frac{\partial^2}{\partial \varsigma^2} = \frac{\partial}{\partial \varsigma} \left(\frac{\partial}{\partial \varsigma} \right) = -t^2 \frac{\partial}{\partial t} \left(-t^2 \frac{\partial}{\partial t} \right) = 2t^3 \frac{\partial}{\partial t} + t^4 \frac{\partial^2}{\partial t^2}. \quad (4.54)$$

The new scaled concentration is written as

$$C(t, \theta) = \sum_{l=0}^{\infty} C_l(t) P_l(\cos \theta), \quad (4.55)$$

and the unknown coefficients C_l need to be solved.

Using the scaling and changing r completely to the new variable t , the velocity distributions in Eqs. (4.43) – (4.44) are now modified as follows.

$$V_t(t, \theta) = \frac{2}{3}C_1 \cos \theta(1 - t^3) + \frac{1}{2} \sum_{m=2}^{\infty} C_m m(m+1) (t^m - t^{m+2}) P_m(\cos \theta) \quad (4.56)$$

$$V_\theta(t, \theta) = -\frac{2}{3}C_1 \sin \theta \left(1 + \frac{t^3}{2}\right) + \frac{1}{2 \sin \theta} \sum_{m=2}^{\infty} C_m \frac{m(m+1)}{2m+1} [(2-m)t^m + mt^{m+2}] (P_{m+1} - P_{m-1}) \quad (4.57)$$

Rewriting the advection-diffusion equation Eq. (4.50) in terms of the new variable t ,

$$\begin{aligned} & \text{Pe} \sum_l^\infty V_\varsigma \frac{\partial C_\varsigma}{\partial \varsigma} P_l + \text{Pe} \sum_l^\infty \frac{V_\theta C_\varsigma}{\varsigma} \frac{\partial P_l}{\partial \theta} - \sum_l^\infty \left(\frac{\partial^2 C_\varsigma}{\partial \varsigma^2} + \frac{2}{\varsigma} \frac{\partial C_\varsigma}{\partial \varsigma} - \frac{l(l+1)}{\varsigma^2} C_\varsigma \right) P_l = 0 \\ \implies & -\text{Pe} \sum_l^\infty V_t t^2 \frac{\partial C_l}{\partial t} P_l + \text{Pe} \sum_l^\infty V_t C_l t \frac{\partial P_l}{\partial \theta} - \sum_l^\infty \left(t^4 \frac{\partial^2 C_l}{\partial t^2} - l(l+1)t^2 C_l \right) P_l = 0 \\ \implies & -\text{Pe} \sum_l^\infty V_t t \frac{\partial C_l}{\partial t} P_l + \text{Pe} \sum_l^\infty V_t C_l \frac{\partial P_l}{\partial \theta} - \sum_l^\infty \left(t^3 \frac{\partial^2 C_l}{\partial t^2} - l(l+1)t C_l \right) P_l = 0. \end{aligned} \quad (4.58)$$

Now the prime for differentiation with respect to t is rewritten, and note that at this point Pe is still arbitrary.

An important property of the Legendre polynomials is that they are orthogonal. Looking at the Legendre polynomials in the advection-diffusion equation Eq. (4.58) to see how this can all be reduced into one summation in the following form:

$$\begin{aligned} & \sum_{l=0}^{\infty} J_l(t) P_l(\cos \theta) = 0, \\ \implies & J_l(t) = 0 \end{aligned} \quad (4.59)$$

where, $J_l(t) = J_l(C_l(t), C_m(t), C_n(t), \text{Pe})$. Due to the orthogonal property, this summation can only be satisfied if all polynomial terms will have their coefficients $J_l(t)$ equal

to zero. Next, it is necessary to express every term in Eq. (4.58) in terms of Legendre polynomials and this leads to the next topic.

By applying the Legendre polynomial triple product integrals $G_{l,m,n}$ and $H_{l,m,n}$, the advection-diffusion equation Eq. (4.58) can be simplified term by term.

$$G_{l,m,n} = \int_{-1}^1 P_l(x)P_m(x)P_n(x)dx \quad (4.60)$$

$$P_l P_m = \sum_{n=0}^{l+m} \frac{2n+1}{2} G_{l,m,n} P_n(\cos \theta) \quad (4.61)$$

$$H_{l,m,n} = \int_{-1}^1 \frac{\partial P_l}{\partial x} P_m(x)P_n(x)dx \quad (4.62)$$

$$\frac{\partial P_l}{\partial x} P_m = \sum_{n=0}^{l+m} \frac{2n+1}{2} H_{l,m,n} P_n(\cos \theta) \quad (4.63)$$

Ideally, the value of the upper limit in all summations should be infinity ∞ . In order to simplify the problem, a symbolic upper limit N is used instead of infinity. The first term in Eq. (4.58) is then separated into two terms $t1$ and $t2$:

$$- \text{Pe} \sum_l^N V_l t \frac{\partial C_l}{\partial t} P_l = t1 + t2 \quad (4.64)$$

$$\begin{aligned} t1 &= -\text{Pe} \sum_{l=0}^N \frac{2}{3} (t - t^4) C_1 \frac{\partial C_l}{\partial t} \cos \theta P_l = -\text{Pe} \sum_{l=0}^N \frac{2}{3} (t - t^4) C_1 \frac{\partial C_l}{\partial t} \sum_{n=0}^{N+1} \frac{2n+1}{2} G_{l,1,n} P_n \\ &= -\text{Pe} \sum_{l=0}^{N+1} \frac{2l+1}{2} P_l \sum_{n=0}^N \frac{2}{3} (t - t^4) C_1 \frac{\partial C_n}{\partial t} G_{n,1,l} \end{aligned} \quad (4.65)$$

and

$$\begin{aligned} t2 &= -\frac{\text{Pe}}{2} \sum_{l=0}^N t \frac{\partial C_l}{\partial t} P_l \sum_{m=2}^N C_m m(m+1) (t^m - t^{m+2}) P_m \\ &= -\frac{\text{Pe}}{2} \sum_{l=0}^N \sum_{m=2}^N \frac{\partial C_l}{\partial t} C_m m(m+1) (t^{m+1} - t^{m+3}) \sum_{l=0}^{2N} \frac{2n+1}{2} G_{l,m,n} P_n \\ &\quad - \frac{\text{Pe}}{2} \sum_{l=0}^{2N} \frac{2l+1}{2} P_l \sum_{m=2}^N \frac{\partial C_l}{\partial t} C_m m(m+1) (t^{m+1} - t^{m+3}) \sum_{n=0}^N G_{n,m,l} \end{aligned} \quad (4.66)$$

Now consider the recursive formula for the Legendre polynomials:

$$\begin{aligned}
 x &= \cos \theta \\
 \frac{\partial}{\partial x} \left[(1-x^2) \frac{\partial P_l}{\partial x} \right] &= -l(l+1)P_l = -\frac{l(l+1)}{2l+1} \frac{\partial}{\partial x} (P_{l+1} - P_{l-1}) \\
 \implies \frac{\partial P_l}{\partial \theta} &= -\sin \theta \frac{\partial P_l}{\partial x} = \frac{1}{\sin \theta} \frac{l(l+1)}{2l+1} (P_{l+1} - P_{l-1})
 \end{aligned} \tag{4.67}$$

Similarly, by applying the above rule, the second term in Eq. (4.58) can also be separated into two terms $t3$ and $t4$:

$$\text{Pe} \sum_l V_l C_l \frac{\partial P_l}{\partial \theta} = t3 + t4 \tag{4.68}$$

$$\begin{aligned}
 t3 &= \text{Pe} \sum_{l=0}^N \frac{2}{3} \left(1 + \frac{t^3}{2}\right) C_1 C_l \sin^2 \theta \frac{\partial P_l}{\partial x} \\
 &= -\text{Pe} \sum_{l=0}^N \frac{2}{3} \left(1 + \frac{t^3}{2}\right) C_1 C_l \frac{l(l+1)}{2l+1} (P_{l+1} - P_{l-1}) \\
 &= -\text{Pe} \sum_{l=0}^{N+1} \frac{2l+1}{2} P_l \sum_{n=0}^N \frac{2}{3} \left(1 + \frac{t^3}{2}\right) C_1 C_n \frac{n(n+1)}{2n+1} G_{n+1,0,l} \\
 &\quad + \text{Pe} \sum_{l=0}^{N-1} \frac{2l+1}{2} P_l \sum_{n=0}^N \frac{2}{3} \left(1 + \frac{t^3}{2}\right) C_1 C_n \frac{n(n+1)}{2n+1} G_{n-1,0,l}
 \end{aligned} \tag{4.69}$$

and

$$\begin{aligned}
 t4 &= \frac{\text{Pe}}{2 \sin \theta} \sum_{l=0}^N C_l \frac{\partial P_l}{\partial \theta} \sum_{m=2}^N C_m \frac{m(m+1)}{2m+1} [(2-m)t^m + mt^{m+2}] (P_{m+1} - P_{m-1}) \\
 &= -\frac{\text{Pe}}{2} \sum_{l=0}^N C_l \frac{\partial P_l}{\partial x} \sum_{m=2}^N C_m \frac{m(m+1)}{2m+1} [(2-m)t^m + mt^{m+2}] (P_{m+1} - P_{m-1}) \\
 &= -\frac{\text{Pe}}{2} \sum_{l=0}^{2N} \frac{2l+1}{2} P_l \sum_{m=2}^N \sum_{n=2}^N C_n C_m \frac{m(m+1)}{2m+1} [(2-m)t^m + mt^{m+2}] (H_{n,m+1,l} - H_{n,m-1,l})
 \end{aligned} \tag{4.70}$$

Now, each term in the advection-diffusion equation Eq. (4.58) is expressed in terms of Legendre polynomials, and the advection-diffusion equation is reduced successfully in this form $\sum_{l=0}^{\infty} J_l(t) P_l(\cos \theta) = 0$. Then, by combining all the terms, the new advection-

diffusion equation is given by:

$$\begin{aligned}
 & -\text{Pe} \sum_{l=0}^{N+1} \frac{2l+1}{2} P_l \sum_{n=0}^N \frac{2}{3} (t-t^4) C_1 \frac{\partial C_n}{\partial t} G_{n,1,l} \\
 & -\frac{\text{Pe}}{2} \sum_{l=0}^{2N} \frac{2l+1}{2} P_l \sum_{m=2}^N \frac{\partial C_l}{\partial t} C_m m(m+1) (t^{m+1} - t^{m+3}) \sum_{n=0}^N G_{n,m,l} \\
 & -\text{Pe} \sum_{l=0}^{N+1} \frac{2l+1}{2} P_l \sum_{n=0}^N \frac{2}{3} \left(1 + \frac{t^3}{2}\right) C_1 C_n \frac{n(n+1)}{2n+1} G_{n+1,0,l} \\
 & +\text{Pe} \sum_{l=0}^{N-1} \frac{2l+1}{2} P_l \sum_{n=0}^N \frac{2}{3} \left(1 + \frac{t^3}{2}\right) C_1 C_n \frac{n(n+1)}{2n+1} G_{n-1,0,l} \\
 & -\frac{\text{Pe}}{2} \sum_{l=0}^{2N} \frac{2l+1}{2} P_l \sum_{m=2}^N \sum_{n=2}^N C_n C_m \frac{m(m+1)}{2m+1} [(2-m)t^m + mt^{m+2}] (H_{n,m+1,l} - H_{n,m-1,l}) \\
 & - \sum_l \left(t^3 \frac{\partial^2 C_l}{\partial t^2} - l(l+1)tC_l \right) P_l = 0. \tag{4.71}
 \end{aligned}$$

Recalling that Legendre polynomials are orthogonal sequences, the function $J_l(t)$ in the above summation should be zero $\sum_{l=0}^{\infty} J_l(t) P_l(\cos \theta) = 0$. The choice for l leads to l -th order function $J_l(t)$, which needs to be solved numerically, and the relation in Eq. (4.71) allows the function $J_l(t)$ to be generated recursively.

For $0 \leq l \leq N-1$, the function $J_l(t)$ for P_l :

$$\begin{aligned}
 & -\text{Pe} \frac{2l+1}{2} \sum_{n=0}^N \frac{2}{3} (t-t^4) C_1 \frac{\partial C_n}{\partial t} G_{n,1,l} \\
 & -\text{Pe} \frac{2l+1}{4} \sum_{m=2}^N \frac{\partial C_l}{\partial t} C_m m(m+1) (t^{m+1} - t^{m+3}) \sum_{n=0}^N G_{n,m,l} \\
 & -\text{Pe} \frac{2l+1}{2} \sum_{n=0}^N \frac{2}{3} \left(1 + \frac{t^3}{2}\right) C_1 C_n \frac{n(n+1)}{2n+1} G_{n+1,0,l} \\
 & +\text{Pe} \frac{2l+1}{2} \sum_{n=0}^N \frac{2}{3} \left(1 + \frac{t^3}{2}\right) C_1 C_n \frac{n(n+1)}{2n+1} G_{n-1,0,l} \\
 & -\text{Pe} \frac{2l+1}{4} \sum_{m=2}^N \sum_{n=2}^N C_n C_m \frac{m(m+1)}{2m+1} [(2-m)t^m + mt^{m+2}] (H_{n,m+1,l} - H_{n,m-1,l}) \\
 & - \sum_l \left(t^3 \frac{\partial^2 C_l}{\partial t^2} - l(l+1)tC_l \right) P_l = 0 \tag{4.72}
 \end{aligned}$$

For $l = N$, the function $J_l(t)$ for P_l :

$$\begin{aligned}
 & -\text{Pe} \frac{2l+1}{2} \sum_{n=0}^N \frac{2}{3} (t-t^4) C_1 \frac{\partial C_n}{\partial t} G_{n,1,l} \\
 & -\text{Pe} \frac{2l+1}{4} \sum_{m=2}^N \frac{\partial C_l}{\partial t} C_m m(m+1) (t^{m+1} - t^{m+3}) \sum_{n=0}^N G_{n,m,l} \\
 & -\text{Pe} \frac{2l+1}{2} \sum_{n=0}^N \frac{2}{3} \left(1 + \frac{t^3}{2}\right) C_1 C_n \frac{n(n+1)}{2n+1} G_{n+1,0,l} \\
 & -\text{Pe} \frac{2l+1}{4} \sum_{m=2}^N \sum_{n=2}^N C_n C_m \frac{m(m+1)}{2m+1} [(2-m)t^m + mt^{m+2}] (H_{n,m+1,l} - H_{n,m-1,l}) \\
 & - \sum_l \left(t^3 \frac{\partial^2 C_l}{\partial t^2} - l(l+1)t C_l \right) P_l = 0
 \end{aligned} \tag{4.73}$$

For $l = N + 1$, the function $J_l(t)$ for P_l :

$$\begin{aligned}
 & -\text{Pe} \frac{2l+1}{2} \sum_{n=0}^N \frac{2}{3} (t-t^4) C_1 \frac{\partial C_n}{\partial t} G_{n,1,l} \\
 & -\text{Pe} \frac{2l+1}{4} \sum_{m=2}^N \frac{\partial C_l}{\partial t} C_m m(m+1) (t^{m+1} - t^{m+3}) \sum_{n=0}^N G_{n,m,l} \\
 & -\text{Pe} \frac{2l+1}{2} \sum_{n=0}^N \frac{2}{3} \left(1 + \frac{t^3}{2}\right) C_1 C_n \frac{n(n+1)}{2n+1} G_{n+1,0,l} \\
 & -\text{Pe} \frac{2l+1}{4} \sum_{m=2}^N \sum_{n=2}^N C_n C_m \frac{m(m+1)}{2m+1} [(2-m)t^m + mt^{m+2}] (H_{n,m+1,l} - H_{n,m-1,l})
 \end{aligned} \tag{4.74}$$

For $N + 2 \leq l \leq 2N$, the function $J_l(t)$ for P_l :

$$\begin{aligned}
 & -\text{Pe} \frac{2l+1}{4} \sum_{m=2}^N \frac{\partial C_l}{\partial t} C_m m(m+1) (t^{m+1} - t^{m+3}) \sum_{n=0}^N G_{n,m,l} \\
 & -\text{Pe} \frac{2l+1}{4} \sum_{m=2}^N \sum_{n=2}^N C_n C_m \frac{m(m+1)}{2m+1} [(2-m)t^m + mt^{m+2}] (H_{n,m+1,l} - H_{n,m-1,l})
 \end{aligned} \tag{4.75}$$

Note that the number of variables is reduced to the number of governing equations. By numerically solving the Eqs. (4.72) – (4.75), the n th concentration C_n can be explicitly computed to obtain the full picture of velocity distribution.

A natural question arises as to whether there is nonzero velocity for a Janus bead at a finite Péclet number. Indeed, an important question to address is to what extent can the advection affect the locomotion of an active colloid. In the small Péclet number limit ($Pe \ll 1$), the Brownian diffusion of solute particles dominates over advection; the motion of the Janus particle is only slightly perturbed from its equilibrium. On the contrary, when Pe increases and the advection term cannot be neglected in Eq. (4.50), Brownian diffusion is important only in a thin boundary layer on the upstream side of the Janus sphere. According to Eq. (4.50), the boundary layer signifies a balance between radial diffusion ($Pe\mathbf{V} \cdot \nabla C$) and advection ($\nabla^2 C$). In other words, the boundary layer represents (in a frame fixed on the moving colloid) a balance between the strong advection of solute particles (with velocity \mathbf{v}) towards the colloid and diffusion, which enables the solute particles to pass around the (impenetrable) colloid. This suggests that an accumulation of solute particles might occur in the boundary layer. A region of low particle density could be present where the downstream of the colloid carries solute particles away due to the combination of advection and diffusion.

4.2.3 Flow Field

In order to have an insight into motion of a fluid, it is necessary to find an equation of the flow line that passes a spherical swimmer. Consider an explicit form for the velocity

distribution, where the r and θ components of the velocity \mathbf{V} are given by:

$$V_r(r, \theta) = -|\mathbf{V}| \left[1 - \left(\frac{R}{r} \right)^3 \right] \cos \theta + \frac{\mu}{2R} \sum_{l=2}^{\infty} l(l+1) B_l \left[\left(\frac{R}{r} \right)^l - \left(\frac{R}{r} \right)^{l+2} \right] P_l(\cos \theta) \quad (4.76)$$

$$V_\theta(r, \theta) = |\mathbf{V}| \left[1 + \frac{1}{2} \left(\frac{R}{r} \right)^3 \right] \sin \theta + \frac{\mu}{2R \sin \theta} \sum_{l=2}^{\infty} B_l \frac{l(l+1)}{2l+1} \left[(2-l) \left(\frac{R}{r} \right)^l + l \left(\frac{R}{r} \right)^{l+2} \right] [P_{l+1}(\cos \theta) - P_{l-1}(\cos \theta)] \quad (4.77)$$

Here, the colloid size R and the mobility μ are constant. Once the unknown coefficients B_l of the concentration field in Eq. (4.6) is solved, streamlines of a vector field can be visualised.

The velocity profiles in Eqs. 4.76 – 4.77 are in polar coordinate, and they need to be transformed from polar to Cartesian coordinate:

$$\begin{bmatrix} V_x \\ V_y \end{bmatrix} = \begin{bmatrix} \cos \theta & -\sin \theta \\ \sin \theta & \cos \theta \end{bmatrix} \begin{bmatrix} V_r \\ V_\theta \end{bmatrix} \quad (4.78)$$

$$V_x = V_r \cos \theta - V_\theta \sin \theta, \quad (4.79)$$

$$V_y = V_r \sin \theta + V_\theta \cos \theta \quad (4.80)$$

$$r = \sqrt{x^2 + y^2}, \quad \cos \theta = \frac{x}{\sqrt{x^2 + y^2}}, \quad \sin \theta = \frac{y}{\sqrt{x^2 + y^2}} \quad (4.81)$$

By using the converting matrix and the relations between (x, y) and (r, θ) , the velocity in Cartesian coordinate can be written as

$$\begin{aligned}
 V_x &= -|\mathbf{V}| \left[1 - \left(\frac{R}{\sqrt{x^2 + y^2}} \right)^3 \right] \frac{x^2}{x^2 + y^2} \\
 &+ \frac{\mu}{2R} \frac{x}{\sqrt{x^2 + y^2}} \sum_{l=2}^{\infty} l(l+1) B_l \left[\left(\frac{R}{\sqrt{x^2 + y^2}} \right)^l - \left(\frac{R}{\sqrt{x^2 + y^2}} \right)^{l+2} \right] P_l \left(\frac{x}{\sqrt{x^2 + y^2}} \right) \\
 &- |\mathbf{V}| \left[1 + \frac{1}{2} \left(\frac{R}{\sqrt{x^2 + y^2}} \right)^3 \right] \frac{y^2}{x^2 + y^2} \\
 &- \frac{\mu}{2R} \sum_{l=2}^{\infty} B_l \frac{l(l+1)}{2l+1} \left[(2-l) \left(\frac{R}{\sqrt{x^2 + y^2}} \right)^l + l \left(\frac{R}{\sqrt{x^2 + y^2}} \right)^{l+2} \right] \\
 &\quad \left[P_{l+1} \left(\frac{x}{\sqrt{x^2 + y^2}} \right) - P_{l-1} \left(\frac{x}{\sqrt{x^2 + y^2}} \right) \right] \tag{4.82}
 \end{aligned}$$

$$\begin{aligned}
 V_y &= -|\mathbf{V}| \left[1 - \left(\frac{R}{\sqrt{x^2 + y^2}} \right)^3 \right] \frac{xy}{x^2 + y^2} \\
 &+ \frac{\mu}{2R} \frac{y}{\sqrt{x^2 + y^2}} \sum_{l=2}^{\infty} l(l+1) B_l \left[\left(\frac{R}{\sqrt{x^2 + y^2}} \right)^l - \left(\frac{R}{\sqrt{x^2 + y^2}} \right)^{l+2} \right] P_l \left(\frac{x}{\sqrt{x^2 + y^2}} \right) \\
 &+ |\mathbf{V}| \left[1 + \frac{1}{2} \left(\frac{R}{\sqrt{x^2 + y^2}} \right)^3 \right] \frac{xy}{x^2 + y^2} \\
 &+ \frac{\mu x}{2Ry} \sum_{l=2}^{\infty} B_l \frac{l(l+1)}{2l+1} \left[(2-l) \left(\frac{R}{\sqrt{x^2 + y^2}} \right)^l + l \left(\frac{R}{\sqrt{x^2 + y^2}} \right)^{l+2} \right] \\
 &\quad \left[P_{l+1} \left(\frac{x}{\sqrt{x^2 + y^2}} \right) - P_{l-1} \left(\frac{x}{\sqrt{x^2 + y^2}} \right) \right] \tag{4.83}
 \end{aligned}$$

Note that the x and y components of velocity profile in Eqs. (4.82) – (4.83) are in a center of mass frame. Let us transform the inertial frame of reference to the laboratory frame, which is moving with the translation speed $|\mathbf{V}|$ with respect to the center of mass frame. The Cartesian components of the different velocity vectors in the two frames of reference

are

$$V_x = -V_r \cos^2 \theta - V_\theta \sin^2 \theta = -|\mathbf{V}|, \quad (4.84)$$

$$V_y = V_r \sin \theta \cos \theta + V_\theta \cos \theta \sin \theta = 0. \quad (4.85)$$

Hence, the flow lines of vector field can be obtained from the preceding relations.

$$\begin{aligned} V_x &= |\mathbf{V}| \left(\frac{R}{\sqrt{x^2 + y^2}} \right)^3 \frac{x^2}{x^2 + y^2} \\ &+ \frac{\mu}{2R} \frac{x}{\sqrt{x^2 + y^2}} \sum_{l=2}^{\infty} l(l+1) B_l \left[\left(\frac{R}{\sqrt{x^2 + y^2}} \right)^l - \left(\frac{R}{\sqrt{x^2 + y^2}} \right)^{l+2} \right] P_l \left(\frac{x}{\sqrt{x^2 + y^2}} \right) \\ &- \frac{|\mathbf{V}|}{2} \left(\frac{R}{\sqrt{x^2 + y^2}} \right)^3 \frac{y^2}{x^2 + y^2} \\ &- \frac{\mu}{2R} \sum_{l=2}^{\infty} B_l \frac{l(l+1)}{2l+1} \left[(2-l) \left(\frac{R}{\sqrt{x^2 + y^2}} \right)^l + l \left(\frac{R}{\sqrt{x^2 + y^2}} \right)^{l+2} \right] \\ &\left[P_{l+1} \left(\frac{x}{\sqrt{x^2 + y^2}} \right) - P_{l-1} \left(\frac{x}{\sqrt{x^2 + y^2}} \right) \right] \end{aligned} \quad (4.86)$$

$$\begin{aligned} V_y &= -|\mathbf{V}| \left[1 - \left(\frac{R}{\sqrt{x^2 + y^2}} \right)^3 \right] \frac{xy}{x^2 + y^2} \\ &+ \frac{\mu}{2R} \frac{y}{\sqrt{x^2 + y^2}} \sum_{l=2}^{\infty} l(l+1) B_l \left[\left(\frac{R}{\sqrt{x^2 + y^2}} \right)^l - \left(\frac{R}{\sqrt{x^2 + y^2}} \right)^{l+2} \right] P_l \left(\frac{x}{\sqrt{x^2 + y^2}} \right) \\ &+ |\mathbf{V}| \left[1 + \frac{1}{2} \left(\frac{R}{\sqrt{x^2 + y^2}} \right)^3 \right] \frac{xy}{x^2 + y^2} \\ &+ \frac{\mu x}{2Ry} \sum_{l=2}^{\infty} B_l \frac{l(l+1)}{2l+1} \left[(2-l) \left(\frac{R}{\sqrt{x^2 + y^2}} \right)^l + l \left(\frac{R}{\sqrt{x^2 + y^2}} \right)^{l+2} \right] \\ &\left[P_{l+1} \left(\frac{x}{\sqrt{x^2 + y^2}} \right) - P_{l-1} \left(\frac{x}{\sqrt{x^2 + y^2}} \right) \right] \end{aligned} \quad (4.87)$$

4.3 Results

The theoretical framework of advection-diffusion for a Janus particle has already been developed in the section 4.2. In the following section, various methods of analysis are employed to find analytic or numerical solutions in order to obtain the concentration profile. Solving the advection-diffusion equation for large N is challenging as it is necessary to face the intricate nonlinearity and singularities. Attempting to continue the expansion to higher order in t and Pe in Eq. (4.71) is not necessary as the algebra becomes rapidly intractable. Therefore, the nonlinear equations in Eqs. (4.72) – (4.75) are numerically solved by finite N . To fully determine the function $J_l(t)$ with unknown coefficients $C_l(t, Pe)$, the advection diffusion equation Eq. (4.71) must be accompanied with appropriate boundary conditions.

At infinity, the concentration is a constant, in this instance called constant b .

$$\sum_{l=0}^N C_l(0) = \text{constant} = b \quad (4.88)$$

Substituting the variable t , the boundary condition Eq. (4.51) reads

$$\sum_{l=0}^N t^2 \partial_t C_l(t)|_{t=1} P_l = K(\theta) \quad (4.89)$$

Here, the coverage function $K(\theta)$ could also be expanded by Legendre polynomials [88]

$$K(\theta) = \sum_{l=0}^{\infty} F_l P_l(\cos \theta), \quad (4.90)$$

$$F_l = - \left(\frac{1}{2} \right)^{\frac{l-1}{2}} \frac{(2l+1)(l-2)!!}{4 \left(\frac{l+1}{2} \right)!}, \quad (4.91)$$

$$F_0 = \frac{1}{2}, F_1 = \frac{3}{4}, F_2 = 0, F_3 = -\frac{7}{16} \dots \quad (4.92)$$

The boundary conditions for $N = 2$ are

$$C_0(0) = \text{constant} = b = 0, \quad C_1(0) = 0, \quad C_2(0) = 0 \quad (4.93)$$

$$t^2 \partial_t C_0|_{t=1} = \frac{1}{2}, \quad t^2 \partial_t C_1|_{t=1} = \frac{3}{4}, \quad t^2 \partial_t C_2|_{t=1} = 0 \quad (4.94)$$

Due to the orthogonal property of Legendre polynomials, all the order functions J_l for $N = 2$ ought to be zero and have the following forms.

The function $J_0(t)$ for $P_0 = 1$:

$$-\frac{2}{9}\text{Pe}(t-t^4)C_1\frac{\partial C_1}{\partial t}-\frac{3}{5}\text{Pe}(t^3-t^5)C_2\frac{\partial C_2}{\partial t}+\frac{4}{9}\text{Pe}\left(1+\frac{t^3}{2}\right)C_1^2+\frac{6}{5}\text{Pet}^4C_2^2-t^3\frac{\partial^2 C_1}{\partial t^2}=0 \quad (4.95)$$

The function $J_1(t)$ for $P_1 = \cos \theta$:

$$\begin{aligned} &-\frac{2}{3}\text{Pe}(t-t^4)C_1\frac{\partial C_0}{\partial t}+\frac{4}{15}\text{Pe}(t-t^4)C_1\frac{\partial C_2}{\partial t}-\frac{6}{5}\text{Pe}(t^3-t^5)C_2\frac{\partial C_1}{\partial t} \\ &+\frac{4}{5}\text{Pe}\left(1+\frac{t^3}{2}\right)C_1C_2+\frac{6}{5}\text{Pet}^4C_1C_2-t^3\frac{\partial^2 C_1}{\partial t^2}+2tC_1=0 \end{aligned} \quad (4.96)$$

The function $J_2(t)$ for $P_2 = \frac{1}{2}(3\cos^2\theta - 1)$:

$$\begin{aligned} &-\frac{4}{9}\text{Pe}(t-t^4)C_1\frac{\partial C_1}{\partial t}-3\text{Pe}(t^3-t^5)C_2\frac{\partial C_0}{\partial t}-\frac{6}{7}\text{Pe}(t^3-t^5)C_2\frac{\partial C_2}{\partial t} \\ &-\frac{4}{9}\text{Pe}\left(1+\frac{t^3}{2}\right)C_1^2+\frac{6}{7}\text{Pet}^4C_2^2-t^3\frac{\partial^2 C_2}{\partial t^2}+6tC_2=0 \end{aligned} \quad (4.97)$$

The function $J_3(t)$ for $P_3 = \frac{1}{2}(5\cos^3\theta - 3\cos\theta)$:

$$-\frac{2}{5}\text{Pe}(t-t^4)C_1\frac{\partial C_2}{\partial t}-\frac{9}{5}\text{Pe}(t^3-t^5)C_2\frac{\partial C_1}{\partial t}-\frac{4}{5}\text{Pe}\left(1+\frac{t^3}{2}\right)C_1C_2-\frac{6}{5}\text{Pet}^4C_1C_2=0 \quad (4.98)$$

The function $J_4(t)$ for $P_4 = \frac{1}{8}(35\cos^4\theta - 30\cos^2\theta + 3)$:

$$-\frac{54}{35}\text{Pe}(t^3-t^5)C_2\frac{\partial C_2}{\partial t}-\frac{72}{35}\text{Pet}^4C_2^2=0 \quad (4.99)$$

Clearly, the advection-diffusion equations in Eqs. (4.72) – (4.75) have two regular singular points at $t = 0$ and $t = 1$. A new, tiny variable t_0 is used to avoid boundary problem with singularities, and the nonlinear-differential equation is approximately solved in the region $t_0 \leq t \leq 1 - t_0$. In practice, the new variable t_0 is between 0.0001 to 0.00001 in the code.

4.3.1 Advection-Diffusion in Two Limits

To simplify the problem, two special cases are considered first. One is the case in the boundary layer, and the other is at infinity. At the surface of the colloid $t = R/r = 1$, the nonlinear equations Eqs. (4.95) – (4.97) are reduced

$$\frac{2}{3}\text{Pe}C_1^2 + \frac{6}{5}\text{Pe}C_2^2 - \frac{\partial^2 C_0}{\partial t^2} = 0 \quad (4.100)$$

$$\frac{12}{5}\text{Pe}C_1C_2 + 2C_1 - \frac{\partial^2 C_1}{\partial t^2} = 0 \quad (4.101)$$

$$-\frac{2}{3}\text{Pe}C_1^2 + \frac{6}{7}\text{Pe}C_2^2 + 6C_2 - \frac{\partial^2 C_2}{\partial t^2} = 0 \quad (4.102)$$

When numerically solving the reduced equations, the solutions of unknown coefficient C_l are obtained and all are a function of Péclet number Pe , as shown in Figures 4.1 – 4.3. As the advection becomes increasingly important, both C_0 and C_1 are monotonically decreasing functions of Pe , and reach their minimums of 0.1 and 0.2, respectively. On the contrary, C_2 initially rises with Pe , and this growth persists until $\text{Pe} \approx 30$ where C_2 reaches its maximum. Beyond $\text{Pe} \approx 30$ there is a decline of C_2 to its limiting value of 0.06 for $\text{Pe} = 100$.

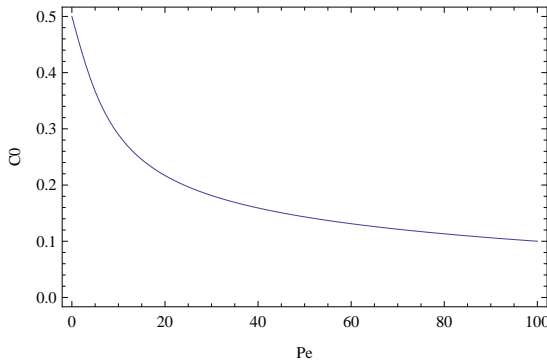


Figure 4.1: For $N = 2$ and $t \rightarrow 1$, the C_0 of surface concentration as a function of Pe

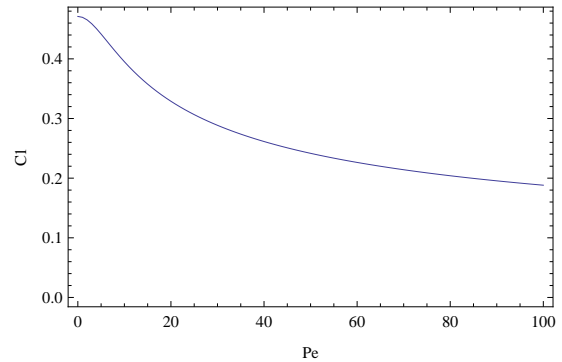


Figure 4.2: For $N = 2$ and $t \rightarrow 1$, the C_1 of surface concentration as a function of Pe

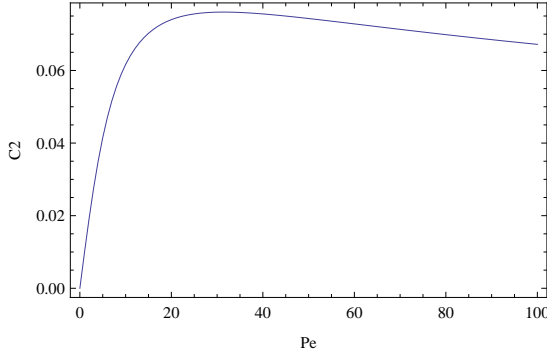


Figure 4.3: For $N = 2$ and $t \rightarrow 1$, the C_2 of surface concentration as a function of Pe

The resulting concentration profile is given by

$$C(1, \theta) = \sum_{l=0}^2 C_l(1) P_l(\cos \theta) \quad (4.103)$$

$$= C_0 + C_1 \cos \theta + C_2 \frac{1}{2} (3 \cos^2 \theta - 1) \quad (4.104)$$

After computing the coefficients C_0 , C_1 , and C_2 , the surface concentration of the solute is also illustrated as a function of Pe and the polar angles θ . Figures 4.4 – 4.6 indicate that the surface concentration of solute descends gradually and becomes constant as $Pe \rightarrow 100$ for fixed polar angles ($\theta = 0, \frac{\pi}{4}, \frac{\pi}{2}$).

In addition, there is a depletion of the surface concentration of solute in the region $0 \leq \theta \leq \pi$ and this angular dependence is shown in Figures 4.7 – 4.9. For different Péclet numbers ($Pe = 1, 10, 100$), the surface concentration displays a considerably reduction and approaches zero as $\theta \rightarrow \pi$. The depletion closely reflects the form of coverage function for a Janus sphere.

In the other extreme case, in which t is very small, only the linear terms in the nonlinear equations Eqs. (4.95) – (4.97) need to be kept. This approach will also reduce the nonlinear

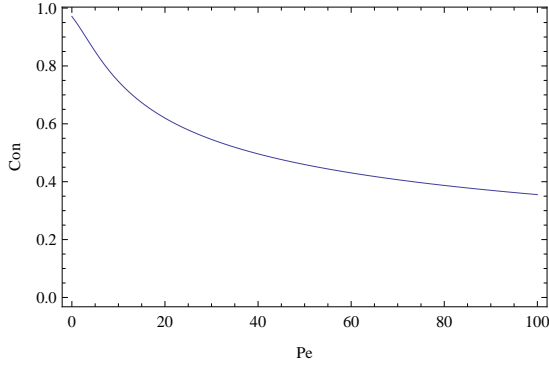


Figure 4.4: For $N = 2$ and $t \rightarrow 1$, the surface concentration v.s. Pe for $\theta = 0$

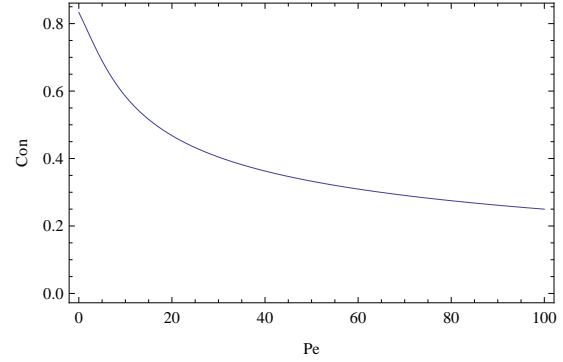


Figure 4.5: For $N = 2$ and $t \rightarrow 1$, the surface concentration v.s. Pe for $\theta = \frac{\pi}{4}$

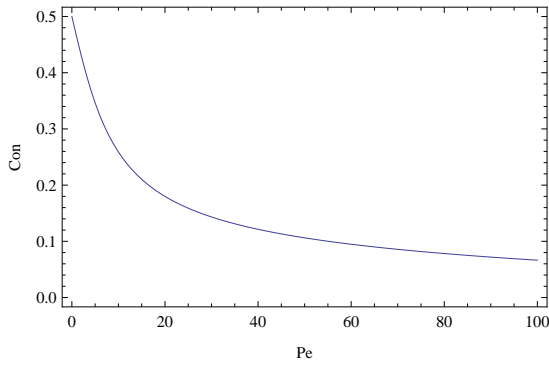


Figure 4.6: For $N = 2$ and $t \rightarrow 1$, the surface concentration v.s. Pe for $\theta = \frac{\pi}{2}$

equations because these equations will all be first order differential equations rather than second order.

$$-\frac{2}{9}Pe t C_1 \frac{\partial C_1}{\partial t} + \frac{4}{9}Pe C_1^2 = 0 \quad (4.105)$$

$$-\frac{2}{3}Pe t C_1 \frac{\partial C_0}{\partial t} - \frac{4}{15}Pe t C_1 \frac{\partial C_2}{\partial t} + \frac{4}{5}Pe C_1 C_2 + 2t C_1 = 0 \quad (4.106)$$

$$-\frac{4}{9}Pe t C_1 \frac{\partial C_1}{\partial t} - \frac{4}{9}Pe C_1^2 + 6C_2 = 0 \quad (4.107)$$

The analytic solution of the concentration coefficient is exactly found and has a simple form:

$$C_0 = \frac{3}{Pe}t, \quad C_1 = at^2, \quad C_2 = \frac{2}{9}Pe a^2 t^3 \quad (4.108)$$

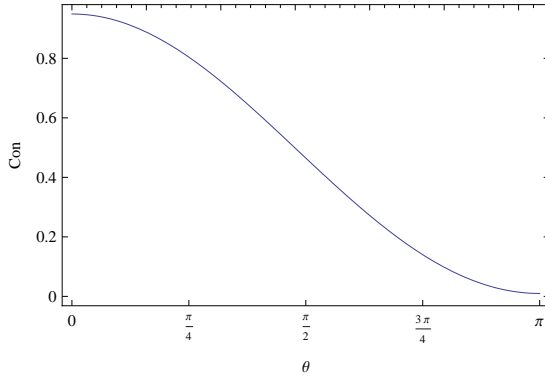


Figure 4.7: For $N = 2$ and $t \rightarrow 1$, the surface concentration v.s. θ for $Pe = 1$

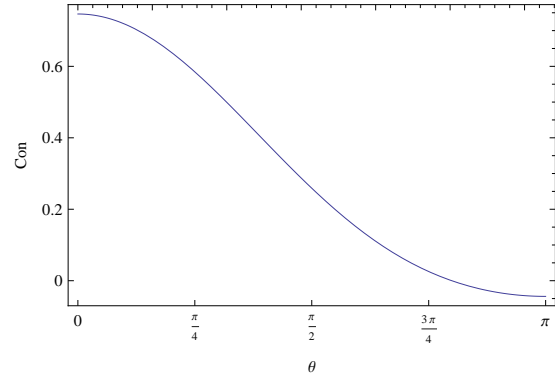


Figure 4.8: For $N = 2$ and $t \rightarrow 1$, the surface concentration v.s. θ for $Pe = 10$

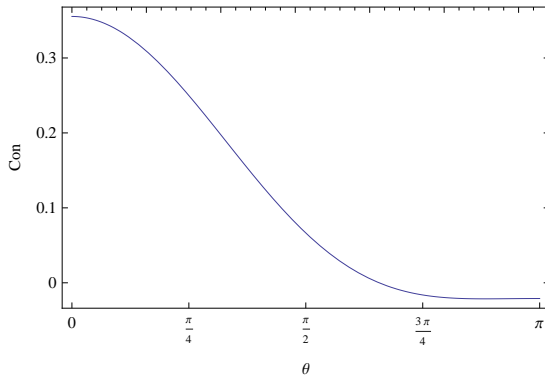


Figure 4.9: For $N = 2$ and $t \rightarrow 1$, the surface concentration v.s. θ for $Pe = 100$

where a is an arbitrary constant. In order to avoid a regular singular point, t is set as small value t_0 ($t_0 = 0.00001$ in the programme) instead of 0 to approach the case at infinity. Despite the different values of θ , the results in Figures (4.10) – (4.12) share the same trend, in which the concentration decays with Pe , and this trend continues until approaching its minimum as $Pe \rightarrow 100$. In addition, the concentration furthest away from the Janus colloid remains a constant for different polar angles, as shown in Figures (4.13) – (4.15). When the variable t decreases, the first term in concentration distribution C_0 becomes a leading order. As C_0 is inversely proportional to Pe , the concentration varies

inversely with the Pe as well.

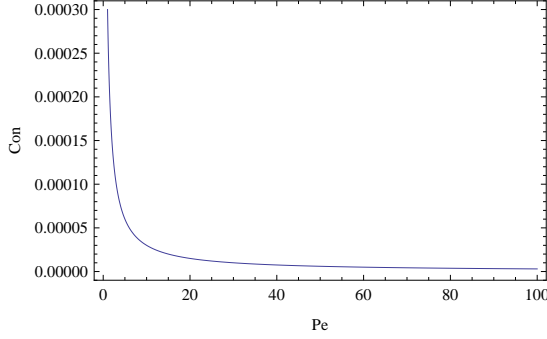


Figure 4.10: For $N = 2$ and $t \rightarrow 0$, the concentration at infinity v.s. Pe for $\theta = 0$

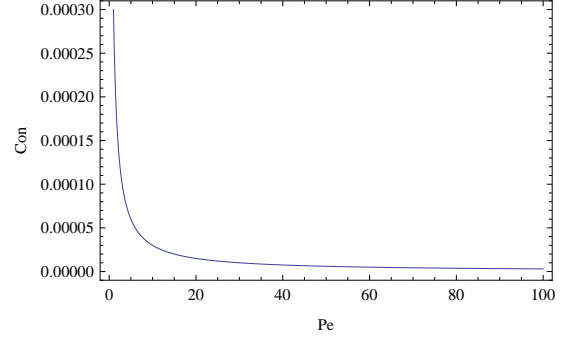


Figure 4.11: For $N = 2$ and $t \rightarrow 0$, the concentration at infinity v.s. Pe for $\theta = \frac{\pi}{4}$

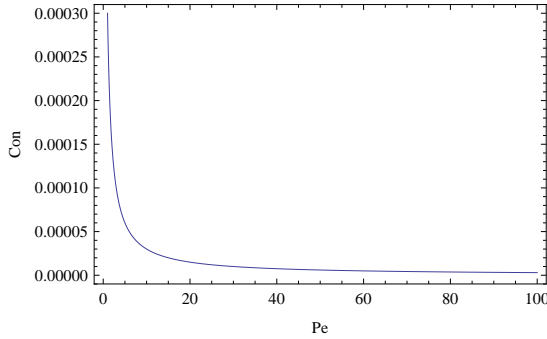


Figure 4.12: For $N = 2$ and $t \rightarrow 0$, the concentration at infinity v.s. Pe for $\theta = \frac{\pi}{2}$

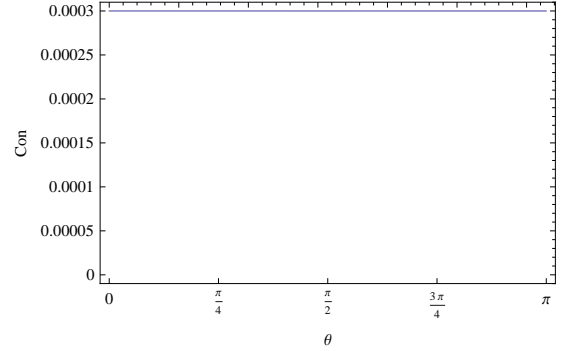


Figure 4.13: For $N = 2$ and $t \rightarrow 0$, the concentration at infinity v.s. θ for Pe = 1

Similarly, the boundary conditions for $N = 3$ are

$$C_0(0) = 0, \quad C_1(0) = 0, \quad C_2(0) = 0, \quad C_3(0) = 0 \quad (4.109)$$

$$t^2 \partial_t C_0|_{t=1} = \frac{1}{2}, \quad t^2 \partial_t C_1|_{t=1} = \frac{3}{4}, \quad t^2 \partial_t C_2|_{t=1} = 0, \quad t^2 \partial_t C_3|_{t=1} = -\frac{7}{16} \quad (4.110)$$

At the surface of the colloid $t = R/r = 1$, the advection-diffusion equation for $N = 3$ can

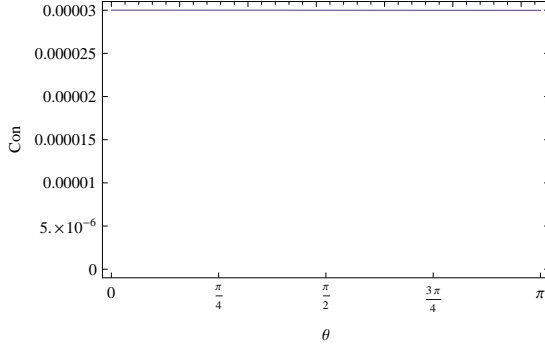


Figure 4.14: For $N = 2$ and $t \rightarrow 0$, the concentration at infinity v.s. θ for $Pe = 10$

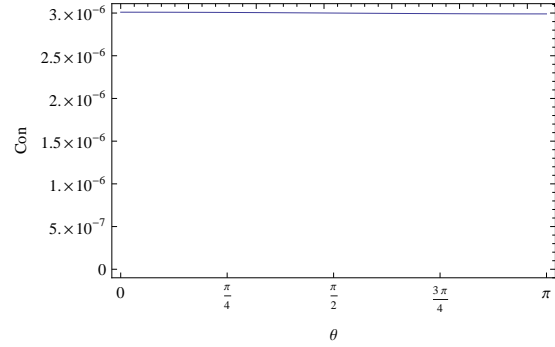


Figure 4.15: For $N = 2$ and $t \rightarrow 0$, the concentration at infinity v.s. θ for $Pe = 100$

be simplified as follows.

$$\frac{2}{3}PeC_1^2 + \frac{6}{5}PeC_2^2 + \frac{12}{7}PeC_3^2 - \frac{\partial^2 C_0}{\partial t^2} = 0 \quad (4.111)$$

$$\frac{12}{5}PeC_1C_2 + \frac{144}{35}PeC_2C_3 + 2C_1 - \frac{\partial^2 C_1}{\partial t^2} = 0 \quad (4.112)$$

$$-\frac{2}{3}PeC_1^2 + \frac{6}{7}PeC_2^2 + \frac{12}{7}PeC_3^2 + \frac{24}{7}PeC_1C_3 + 6C_2 - \frac{\partial^2 C_2}{\partial t^2} = 0 \quad (4.113)$$

$$-\frac{12}{5}PeC_1C_2 + \frac{8}{5}PeC_2C_3 + 12C_3 - \frac{\partial^2 C_3}{\partial t^2} = 0 \quad (4.114)$$

For $N = 3$, the numerical solutions of the concentration distribution for different Pe are seen in Figures (4.16) – (4.19) and show qualitatively similar behaviour with those for $N = 2$.

When t is very small, only the linear terms in the advection-diffusion equation need to be kept and the advection-diffusion for $N = 3$ can be rewritten as

$$-\frac{2}{9}PetC_1 \frac{\partial C_1}{\partial t} + \frac{4}{9}PeC_1^2 = 0 \quad (4.115)$$

$$-\frac{2}{3}PetC_1 \frac{\partial C_0}{\partial t} - \frac{4}{15}PetC_1 \frac{\partial C_2}{\partial t} + \frac{4}{5}PeC_1C_2 + 2tC_1 = 0 \quad (4.116)$$

$$-\frac{4}{9}PeC_1^2 + \frac{8}{7}PeC_1C_3 + 6tC_2 - \frac{4}{9}PetC_1 \frac{\partial C_1}{\partial t} - \frac{2}{7}PetC_1 \frac{\partial C_3}{\partial t} = 0 \quad (4.117)$$

$$-\frac{4}{5}PeC_1C_2 + 12tC_3 - \frac{2}{5}PetC_1 \frac{\partial C_2}{\partial t} = 0 \quad (4.118)$$

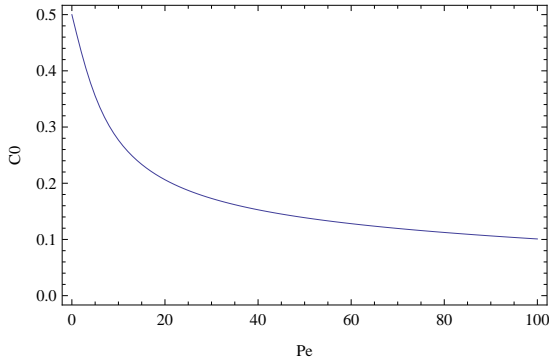


Figure 4.16: For $N = 3$ and $t \rightarrow 1$, the C_0 of surface concentration as a function of Pe

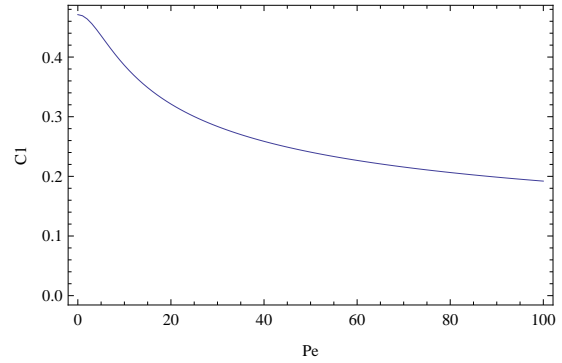


Figure 4.17: For $N = 3$ and $t \rightarrow 1$, the C_1 of surface concentration as a function of Pe

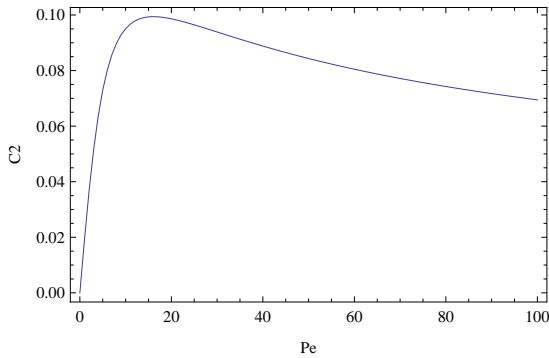


Figure 4.18: For $N = 3$ and $t \rightarrow 1$, the C_2 of surface concentration as a function of Pe

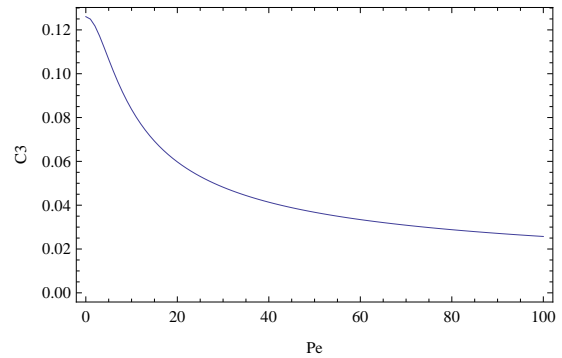


Figure 4.19: For $N = 3$ and $t \rightarrow 1$, the C_3 of surface concentration as a function of Pe

However, it may not always be possible to find analytical solutions to advection-diffusion equations in the domain where t is small. Having analysed the advection-diffusion equation to the two limits ($t \rightarrow 1, t \rightarrow 0$), what do these results for the limits mean physically and what can they tell us about the behaviour at the inbetween values of t . Next, the methods used to perform the numerical computations are introduced in the following subsection.

4.3.2 Advection-Diffusion in General Condition

Turning the attention to more general cases ($1 > t > 0$) for finite Pe , the concentration profile is computed via a numerical solution of the full advection-diffusion equations

in Eqs. (4.72) – (4.75).

For $N = 1$, the advection-diffusion equations and the boundary conditions are

$$\frac{4}{9}\text{Pe}(1 + \frac{1}{2}t^3)C_1^2 - \frac{2}{9}\text{Pe}(t - t^4)C_1 \frac{\partial C_1}{\partial t} - t^3 \frac{\partial C_0}{\partial t} = 0, \quad (4.119)$$

$$2tC_1 - \frac{2}{3}\text{Pe}(t - t^4)C_1 \frac{\partial C_0}{\partial t} - t^3 \frac{\partial C_1}{\partial t} = 0, \quad (4.120)$$

$$C_0(0) = 0, \quad C_1(0) = 0, \quad (4.121)$$

$$t^2 \partial_t C_0|_{t=1} = \frac{1}{2}, \quad t^2 \partial_t C_1|_{t=1} = \frac{3}{4}. \quad (4.122)$$

For $N = 2$, the advection-diffusion equation has been shown in Eqs. (4.95) – (4.97).

The numerical solutions of the concentration coefficients are plotted versus t for different N in Figures (4.20) – (4.33). The results reveal that C_0 is always linear with t and C_1 increases in the region $0 < t < 1$. In Figures (4.34) – (4.37), the concentration decreases gradually with the polar angle θ and all profiles of the concentration for different N are in a consistent manner.

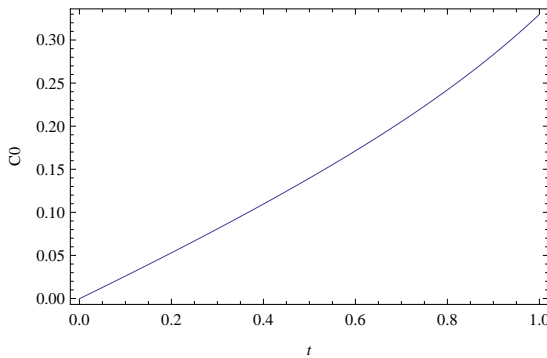


Figure 4.20: For $N = 1$, C_0 as a function of t

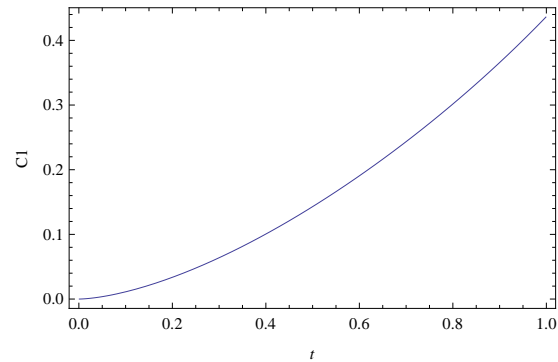


Figure 4.21: For $N = 1$, C_1 as a function of t

According to Eqs. (4.56) – (4.57), C_1 is directly related to the leading order of the velocity, hence the behaviour of C_1 is important and needs to be specifically analysed.

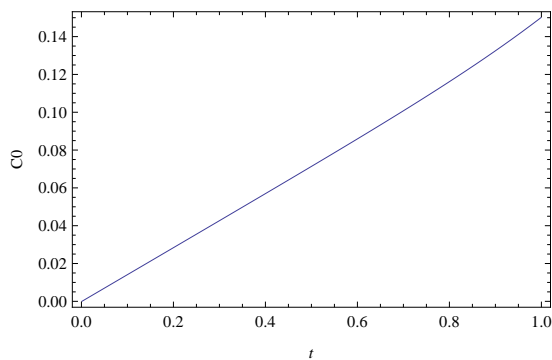


Figure 4.22: For $N = 2$, C_0 as a function of t

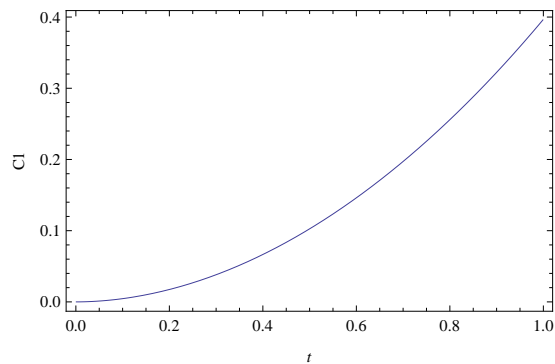


Figure 4.23: For $N = 2$, C_1 as a function of t

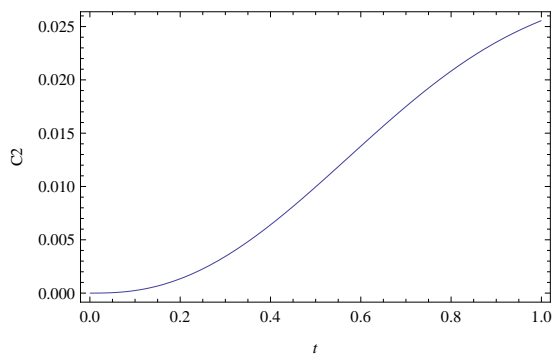


Figure 4.24: For $N = 2$, C_2 as a function of t

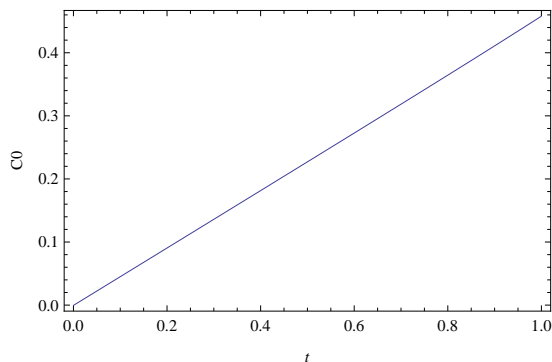


Figure 4.25: For $N = 3$, C_0 as a function of t

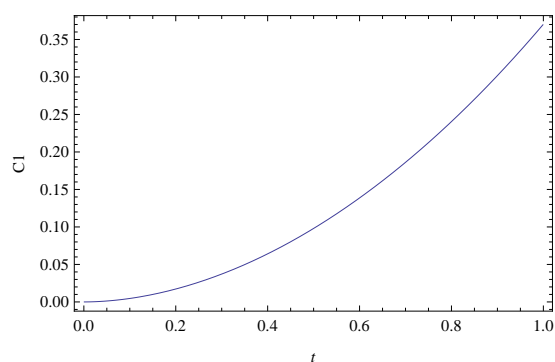


Figure 4.26: For $N = 3$, C_1 as a function of t

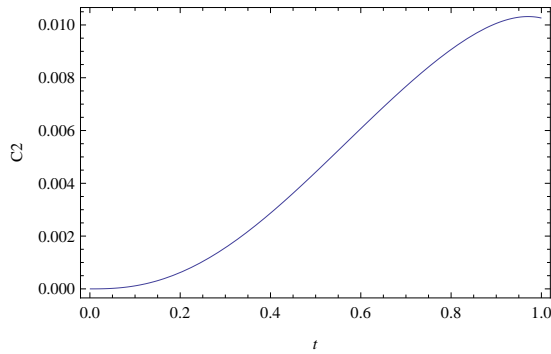


Figure 4.27: For $N = 3$, C_2 as a function of t

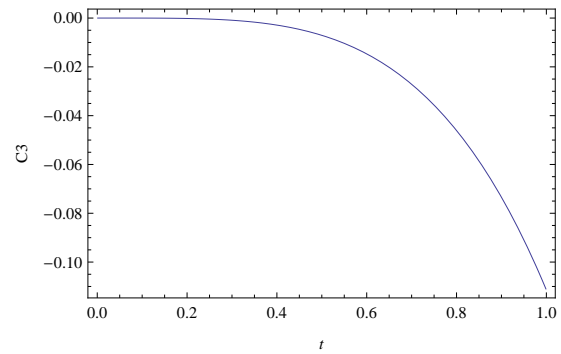


Figure 4.28: For $N = 3$, C_3 as a function of t

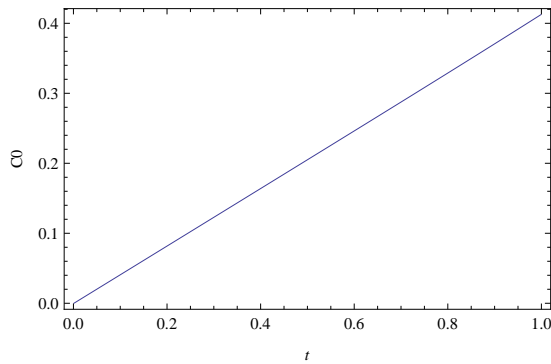


Figure 4.29: For $N = 4$, C_0 as a function of t

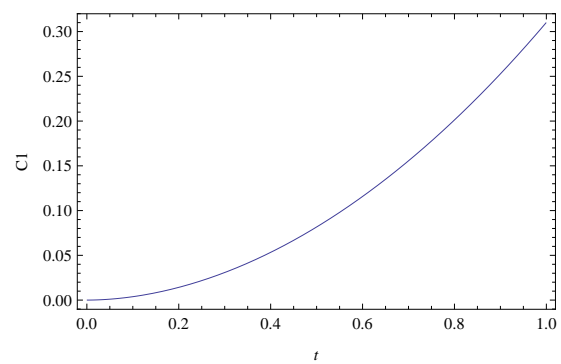


Figure 4.30: For $N = 4$, C_1 as a function of t

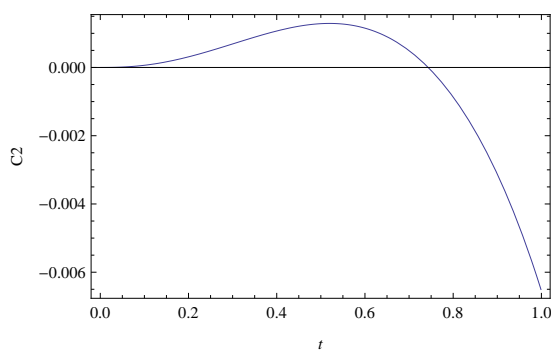


Figure 4.31: For $N = 4$, C_2 as a function of t

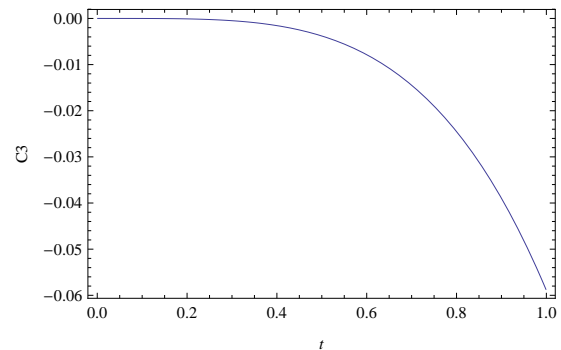


Figure 4.32: For $N = 4$, C_3 as a function of t

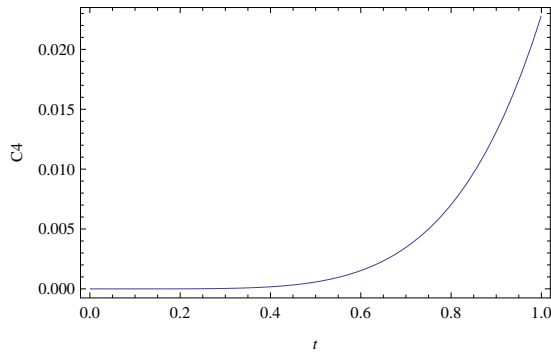


Figure 4.33: For $N = 4$, C_4 as a function of t

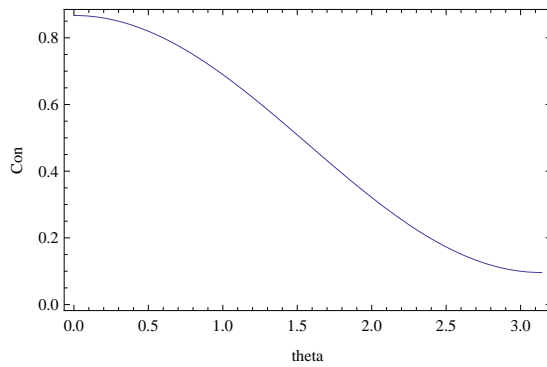


Figure 4.34: For $N = 1$ and $Pe = 1$, the surface concentration v.s. θ

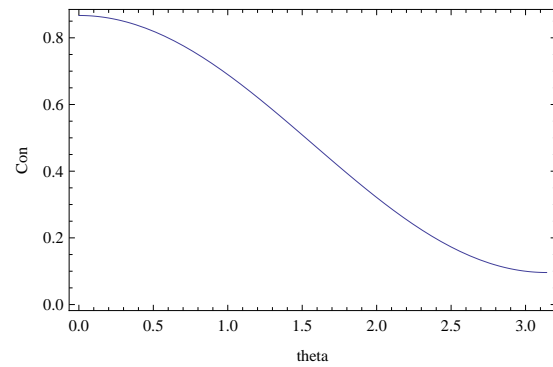


Figure 4.35: For $N = 2$ and $Pe = 1$, the surface concentration v.s. θ

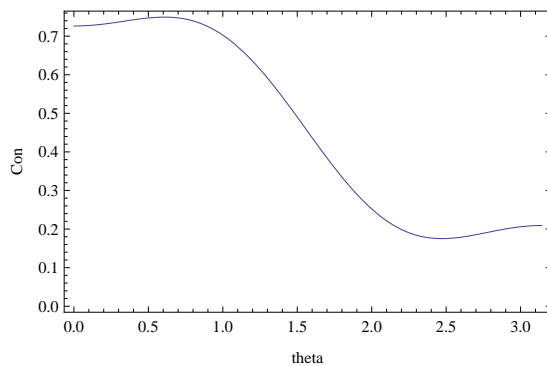


Figure 4.36: For $N = 3$ and $Pe = 1$, the surface concentration v.s. θ

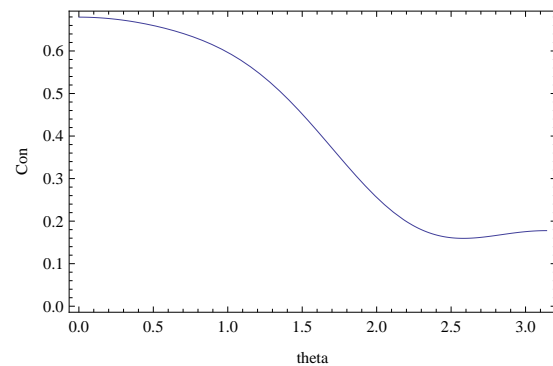


Figure 4.37: For $N = 4$ and $Pe = 1$, the surface concentration v.s. θ

Figures (4.38) – (4.41) illustrate C_1 as a function of Pe for $N = 1, 2, 3, 4$ and the results show that there is a sudden decline in the concentration in the region $0 \leq Pe \leq 10$. This behaviour is rather unexpected and suggests that there is no self-propulsion even if the advection becomes dominant over the flow.

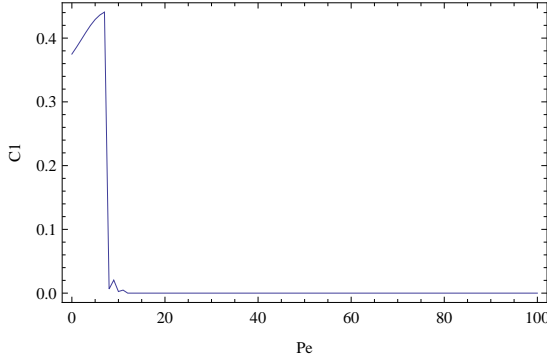


Figure 4.38: For $N = 1$, C_1 v.s. Pe

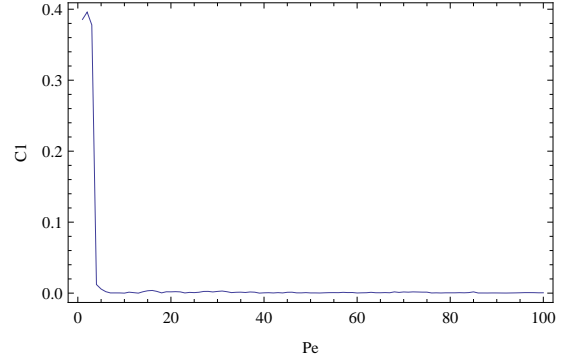


Figure 4.39: For $N = 2$, C_1 v.s. Pe

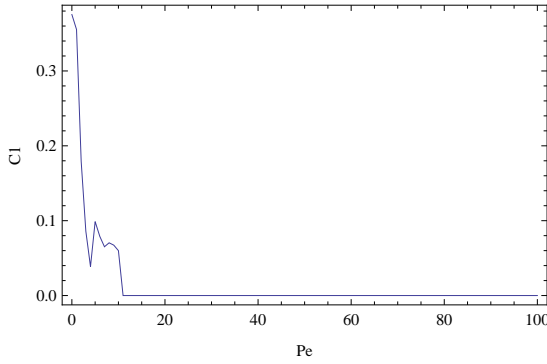


Figure 4.40: For $N = 3$, C_1 v.s. Pe

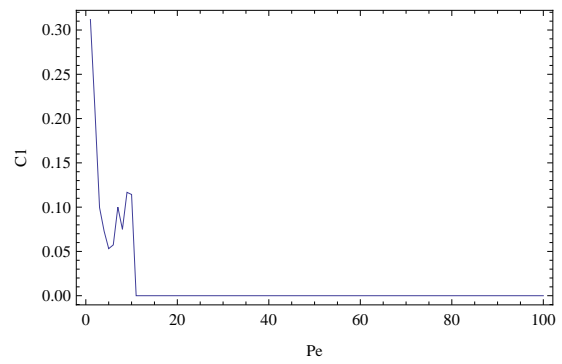


Figure 4.41: For $N = 4$, C_1 v.s. Pe

By solving the full set of advection-diffusion equations, the Janus colloid can achieve an autonomous propulsion at a small Pe , but its velocity becomes zero, due to no symmetry breaking at a large Pe . For $N = 4$, concentration distribution of the solute and the corresponding contour plot with different Pe are illustrated in Figures 4.42 – 4.45. If the Péclet number is small ($Pe \sim \mathcal{O}(1)$), this leads to an increasing mobility, and the strong inward advective flux of solute particles in the upstream region causes an accumulation in

the boundary layer at the surface of the colloid. Figures 4.42 – 4.43 indicate that there is an accumulation of particles around the Janus colloid at its thin upstream boundary layer for $Pe = 1$. However, this accumulation zone disappears for $Pe = 100$ shown in Figures 4.44 – 4.45, and it implies that the Janus sphere comes to equilibrium. With higher Pe , effects of advection become more important than diffusion in fluid, and causes larger solute advection in the vicinity of the sphere. If solute molecules move very rapidly to the side with low solute concentration, it could balance concentration gradient soon, and no longer maintain asymmetric distribution of solute concentration around the colloid. As a result, no propulsion is created due to no symmetry breaking for $Pe = 100$.

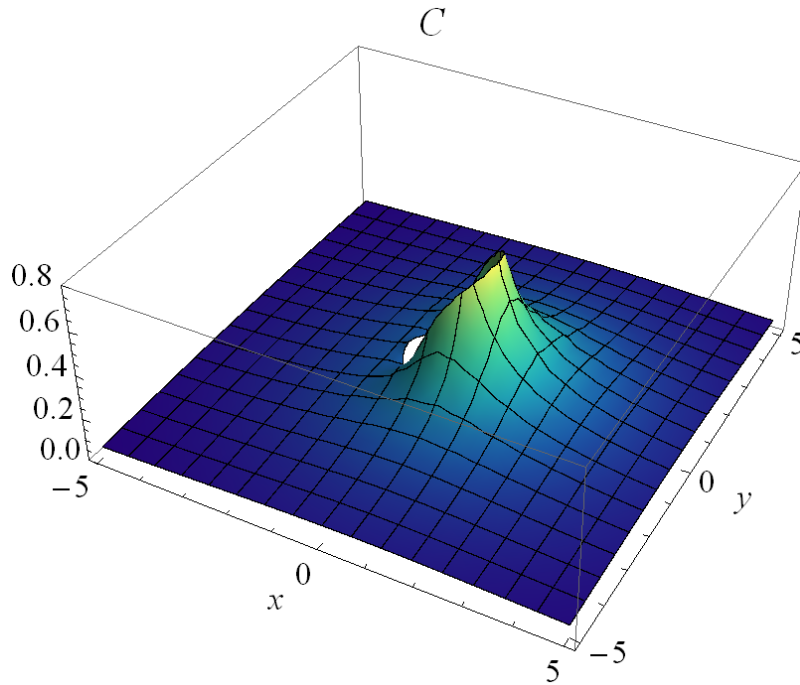


Figure 4.42: For $N = 4$, $Pe = 1$, the concentration distribution of the solute for a Janus sphere in 3D.

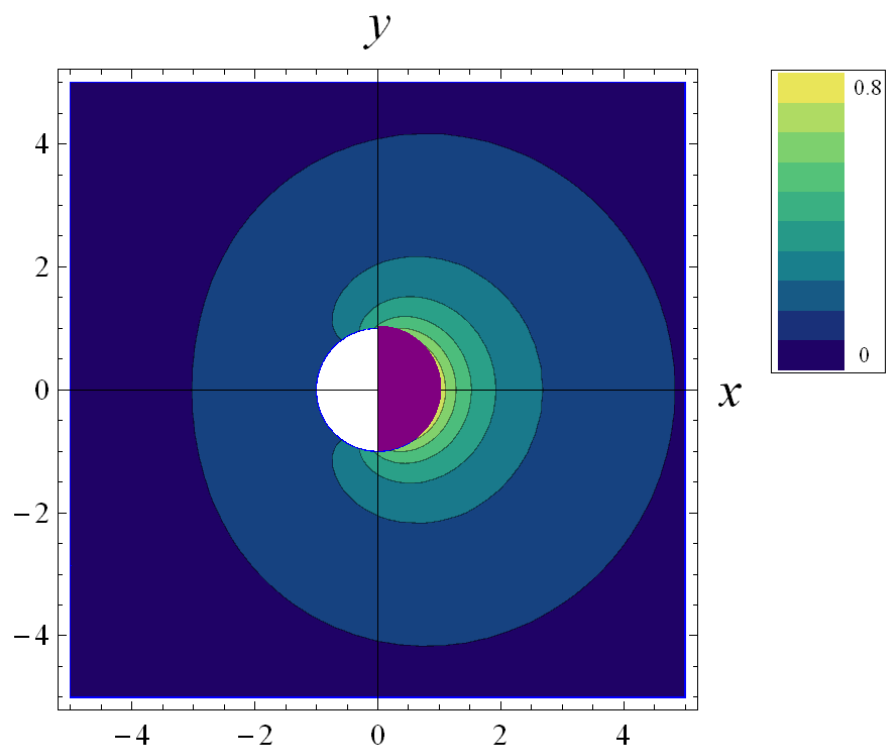


Figure 4.43: For $N = 4$, $Pe = 1$, the contour plot for the concentration profile of the solute and an accumulation in the vicinity of the Janus sphere in its upstream region. The Janus colloid is placed in the centre, and color bar indicates high (yellow) versus low (dark blue) concentration.

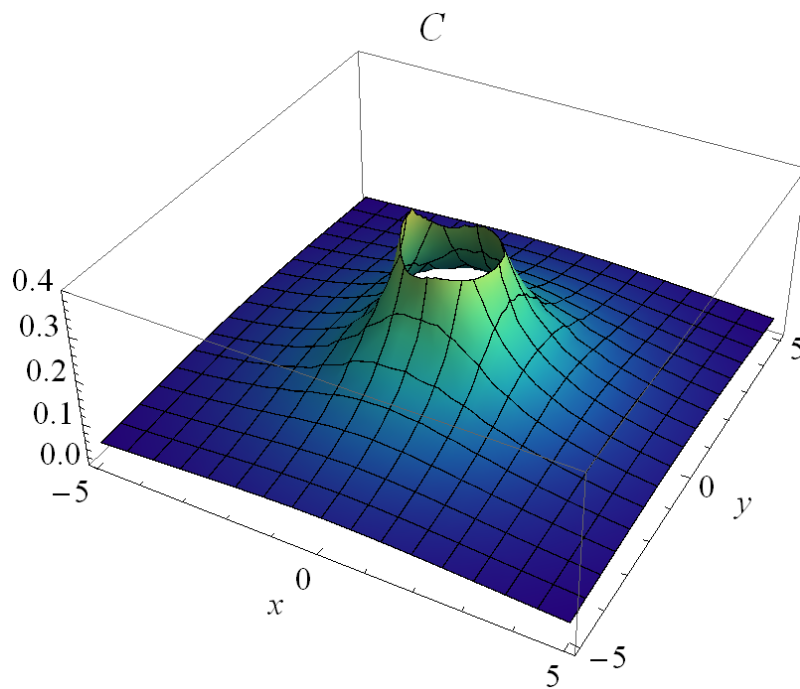


Figure 4.44: For $N = 4$, $Pe = 100$, the concentration distribution of the solute for a Janus sphere in 3D.

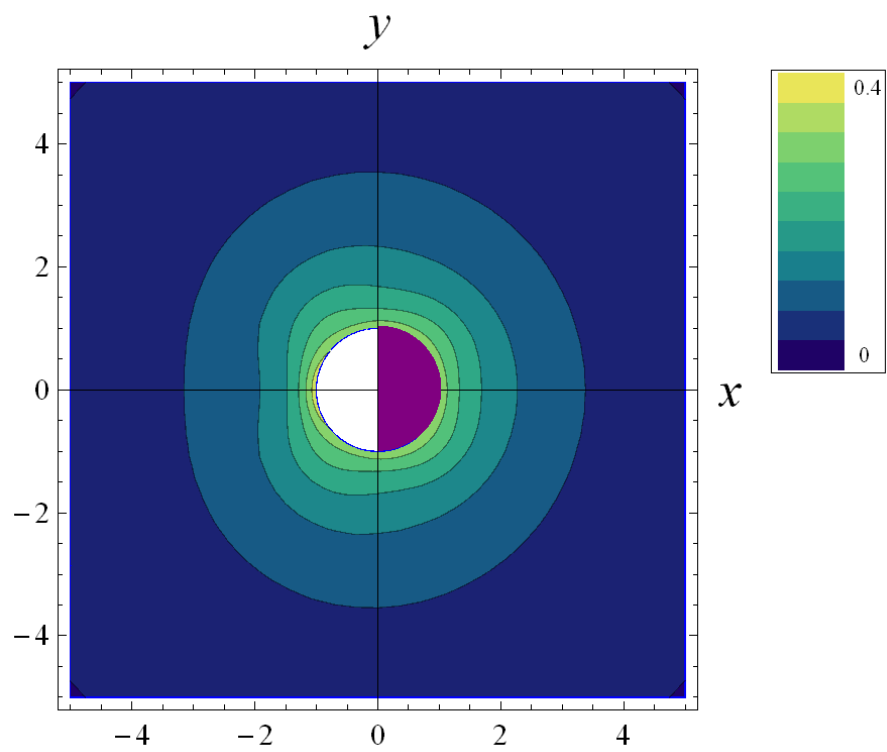


Figure 4.45: For $N = 4$, $Pe = 100$, the contour plot for the concentration profile of the solute. There is no an accumulation of particles because of no symmetry breaking.

4.3.3 Flow Field for Janus and Inhomogeneous Spheres

The framework of flow field introduced in section 4.2.3 can be applied to diffusion-reaction model in Chapter 3. Once the full picture of the concentration of the solute is known, the flow field for Janus colloid can be determined. The streamlines of this flow for a number of representative values of $\frac{k_1 C_\infty}{k_2}$ and $\frac{k_1 R}{D_{hp}}$ were studied in order to present the different qualitative phenomena.

For Janus colloid, Figures 4.46 – 4.48 illustrate the streamlines for the regions I, II and III in Figure 3.8 respectively. In regimes I and II, there is always a net flow parallel to the swimming direction at the front of the sphere. However, the flow field in regime III, shown in Figure 4.48, displays qualitatively striking features. In order to explore the complex pattern in regime III, more flow plots with different parameters $\frac{k_1 C_\infty}{k_2}$ and $\frac{k_1 R}{D_{hp}}$ are studied. According to Figures 4.48 – 4.52, less and less net flow is observed in the region III, where the propulsion velocity of the Janus sphere is expected to decay with $1/R$ dependence. These figures for different regions illustrate the process of how the flow fields changed from one region to another.

Furthermore, the motion of a fluid for inhomogeneous sphere is also computed with similar procedure, and is shown in Figures 4.53 – 4.55 corresponding to three different regions in Figure 3.9. The flow patterns in the vicinity of inhomogeneous colloid in region I and II are symmetric with respect to the midplane, and this is similar to Janus case. Increasing the size parameter $\frac{k_1 R}{D_{hp}}$ leads to a complex flow field in regime III, where size dependence of propulsion velocity comes into play, and this reveals an asymmetric pattern rather than symmetric one. For larger colloid size, there are additional circulations in the vicinity of the particle. For comparison, the fluid flows more smoothly around the

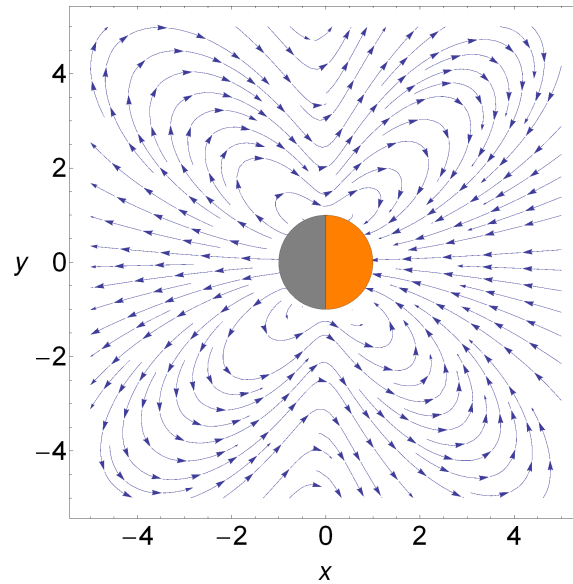


Figure 4.46: The flow field around the Janus sphere for $\frac{k_1 C_\infty}{k_2} = 0.5$ and $\frac{k_1 R}{D_{hp}} = 0.5$ in region I of the diagram in Figure 3.8.

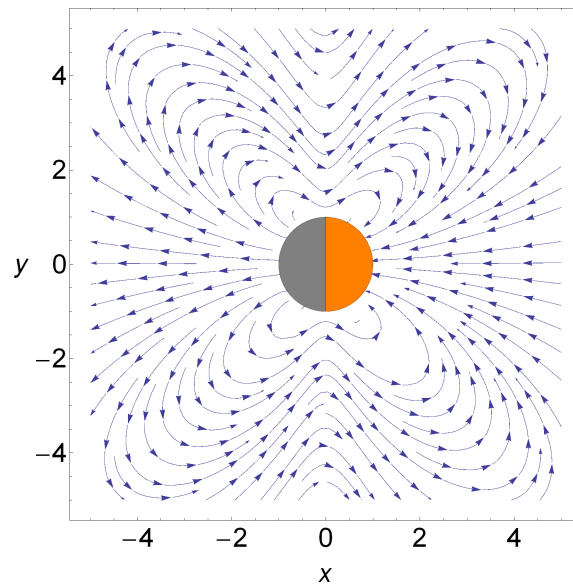


Figure 4.47: The flow field around the Janus sphere for $\frac{k_1 C_\infty}{k_2} = 5$ and $\frac{k_1 R}{D_{hp}} = 0.5$ in region II of the diagram in Figure 3.8.

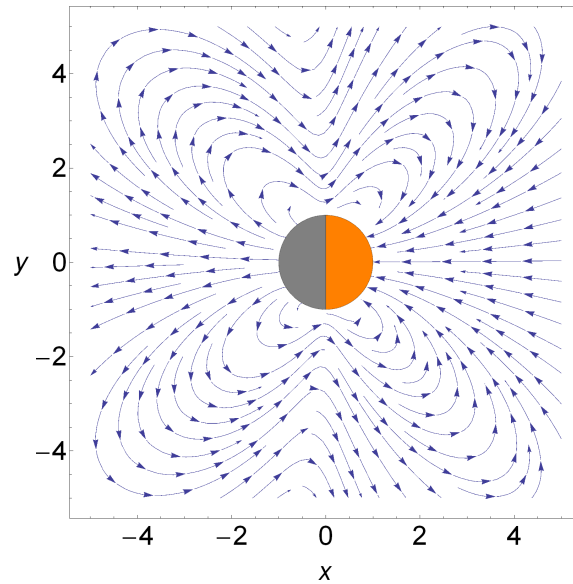


Figure 4.48: The flow field around the Janus sphere for $\frac{k_1 C_\infty}{k_2} = 0.5$ and $\frac{k_1 R}{D_{hp}} = 1$ in region III of the diagram in Figure 3.8.

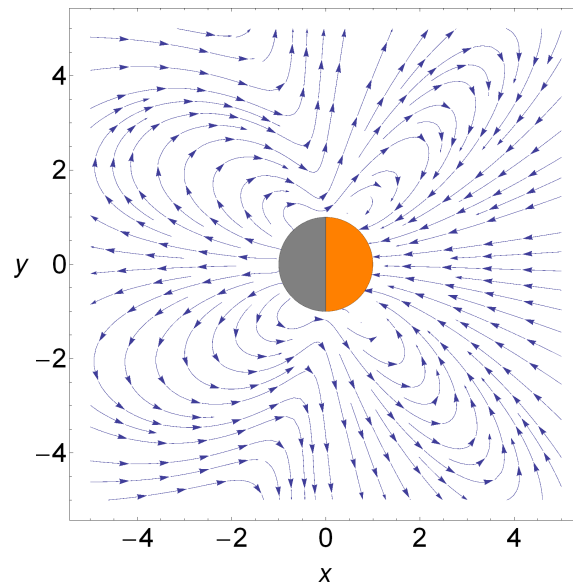


Figure 4.49: The flow field around the Janus sphere for $\frac{k_1 C_\infty}{k_2} = 0.5$ and $\frac{k_1 R}{D_{hp}} = 5$ in region III of the diagram in Figure 3.8.

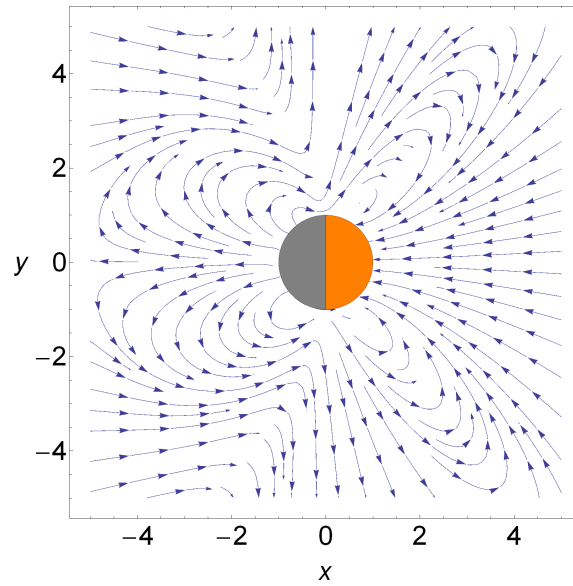


Figure 4.50: The flow field around the Janus sphere for $\frac{k_1 C_\infty}{k_2} = 0.5$ and $\frac{k_1 R}{D_{hp}} = 10$ in region III of the diagram in Figure 3.8.

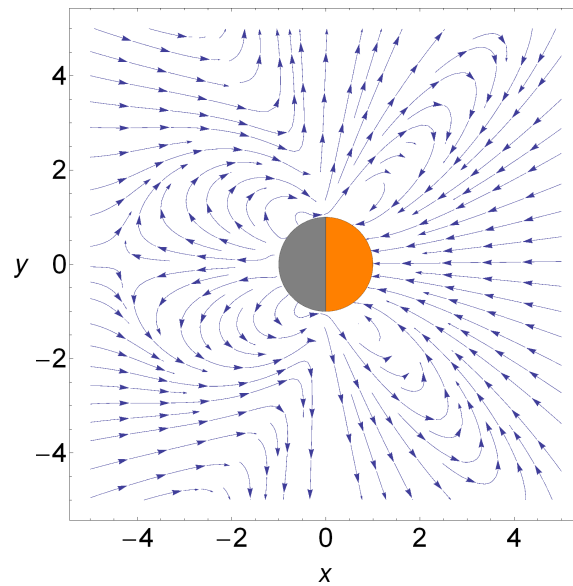


Figure 4.51: The flow field around the Janus sphere for $\frac{k_1 C_\infty}{k_2} = 0.5$ and $\frac{k_1 R}{D_{hp}} = 20$ in region III of the diagram in Figure 3.8.

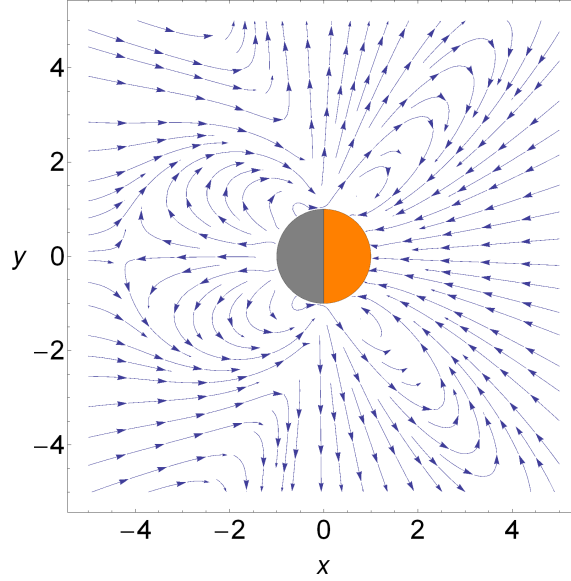


Figure 4.52: The flow field around the Janus sphere for $\frac{k_1 C_\infty}{k_2} = 0.5$ and $\frac{k_1 R}{D_{hp}} = 50$ in region III of the diagram in Figure 3.8.

inhomogeneous sphere in regions I and II than that moves in region III, and this difference reflects the role of size dependence at large size limit.

4.4 Summary

To summarise, the model of advection-diffusion has been constructed to compute the concentration and velocity of a Janus sphere suspended in fluid. By solving the full set of advection-diffusion equations, the Janus colloid can achieve an autonomous propulsion at a small Pe , but its velocity becomes zero due to no symmetry breaking at the large Pe limit. In addition, for both Janus and inhomogeneous spheres propelled by diffusion-reaction, size effect has a major impact on the flow field for large colloids.

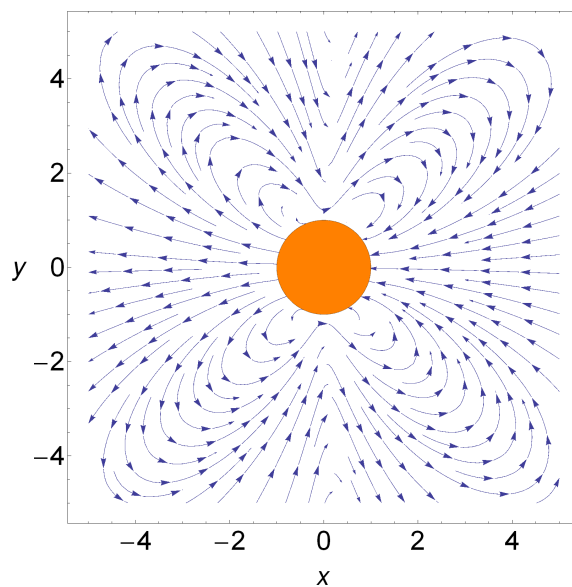


Figure 4.53: The flow field around the inhomogeneous sphere for $\frac{k_1 C_\infty}{k_2} = 0.5$ and $\frac{k_1 R}{D_{hp}} = 0.5$ in region I of the diagram in Figure 3.9.

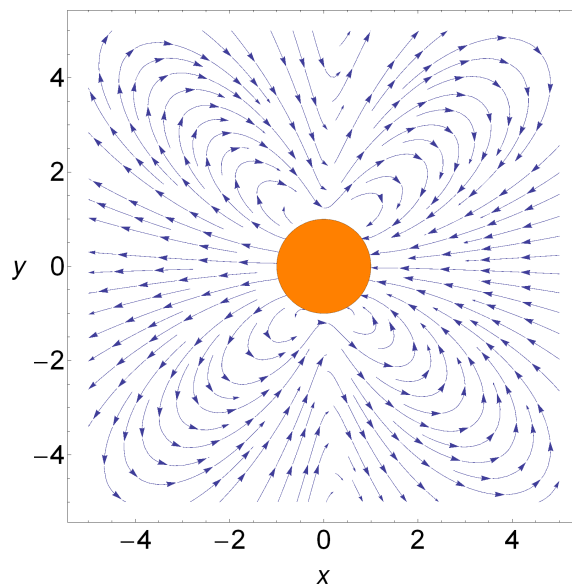


Figure 4.54: The flow field around the inhomogeneous sphere for $\frac{k_1 C_\infty}{k_2} = 5$ and $\frac{k_1 R}{D_{hp}} = 0.5$ in region II of the diagram in Figure 3.9.

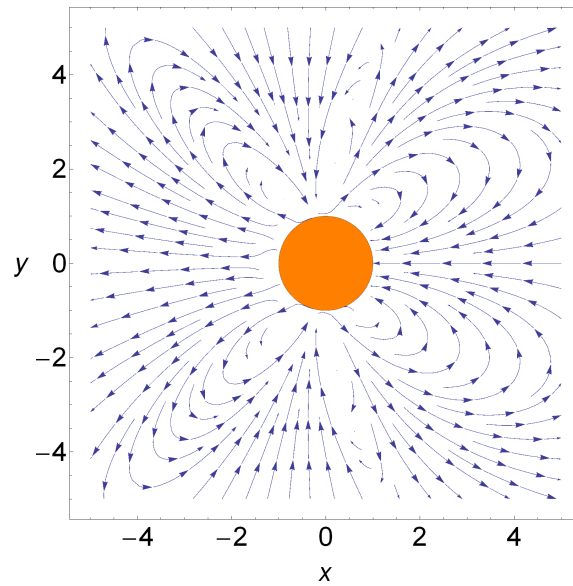


Figure 4.55: The flow field around the inhomogeneous sphere for $\frac{k_1 C_\infty}{k_2} = 0.5$ and $\frac{k_1 R}{D_{hp}} = 50$ in region III of the diagram in Figure 3.9.

Chapter 5

Conclusion

5.1 Conclusion and discussion

The last decade has witnessed the emergence of a new paradigm in biological motility: transport activities undertaken by molecular motors and dynamics of colloids in fluid at the micro- or nanoscale. While advances in experimental techniques for the design of artificial swimming robots have proceeded considerably, theoretical developments have struggled to keep pace. In order to overcome this gap, this work was devoted to exploring the physical characteristics of active colloids that asymmetrically catalyse a chemical reaction and to provide a perspective on the propulsion of colloidal dispersions from a microscale viewpoint.

A model of diffusion-reaction has been established and is an extension of previous theories [82] and [73]. The approach in Chapter 3 employs a combination of analytical and numerical techniques. In addition, there are some simplifying assumptions in the analysis presented in section 3.2. The catalytic activity occurring on the surface of the colloid is considered as a two-step process. However, there could be more intermediate steps in

the chemical reaction. It is assumed that the main qualitative results will not be affected by the more complicated kinetic route of the decomposition of substrate catalysed by the enzyme. Another assumption is that advection is neglected in the diffusion-reaction model.

By building upon the theoretical framework presented in section 3.2, both Janus and inhomogeneous colloids can achieve self-propulsion by the diffusiophoretic effect and this mechanism is based on the fact that the asymmetry of the coated catalyst dominates the mobility. Such spontaneous symmetry breaking can be observed in all regions in Figures 3.8 – 3.9. When the fuel concentration is small ($\frac{k_1 C_\infty}{k_2} < 1$), a Janus sphere can displace itself. Furthermore, its swimming velocity is proportional to the concentration of solute. The enhancement of the displacement of a Janus colloid has been verified in a previous experiment [72]. Nevertheless, the effect of fuel concentration on propulsion velocity is reduced for higher concentration of solute. Although the previous theory [82] implies that the velocity of a Janus sphere is independent of its radius, the results in Chapter 3 indicate that the propulsion velocity of the Janus particle is inversely proportional to the size at the large size limit ($\frac{k_1 R}{D_{hp}} > 1$), and the $1/R$ behaviour is expected to disappear for smaller colloids. Evidence from the current experiment [73] demonstrates that the velocity of a Janus colloid displays the $1/R$ size dependence in an experiment accessible range (250 nm to 5 μ m). As a consequence, the theory developed in Chapter 3 can explain the influence of fuel concentration as well as the observed size dependence of propulsion velocity for the Janus colloid and is consistent with these previous experiments [72] [73]. Furthermore, this analysis is then extended to an inhomogeneous colloid with asymmetric catalyst. Compared with Janus particles, while an inhomogeneous sphere has similar behaviour for propulsion velocity at small size limits, its propulsion velocity exhibits a decay with $1/R^2$ dependence at large size limits.

The role played by advection-diffusion in the motion of a Janus colloid was examined in Chapter 4. The concentration is computed as a function of Péclet number. The combination of advection and diffusion generates and maintains the concentration gradient for low Péclet number ($0 < Pe < 10$). Since there is symmetry breaking, this leads to an accumulation of solute particles in the boundary layer and effective autonomous propulsion for the Janus sphere. By contrast, the accumulation zone disappears when advection overwhelmingly dominates the flow at high Pe . As a result, the Janus colloid undergoes a random walk and its mean velocity becomes zero. As no symmetry breaking is observed in the region of $10 < Pe < 100$, the dispersion exerts an entropic or depletion force on the Janus colloid, and the presence of strong advection does not result in any enhancement of diffusion.

There is another theory that indicates self-propulsion, due to an accumulation of Janus particles, is linked to Péclet number. Recently, a minimal analysis suggests that advection is able to lead to symmetry breaking in the phoretic motion of a Janus colloid, and the particle is predicted to translate with propulsion velocities in a regime of finite Péclet number [75]. There are two advantages of the theory constructed in Chapter 4. In presenting the numerical procedure for determining the concentration distribution and propulsion velocity for an active colloid, the flows are driven by a far field uniform flow. Another advantage of the theoretical framework that has been presented here is that it readily adopts other forms of far field flow. The formulation described in Chapter 3 and Chapter 4 would remain largely unchanged, except for a slight modification of the value of the boundary condition in the domain; that which corresponds to infinity (in the fluid domain). To summarise, the character of the accumulation of particles reflects the competition between advection, driving the suspension out of equilibrium, and Brownian diffusion, acting to restore equilibrium; both of these effects are considerably influenced by the nature of the

hydrodynamic interactions between particles.

Overall, the theoretical framework for active colloids in the thesis provides a way to interpret existing experimental results and endeavours to give an overview of the partial answers that have been proposed or that can be inferred to date. Although the complete picture has not yet been formulated, it is hoped that the investigation presented in this thesis will be of benefit to more researchers.

5.2 Future landscape

Eventually, there will be other physical scenarios where the ideas in this thesis will be used to study other interesting problems. Firstly, a natural extension is to combine together the two frameworks, namely the two-step kinetic route for diffusion-reaction and the advection-diffusion model. In addition, the theory can be applied to mechanisms with an external concentration gradient and external shear flows.

Next, the theoretical framework developed in sections 3.2 and 4.2 may be extended to study the self-propulsion of a Pt/Au catalytic nanomotor powered by electrocatalytic reactions. The motion of a bimetallic rod-shaped nanomotor is driven by fluid slip around the nanomotor's surface due to a coupling of charge density and electric fields. The governing equations for the phoretic motion of an asymmetric catalysed colloid are very similar to those of electrochemical reactions, except that the motion of the charged or dielectric object is induced by its interaction with an ambient electric field.

It should be noted that, in this discussion, only one active colloid has been considered. Therefore, it is possible to extend the theory to a system, consisting of two or more colloids

with asymmetric catalysts. The interaction between different particles could induce a considerably enhanced diffusion than an individual one. In this way, a train of colloids moving through the dispersion can cause interesting collective behaviour when they interact via the gradient of the fields that they also use for self-propulsion. The generic properties of such self-propelled colloids provide a route for pattern formation in colloidal dispersions, and perhaps other complex fluids. Lastly, the locomotion of self-propelled active colloids, due to interfacial phoretic transport, has been explored and this fascinating world of the swimming characteristics of colloidal dispersions awaits future research.

Bibliography

- [1] J. William Schopf, *Phil. Trans. R. Soc. B.* **361**(1470), 869 (2006).
- [2] W. Altermann and J. Kazmierczak , *Research in Microbiology* **154**(9), 611 (2003).
- [3] T. Cavalier-Smith, *Phil. Trans. R. Soc. Lond. B. Biol. Sci.* **361**(1470): 969 (2006).
- [4] D.C. Savage, *Annual Review of Microbiology* **31**, 107 (1977).
- [5] R. Berg, *Trends in Microbiology* **4**(11), 430 (1996).
- [6] M.T. Madigan, J.M. Martinko, D. Stahl, and D.P. Clark, *Brock Biology of Microorganisms*, 13th Edition (Pearson Education, New Jersey, 2010).
- [7] C. Zimmer, *How Microbes Defend and Define us*, *New York Times* (2010), (<http://www.nytimes.com/2010/07/13/science/13micro.html>).
- [8] P. Nelson, *Biological Physics: Energy, Information, Life*, (Freeman, New York, 2003).
- [9] I. Ibañez-Tallon, N. Heintz, and H. Omran, *Hum. Mol. Genet.* **12**, R27-R35 (2003).
- [10] A.L. Cogen, V. Nizet, and R.L. Gallo, *British Journal of Dermatology* **158**(3), 442 (2008).
- [11] D. Bray, *Cell Movements*, 2nd Edition (Garland Publishing, New York, 2000).
- [12] O. Reynolds, *Philos. Trans.* **174**, 935 (1895).

- [13] S. Vogel, *Life in Moving Fluids: The Physical Biology of Flow*, 2nd Edition (Princeton University Press, 1994).
- [14] A. Cavalcanti, T. Hogg, and B. Shirinzadeh, *Nanorobotics System Simulation in 3D Workspaces with Low Reynolds Number*, IEEE-RAS MHS International Symposium on Micro-Nanomechatronics and Human Science, 1-6 (2006).
- [15] J.P. Heller, *American Journal of Physics* **28**(4), 348 (1960).
- [16] D.B. Dusenbery, *Living at Micro Scale: The Unexpected Physics of Being Small*, (Harvard University Press, Cambridge, 2009).
- [17] S.J. Ebbens and J.R. Howse, *Soft matter* **6**, 726 (2010).
- [18] H.C. Berg and R.A. Anderson, *Nature* **245**, 380 (1973).
- [19] H.C. Berg, *E. Coli in Motion*, (Springer, New York, 2004).
- [20] F. Jülicher, A. Ajdari, and J. Prost, *Rev. Mod. Phys.* **69**, 1269 (1997).
- [21] R.D. Astumian, *Science* **276**, 917 (1997).
- [22] E. Lauga and T.R. Powers, *Rep. Prog. Phys.* **72**, 096601 (2009).
- [23] I.R. Gibbons, *J. Cell Biol.* **91**, 107 (1981).
- [24] R.D. Vale and R.A. Milligan, *Science* **288**, 88 (2000).
- [25] E.M. Purcell, *American Journal of Physics* **45**, 3 (1977).
- [26] A. Najafi and R. Golestanian, *Physical Review E* **69**, 062901 (2004).
- [27] A. Najafi and R. Golestanian, *J. Phys.: Condens. Matter* **17**, S1203 (2005).
- [28] R. Golestanian, A. Ajdari, *Phys. Rev. Lett.* **100**, 038101 (2008).

- [29] R. Dreyfus, J. Baudry, M.L. Roper, M. Fermigier, H.A. Stone, and J. Bibette, *Nature* **437**, 862 (2005).
- [30] Y.F. Mei, G.S. Huang, A.A. Solovev, E. Bermudez Urena, I. Moench, F. Ding, T. Reindl, R. K.Y. Fu, P.K. Chu, and O.G. Schmidt, *Advanced Materials* **20**, 4085 (2008).
- [31] G. Alexander and J.M. Yeomans, *Europhys. Lett.* **83**, 34006 (2008).
- [32] P. Tierno, R. Golestanian, I. Pagonabarraga, and F. Sagués *Phys.Rev. Lett.* **101**, 218304 (2008).
- [33] P. Tierno, R. Golestanian, I. Pagonabarraga, and F. Sagués, *J. Phys. Chem. B* **112**(51), 16525 (2008).
- [34] P. Tierno, O. Güell, F. Sagués, R. Golestanian, and I. Pagonabarraga, *Phys. Rev. E* **81**, 011402 (2010).
- [35] H. Masoud, B.I. Bingham, and A. Alexeev, *Soft Matter* **8**, 8944 (2012).
- [36] W. Gao, A. Uygun, and J. Wang, *J. Am. Chem. Soc.* **134**(2), 897 (2012).
- [37] M.L. Ekiel-Jezewska and E. Wajnryb, *J. Phys. Condens. Matter* **21**, 204102 (2009).
- [38] R. Dominguez and K.C. Holmes, *Annual Review of Biophysics* **40**, 169 (2011).
- [39] J. van der Gucht, E. Paluch, J. Plastino, and C. Sykes, *Proc. Natl. Acad. Sci. USA* **102**(22), 7847 (2005).
- [40] L.A. Cameron, M.J. Footer, A.V. Oudenaarden, and J.A. Theriot, *Proc. Natl. Acad. Sci. USA* **96**(9), 4908 (1999).
- [41] J. Plastino and C. Sykes, *Current Opinion in Cell Biology* **17**(1), 62 (2005).

- [42] L. F. Valadares, Y.-G. Tao, N. S. Zacharia, V. Kitaev, F. Galembeck, R. Kapral, and G. A. Ozin, *Small* **6**, 565 (2010).
- [43] A.E. Carlsson, *Annual Review of Biophysics* Vol. **39**, 91 (2010).
- [44] J.L. Anderson, *Annu. Rev. Fluid Mech.* **21**, 61 (1989).
- [45] F.F. Reuss, *Mem. Soc. Imperiale Naturalistes Moscow* **2**, 327 (1809).
- [46] S.S. Dukhin and B.V. Derjaguin *Electrokinetic Phenomena* (J. Willey & Sons, New York, 1974).
- [47] A.S. Dukhin and P.J. Goetz, *Ultrasound for Characterizing Colloids Particle Sizing, Zeta Potential Rheology*, (Elsevier, 2002).
- [48] P. Mitchell, *Fed. Eur. Biochem. Soc. Lett.* **28**, 1 (1972).
- [49] P.E. Lammert, J. Prost, and R. Bruinsma, *J. Theor. Biol.* **178**(4), 387 (1996).
- [50] W.F. Paxton, K.C. Kistler, C.C. Olmeda, A. Sen, S.K. St. Angelo, Y. Cao, T.E. Mallouk, P.E. Lammert, and V.H. Crespi, *J. Am. Chem. Soc.* **126**, 13424 (2004).
- [51] W.F. Paxton, P.T. Baker, T.R. Kline, Y. Wang, T.E. Mallouk, and A. Sen, *J. Am. Chem. Soc.* **128**, 14881 (2006).
- [52] W.F. Paxton, S. Sundararajan, T.E. Mallouk, and A. Sen, *Angew. Chem., Int. Ed.* **45**(33), 5420 (2006).
- [53] N. Mano and A. Heller, *J. Am. Chem. Soc.* **127**(33), 11574 (2005).
- [54] T.R. Kline, W.F. Paxton, T.E. Mallouk, and A. Sen, *Angew. Chem., Int. Ed.* **44**(5), 744 (2005).
- [55] J.M. Catchmark, S. Subramanian, and A. Sen, *Small* **1**(2), 202 (2005).

- [56] R. Laocharoensuk, J. Burdick, and J. Wang, ACS Nano **2**(5), 1069 (2008).
- [57] J. Burdick, R. Laocharoensuk, P.M. Wheat, J.D. Posner, and J.Wang, J. Amer. Chem. Soc. **130**(26), 8164 (2008).
- [58] S.M. Rafelski, J.B. Alberts, and G.M. Odell, PLOS Comp. Biol. **5**(7), e1000434 (2009).
- [59] C. Ludwig, Sitzungsber. Akad. Wiss. Wien, Math.-Naturwiss. Kl., Abt. 2A **20**, 539 (1856).
- [60] C. Soret, Arch. Sci. Phys. Nat. **2**, 48 (1879).
- [61] E. Ruckenstein, J. Colloid Interface Sci. **83**(1), 77 (1981).
- [62] K.I. Morozov, JETP **88**, 944 (1999).
- [63] R. Piazza and A. Parola, J. Phys.: Condens. Matter **20**, 153102 (2008).
- [64] S.N. Rasuli and R. Golestanian, J. Phys.: Condens. Matter **17**, S1171 (2005).
- [65] R. Piazza and A. Guarino, Phys. Rev. Lett. **88**, 208302 (2002).
- [66] D. Rings, R. Schachoff, M. Selmke, F. Cichos, and K. Kroy, Phys. Rev. Lett. **105**, 090604 (2010).
- [67] H.-R. Jiang, N. Yoshinaga, and M. Sano, Phys. Rev. Lett. **105**, 268302 (2010).
- [68] R. Golestanian, Physics **3**, 108 (2010).
- [69] B.V. Derjaguin, G.P. Sidorenkov, E.A. Zubashchenkov, and E.V. Kiseleva, Kolloidn. Zh. **9**, 335 (1947).
- [70] R.F. Ismagilov, A. Schwartz, N. Bowden, and G.M. Whitesides, Angew. Chem. Int. Ed. **41**, 652 (2002).

- [71] R. Golestanian, T.B. Liverpool, and A. Adjari, Phys. Rev. Lett. **94**, 220801 (2005).
- [72] J.R. Howse, R.A.L. Jones, A.J. Ryan, T. Gough, R. Vafabakhsh, and R. Golestanian, Phys. Rev. Lett. **99**, 048102 (2007).
- [73] S. Ebbens, M.-H. Tu, J.R. Howse, and R. Golestanian, Phys. Rev. E **85**, 020401(R) (2012).
- [74] K.-C. Lee and A.J. Liu, Biophys. J. **95**, 4529 (2008).
- [75] G.P. Alexander and A.J. Liu, (2011), arXiv:1107.3851v1 [cond-mat.mtrl-sci].
- [76] G. Volpe, I. Buttinoni, D. Vogt, H.-J. Kümmerer, and C. Bechinger, Soft Matter **7**, 8810 (2011).
- [77] B. Abécassis, C. Cottin-Bizonne, C. Ybert, A. Ajdari, and L. Bocquet, Nature Materials **7**, 785 (2008).
- [78] J. Palacci, B. Abécassis, C. Cottin-Bizonne, C. Ybert, and L. Bocquet, Phys. Rev. Lett. **104**, 138302 (2010).
- [79] R. Golestanian, Phys. Rev. Lett. **102**, 188305 (2009).
- [80] H. Ke, S. Ye, R.L. Carrol, and K. Showalter, J. Phys. Chem. A **114**(17), 5462 (2010).
- [81] S. Ebbens, R.A.L. Jones, A. J. Ryan, R. Golestanian, and J.R. Howse, Phys. Rev. E **82**, 015304(R) (2010).
- [82] R. Golestanian, T.B. Liverpool, and A. Adjari, . New J. Phys. **9**, 126 (2007).
- [83] B.V. Derjaguin, S.S. Dukhin, and A.A. Korotkova, Kolloidn. Zh. **23**, 53 (1961).
- [84] J.L. Anderson and D.C. Prieve, Sep. Purif. Methods **13**, 67 (1984).
- [85] H.A. Stone and A. Samuel, Phys. Rev. Lett. **77**, 4102 (1996).

- [86] J. Happel and H. Brenner, *Low Reynolds Number Hydrodynamics*, (Prentice-Hall, Englewood Cliffs, 1965).
- [87] J.L. Anderson, *J. Colloid Interface Sci.* **105**, 45 (1985).
- [88] J.D. Jackson, *Classical Electrodynamics*, Third Edition (John Wiley & Sons, New York, 1998).
- [89] S.J. Ebbens and J.R. Howse, *Langmuir* **27**(20), 12293 (2011).
- [90] J.G. Gibbs and Y.-P. Zhao, *Appl. Phys. Lett.* **94**, 163104 (2009).
- [91] M.N. Popescu, S. Dietrich, and G. Oshanin, *J. Chem.Phys.* **130**, 194702 (2009).

Appendix A

Stress Tensor

A key step to understand fluid dynamics requires knowledge of the stress tensor in terms of the properties of the flow, in particular the velocity field. Consider a stress tensor σ [86]:

$$\frac{\partial(\rho\mathbf{v})}{\partial t} + \nabla \cdot (\rho\mathbf{v}^2) = \nabla \cdot \sigma + \rho F, \quad (\text{A.1})$$

where \mathbf{v} is the velocity, ρ represents the density, and F denotes the force. Note that σ is a second-rank tensor (dyadic) and depends on the fluid pressure p , bulk viscosity κ and viscosity η .

$$\sigma = -p\mathbf{I} + \kappa(\nabla \cdot \mathbf{v})\mathbf{I} + 2\eta\Delta, \quad (\text{A.2})$$

$$\Delta = \frac{1}{2}[\nabla\mathbf{v} + (\nabla\mathbf{v})^T] - \frac{1}{3}\mathbf{I}(\nabla \cdot \mathbf{v}), \quad (\text{A.3})$$

here $\mathbf{I} = \delta_{ij}$ which is the Kronecker delta and T denotes transpose matrix.

For incompressible flow, the divergence of the velocity vanishes $\nabla \cdot \mathbf{v} = \mathbf{0}$, therefore the stress tensor σ in Eq. (A.2) becomes

$$\sigma = -p\mathbf{I} + \eta[\nabla\mathbf{v} + (\nabla\mathbf{v})^T]. \quad (\text{A.4})$$

In order to obtain the full picture of the stress tensor σ , the only problem we have to confront is the velocity gradient $\nabla \mathbf{v}$. The velocity gradient in spherical coordinate (r, θ, φ) can be recognizably written in matrix form [86]:

$$\nabla \mathbf{v} = \begin{bmatrix} \frac{\partial v_r}{\partial r} & \frac{\partial v_\theta}{\partial r} & \frac{\partial v_\varphi}{\partial r} \\ \frac{1}{r} \left(\frac{\partial v_r}{\partial \theta} - v_\theta \right) & \frac{1}{r} \left(\frac{\partial v_\theta}{\partial \theta} + v_r \right) & \frac{1}{r} \frac{\partial v_\varphi}{\partial \theta} \\ \frac{1}{r} \left(\frac{1}{\sin \theta} \frac{\partial v_r}{\partial \varphi} - v_\varphi \right) & \frac{1}{r} \left(\frac{1}{\sin \theta} \frac{\partial v_\theta}{\partial \varphi} - v_\varphi \cot \theta \right) & \frac{1}{r} \left(\frac{1}{\sin \theta} \frac{\partial v_\theta}{\partial \varphi} - v_\varphi \cot \theta \right) \end{bmatrix} \quad (\text{A.5})$$

We can now use Eq. (A.5) to interpret all the components of the stress tensor σ . Let us write out Eq. (A.4) entirely and recall that $\sigma_{12} = \sigma_{21}$, etc.

$$\sigma_{rr} = -p + 2\eta \frac{\partial v_r}{\partial r}, \quad (\text{A.6})$$

$$\sigma_{\theta\theta} = -p + \frac{2\eta}{r} \left(\frac{\partial v_\theta}{\partial \theta} + v_r \right), \quad (\text{A.7})$$

$$\sigma_{\varphi\varphi} = -p + \frac{2\eta}{r} \left(\frac{1}{\sin \theta} \frac{\partial v_\theta}{\partial \varphi} - v_\varphi \cot \theta \right), \quad (\text{A.8})$$

$$\sigma_{r\theta} = \sigma_{\theta r} = \frac{\partial v_\theta}{\partial r} + \frac{1}{r} \left(\frac{\partial v_r}{\partial \theta} - v_\theta \right), \quad (\text{A.9})$$

$$\sigma_{\theta\varphi} = \sigma_{\varphi\theta} = \frac{1}{r} \frac{\partial v_\varphi}{\partial \theta} + \frac{1}{r} \left(\frac{1}{\sin \theta} \frac{\partial v_\theta}{\partial \varphi} - v_\varphi \cot \theta \right), \quad (\text{A.10})$$

$$\sigma_{\varphi r} = \sigma_{r\varphi} = \frac{\partial v_\varphi}{\partial r} + \frac{1}{r} \left(\frac{1}{\sin \theta} \frac{\partial v_r}{\partial \varphi} - v_\varphi \right). \quad (\text{A.11})$$